Graphene Membranes: Mechanics, Adhesion, and Gas Separations

by

Steven P. Koenig

B.S., Texas State University – San Marcos 2008

M.S., University of Colorado at Boulder 2010

A thesis submitted to the Faculty of the Graduate School of the University of Colorado in partial fulfillment of the requirement for the degree of

Doctor of Philosophy

Department of Mechanical Engineering

2013

This thesis entitled:
Graphene Membranes: Mechanics, Adhesion, and Gas Separations
written by Steven P. Koenig
has been approved for the Department of Mechanical Engineering

_____

J. Scott Bunch
Committee Chairman, Dept. of Mechanical Engineering

_____

Todd W. Murry
Dept. of Mechanical Engineering

Date_____

The final copy of this thesis has been examined by the signatories, and we find that both the content and the form meet acceptable presentation standards of scholarly work in the above mentioned discipline.

Koenig, Steven P. (Ph.D., Department of Mechanical Engineering)

Graphene Membranes: Mechanics, Adhesion, and Gas Separations

Thesis directed by Professor J. Scott Bunch

ABSTRACT

This thesis examines the mechanical, and adhesive properties of graphene and explores using graphene as a gas separation membrane. A pressurized blister test was used to measure both the in-plane mechanical properties and adhesion energy of monolayer and few layer graphene suspended over a circular cavity in silicon oxide. The adhesion energy between graphene and silicon oxide was found to be 0.45 ± 0.02 J m^{-2} for monolayer graphene and 0.31 ± 0.03 J m^{-2} for samples containing two to five graphene layers. These values are larger than the adhesion energies measured in typical micromechanical structures and are comparable to solid-liquid adhesion energies. We attribute this to the extreme flexibility of graphene, which allows is to conform to the topography of even the smoothest substrates, thus making its interaction with the substrate more liquid like than solid like. In addition we found that the in-plane mechanical properties are consistent with previously reported values.

We also show that ultraviolet-induced oxidative etching can create pores in micrometer-sized graphene membranes, and the resulting membranes can be used as molecular sieves. A pressurized blister test, similar to that used for testing the mechanical properties, and mechanical resonance are used to measure the transport of a range of gases (H_2, CO_2, Ar, N_2, CH_4, and SF_6)

through the pores. The experimentally measured leak rate, separation factors, and Raman spectrum agree well with models based on effusion through a small number of angstrom-sized pores.

Lastly, we work toward creating large scale gas separation membranes from chemical vapor deposition (CVD) grown graphene films. CVD graphene films are grown on copper foils and transferred to a polymer support or suspended over openings in copper. Films are measured in a time lag permeation apparatus to get gas permeation and ideal gas separation factors.

This dissertation is dedicated to my friends and family.

“Education isn’t something you can finish”

Isaac Asimov (1920 - 1992)

ACKNOWLEDGEMENTS

Upon starting the PhD program at the University of Colorado – Boulder and joining Scott Bunch's research group I knew I had my work cut out for me. Scott was a new faculty member and therefore was starting with an empty lab. It was partially my job to populate the lab with equipment and help shape the direction of the research we would carry out. A daunting task that, perhaps, I had underestimated at the start. In the end it was an experience that was as equally rewarding as it was challenging.

Many people contributed to my success throughout graduate school and none more important than my advisor, Scott Bunch. He was an inspirational leader to a new lab and a prime example of what it would take to be a successful young scientist. His patient guidance and enthusiasm for science were instrumental in helping me be a successful graduate student. His "just try it" approach to experimentation pushed me to do experiments that seemed improbable at first. In fact, one such experiments ended up becoming a chapter in this thesis.

Another person who was instrumental in my success in graduate school is Sharon Anderson, the graduate program assistant for the Mechanical Engineering Department. Sharon is, somewhat jokingly, referred to as the department mom because she looks out for all the graduate students like a mother and always has our best interest at heart. Sharon has helped me from my first visit to CU all the way to making sure that I have completed all of my graduation requirements at the right time and just about everything in between. If I ever have a question I will go to Sharon first. I know that even if she does not have the answer to my questions she will know exactly where to look or who to ask.

Starting off in a new and lonely lab was eased by the company of two other new graduate student who started in the lab that first semester, Xinghui Liu and Fanghao Yang. Xinghui provided support through the years with his acquired expertise for device fabrication. Xinghui was able to make devices of great complexity without much trouble and help me when I struggled on the relatively simple fabrication I was faced with. Xinghui was great at exfoliating graphene and together we were able to make many exfoliated graphene devices in that first year.

Not long after starting in the lab we had started a collaboration with the Steve George lab in Chemistry and one of his Post-Docs, Guillermo Acosta, started working closely with us. Guillermo was a great help using the atomic force microscope (AFM) in the Steve George lab and help me get some of the first AFM images of suspended graphene. A print out of one of those images is actually still hanging on the door to the lab and it reminds me of those days starting off. Guillermo was also helpful in some of the first UV etching experiments. I think he was the one to suggest using UV because of his previous experience. Guillermo also made the lab feel like a more familiar place. He loved working on cars which was something I had done with my dad growing up and we would talk about cars while running experiments in the lab late at night.

Going back to that first year, I would like to acknowledge the other members of my first year PhD class for helping me through the struggles of classes, being a TA, doing research, and studying for prelims all at the same time. Without them I might not have made it through that treacherous first year. I want to especially thank Jill Cooper and Rachel Paietta for being such great friends in that first year and beyond. Although I am closest with Jill and Rachel, I also would like to thank Jeremy McCaslin, Matt Brubaker, Mark Czajkowski, and John Francis. They all helped me in some way but there are many others who also contributed.

I want to thank all of the awesome roommates I have had the pleasure of living with over the years of graduate school: Mark Tibbitt, Mike Griffin, Josh Breland, Peter Mitrano, Nate Shieko, and Dave Busha. They all seem like a part of my family now and we have some great memories from living together. I especially want to thank Mark Tibbitt. I moved in with Mark and Josh after looking at a craigslist ad and briefly talking to Mark on the phone while finishing up my undergraduate degree at Texas State University. I really didn't know what to expect moving to a new place and not knowing anyone but Mark helped to make the experience unforgettable. Not only was Mark a great roommate he has been a great friend and also somewhat of a mentor. Even though Mark was only in graduate school one year more than me, he was wise well beyond his years and offered spot on advice at nearly every turn of my time in graduate school, from research problems to navigating the intricacies of graduate school. Mark and I lived together for nearly five years and he was by far the easiest and most enjoyable person to live with.

I would like to thank Narasimha Boddeti for his help with the modeling and mechanics expertise he provided in the work on graphene adhesion and mechanics. I would also like to thank Prof. Martin Dunn who was Narasimha's advisor for his contributions to the adhesion and mechanics of graphene work. Together, with Scott, the four of us were able to make sense of data that had me scratching my head when first plotting it. Without their help, that work probably would not have come to be the high quality highly cited paper that it is.

Luda Wang started in the Bunch Lab in my second year of graduate school. Luda was given the task of putting the finishing touches on the optical drive and detection system that I started building in my first year. Luda was enthusiastic about working with the system and quickly learned how to use it and immediately started making improvements on what I had built.

Luda was instrumental in getting the resonance gas permeation data that is presented in Chapter 5. Luda also continued the ALD on graphene work that we started in our first year with Guillermo and the Steve George Lab and Luda is now continuing the work on gas separations through porous graphene and ultrathin ALD oxide membranes.

Prof. John Pellegrino helped with the graphene gas separation work. I was a little lost when first getting into the field of graphene gas separations but John's expertise in membrane research helped to shape that project and my understanding of membranes.

I want to thank everyone that has been a part of the United Government of Graduate Students (UGGS) with me. They were my graduate school home away from home and have become some of my best friends over the last few years. Specifically I would like to thank Laura Michaelson, Kate Allison, and Joey Hubbard.

I would like to thank Prof. Harold Park for hiring me over the summer before I started graduate school. He gave me a chance to come into his lab and learn about computational nanomechanics and decide whether that was something I wanted to continue with in graduate school without committing to work with him for a full year. Although I didn't end up working with him beyond the summer, I learned a lot about programming and computational research and it has given me much insight when reading computational based papers in the literature. Prof Park also gave me the opportunity to come out to Boulder sooner and get to know the town before starting up graduate school, an opportunity that I value to this day.

Although not directly related to graduate school I want to thank Prof. Donnelly, Prof. Ventrice, and Prof. Galloway for getting me excited about physics and physics research while an undergraduate at Texas State University. Taking Dr. Donnelly's intro physics course compelled

me to change my major to physics. After changing my major I never looked back and have been a science enthusiast ever since. Dr. Galloway gave me the first opportunity to teach physics labs and further my passion for the subject. Both Prof Galloway and Prof. Ventrice gave me chances to work in their research labs and develop a passion for research. I recently traveled back to Texas State University to give a research talk and it was one of the most rewarding experiences to be able to be on the other end of a departmental colloquium talk and give a lecture to the faculty and students of the physics department.

Last but certainly not least I would like to thank my parents and two sisters for their love and support throughout my life, especially during the more challenging times.

I know, inevitably, I am leaving someone deserving off this ever growing list of great people who have inspired and helped me along the way but it is not because of their lack of help but rather my limited memory capacity. Nonetheless, I am thankful to all of those who have contributed in some way to my success without your help there is no telling if the results would be the same.

TABLE OF CONTENTS

LIST OF FIGURES

LIST OF TABLES

1. Introduction

1.1. Introduction

Much like the discovery of other carbon allotropes such as buckminsterfullerenes (fullerenes) and carbon nanotubes (CNTs) before it, the recent isolation of graphene in 2004 has brought with it a wealth of scientific and technological research [1]. In contrast with the zero-dimensional fullerenes and one-dimensional CNTs, graphene is the two-dimensional hexagonal crystal planes of covalently bonded carbon atoms that when stacked form graphite (Figure 1-1). Graphene represents the two dimensional thickness limit for materials, while having excellent mechanical properties due to the carbon-carbon bond. With a Young's modulus of ~1 TPa a single suspended layer of graphene is one of the stiffest materials known to man [2]. Despite its remarkable mechanical properties the graphene-research buzz was initially generated due to the extraordinary electronic properties offered by this two-dimensional electron system. Applications of graphene run the gambit from nano-electro-mechanical systems (NEMS), such as electrostatic loudspeakers [3] and nano-mechanical switches [4], to electronics application, such as transparent conducting electrodes [5] and flexible electronics [6], just to name a few. Research of graphene is still a relatively new field with new and interesting applications being constantly proposed and demonstrated. Despite its newness the field of graphene research is moving a break-neck speed and only one thing can be certain, by the time you are reading this thesis it will most likely out of date. This thesis is only one piece of the puzzle to realizing the vast potential of graphene for future application.

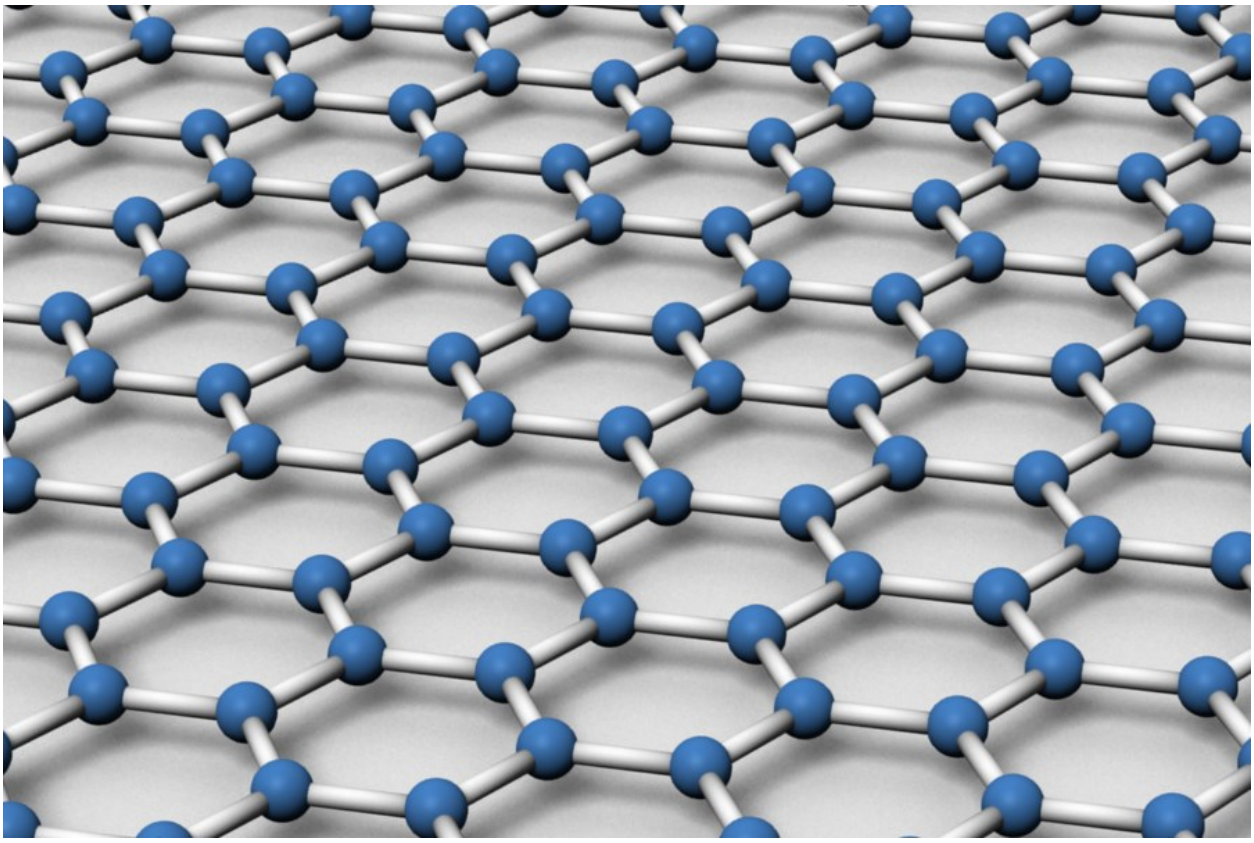

Figure 1-1 Graphene crystal structure. Carbon atoms are blue[1].

[1] Compliments of James Hedberg http://creativecommons.org/licenses/by-nc-sa/3.0/ http://www.jameshedberg.com/scienceGraphics.php?sort=all&id=graphene-atomic-structure-sheet

1.2. Thesis Outline

This thesis presents some of the first experiments on the adhesive and gas separation properties of graphene as well as relevant results on the mechanical properties of single and few layer graphene membranes. Chapters 1-3 provide an overview of some of the basic concepts needed for the experimental results. Chapters 4-6 contain the experimental results on graphene mechanics, adhesion, and gas separations followed by a conclusions and future outlook in Chapter 7. The experimental section begins with Chapter 4 where we perform mechanical and adhesion testing on pressurized circular graphene membranes. We find that the mechanics of single and few-layer graphene scale with the number of layers and that graphene has remarkably high adhesion strength which is attributed to its extreme flexibility. A modified form of this chapter is published in two journal articles, *Nature Nanotechnology* **6**, 543 (2011) and *Journal of Applied Mechanics* **80**(4), 041044 (2013). An experimental study of using graphene as a gas separation membrane begins in Chapter 5 where we study molecular sieving through molecular-sized pores etched in graphene. We create the world's thinnest gas separation membranes from single and bi-layer graphene suspended over circular cavities in SiO_2. A version of this chapter is published in *Nature Nanotechnology* **7**, 728 (2012). Chapter 6 is the first step to realizing large scale graphene based gas separation membranes made from CVD grown graphene. The work of this chapter remains unpublished.

1.3. Primary Accomplishments

Thus far this research effort has resulted in three journal articles and a multitude of conference and invited presentations.

Journal Articles:

- Boddeti, N.G., Koenig, S.P., Long, R., Xiao, J., Bunch, J.S., Dunn, M.L. Mechanics of Pressurized Graphene Blisters, *Journal of Applied Mechanics* 80(4), 041044 (2013)
- Koenig, S. P., Wang, L., Pellegrino, J., Bunch, J. S. Selective molecular sieving through porous graphene. *Nature Nanotechnology*, **7**, 728-732 (2012).
- Wang, L., Travis, J. J., Cavanagh, A. S., Lui, X., Koenig, S. P., Haung, P. Y., George, S. M., Bunch, J. S., Ultrathin Oxide Films by Atomic Layer Deposition on Graphene. *Nano Letters* **12** (7), 3706-3710 (2012).
- Koenig, S. P., Boddeti, N. G., Dunn, M. L., Bunch, J. S. Ultrastrong adhesion of graphene membranes. *Nature Nanotechnology* **6**, 543-546 (2011).

Selected Conference Presentations:

- Koenig, S. P., Wang, L., Pellegrino, J., Bunch, J. S. Selective Molecular Sieving through Porous Graphene. North American Membrane Society 22nd Annual Meeting (Oral Presentation), New Orleans, LA, June 10th-13th, 2012.
- Koenig, S. P., Boddeti, N. G., Dunn, M. L., Bunch, J. S. Ultrastrong adhesion of graphene membranes. Proceedings for American Physical Society (APS) March Meeting 2012 (Oral Presentation), Boston, MA, Feb. 27th – Mar. 2nd, 2012.

Technical Contributions:

- Set up optical table in the Bunch lab and designed and built an optical drive and detection system to measure the resonance of micro and nano structures
- Set up atomic force microscope and pressure chambers in the Bunch lab for pressurizing graphene membranes

- Designed and built time-lag permeation measurement system to measure gas permeation through large scale CVD grown graphene membranes.

1.4. Introduction to Mechanics

One of the most popular problems in physics is that of the mass on a spring. The mass spring system is used from introductory physics all the way up to solid state physics. It can help explain grandfather clocks, musical instruments, mechanics of materials, and the origin of van der Waals forces. The basic underlying equation that governs the mass spring systems is that of Newton's second law, given by

$$F = ma \qquad \{1\text{-}1\}$$

where F is the force, m is mass, and a is acceleration. Another important equation for physics and engineering is that of Hooke's law

$$F = -kx \qquad \{1\text{-}2\}$$

where $k = m\omega^2$ and $a = -\omega^2 x$, k being the spring constant, x displacement and ω the angular frequency. Figure 1-2 shows a plot and schematic of a spring in the region of small displacement where Hooke's law applies. These two equations will form the basis of our analysis of mechanics of materials and harmonic oscillators studied in this chapter. The two following section will go over the basics of mechanics of materials and harmonic oscillators, respectively.

1.4.1. Mechanics of Materials

For the most simple case in mechanics of materials an analogy of Hooke's law (equation {1-2}) can be used. Similar to the case for a spring, Hooke's law applies at small displacements.

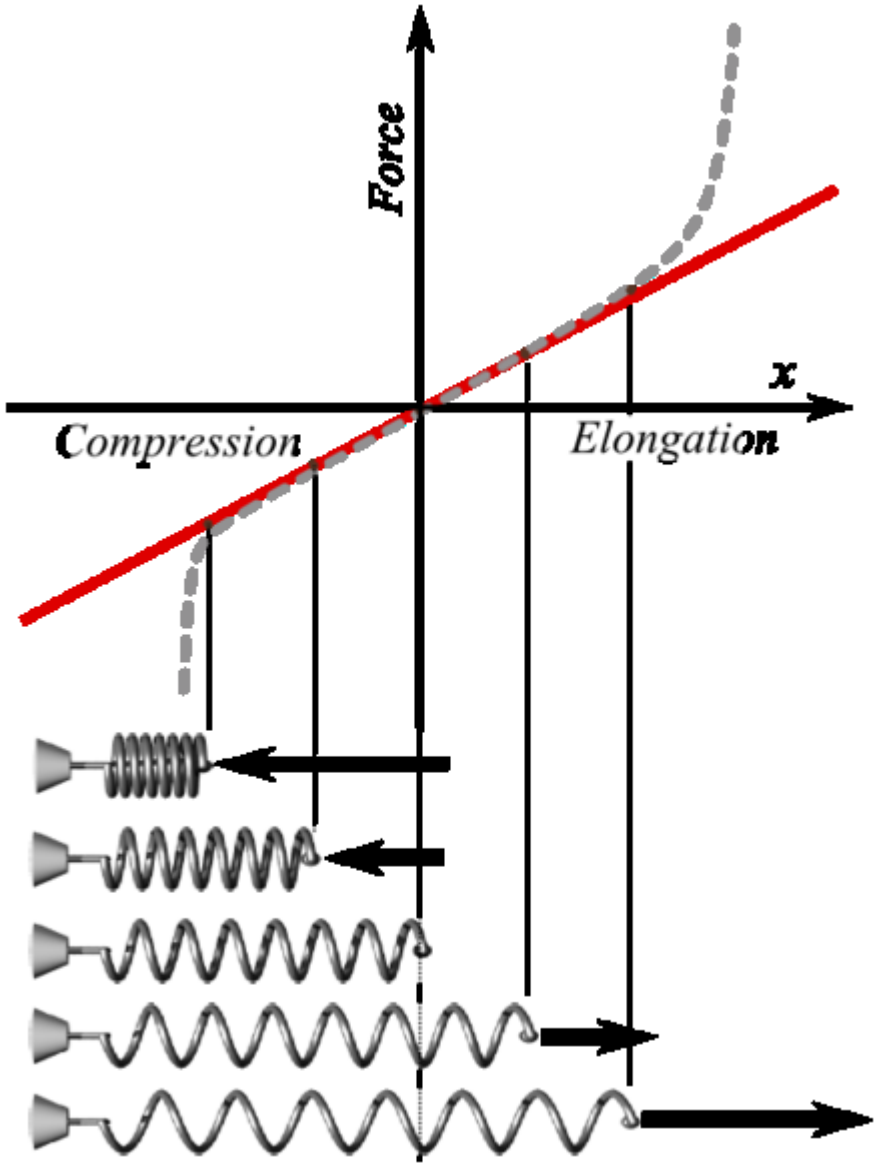

Figure 1-2 Plot of applied force *F* versus displacement for a spring following Hooke's law (red line) and the actual plot of the spring behavior outside of the linear elastic region (grey dashed line) The bottom shows spring states corresponding to some points on the force displacement curve. The middle spring corresponds to the spring in its relaxed state, when no force is applied. From Wikipedia.com: Hooke's law.

As can be imagined for higher dimensional material systems the Hooke's law analogy can get a little more complicated. No need to worry, we will walk through the basics to get you started for this thesis. For a force acting on a material in one dimension, the stress, σ, in the material with an applied force, F, acting on an area, A, is expressed by

$$\sigma = \frac{F}{A} \qquad \{1\text{-}3\}$$

Just as in the case of the spring, when a force acts on a material the material will deform. The material will elongate in the direction of the applied force when pulled apart at both ends, tensile stress, and will contract, in the direction of the applied force, when pushed together, compressive stress. The amount a material deforms is known as strain and is given by

$$\varepsilon = \frac{\Delta L}{L} = \frac{l - L}{L} \qquad \{1\text{-}4\}$$

where ε is the strain, L is the original length of the material, l is the final length of the material, and ΔL is the change in length of the material.

Now that stress and strain are defined we can now relate stress and strain analogous to Hooke's law. For a one dimensional material the relation between stress and strain is given by

$$\sigma_x = E\varepsilon_x \qquad \{1\text{-}5\}$$

where E is the Young's modulus of the material, also known as the elastic modulus. As with Hooke's law the Young's modulus is a measure of the material's stiffness. The higher the Young's modulus the less a material will deform in the presence of a given applied load. This assumes that the material is isotropic, i.e. the material properties are the same in all directions. In

many bulk solid materials this is generally a valid assumption due to the polycrystalline nature of most bulk materials where individual crystallites are randomly oriented.

When a material is strained in one direction it tends to contract in the perpendicular direction to the applied strain. The ratio of the strain in the perpendicular directions is defined by the Poisson's ratio given by

$$\nu = -\frac{\varepsilon_y}{\varepsilon_x} \qquad \{1\text{-}6\}$$

The Poisson's ratio for linear elastic, isotropic materials ranges $-1 < \nu \leq 0.5$. Most materials have a Poisson's ratio between 0 and 0.5. A Poisson's ration of 0.5 means that a material is perfectly incompressible, an example material with a Poisson's ratio of 0.5 is rubber. A Poisson's ratio of 0 means that the material does not deform in the perpendicular direction, an example material with a Poisson's ratio of 0 is cork. Materials with a Poisson ratio less than zero are known as auxetic materials. When auxetic materials are stressed in one direction they will expand in the perpendicular directions. auxetic materials are rare in nature but can be made and are known as mechanical metamaterials. A table of typical Young's modulus and Poisson's ratio for some common materials can be found in Table 1.1.

Table 1.1 Approximate Young's modulus for various materials. Adapted from Wikipedia.com: Young's Modulus and Poisson's ratio unless otherwise noted.

Material	**Young's modulus (*E*) in GPa**	**Poisson's ratio (*v*)**
Rubber (small strain)	0.01-0.1	~0.50
Titanium (Ti)	105-120	0.34
Copper (Cu)	110-130	0.33
Aluminum (Al)	69	0.33
Gold (Au)	79	0.42
Magnesium	45	0.35
Glass	50-90	0.18-0.3
Steel	200	0.27-0.30
Concrete	22-29	0.20
Silicon (Si)	150	0.22-0.27[2]
Silicon Carbide (SiC)	450	0.183-0.192[3]
Diamond	1,220	0.115-.00786 [7]
Single walled carbon nanotube	1,000	0.16
Graphene	1,000	0.16
Cork	0.0186	~0
Auxetic Materials	n/a	$-1 < v < 0$

[2] From http://www.memsnet.org/material/siliconsibulk/
[3] From http://www.memsnet.org/material/siliconcarbidesicbulk/

For an isotropic material under a general state of stress equations {1-5} and {1-6} can be combined to give the three dimensional version of Hooke's law, also known as the generalized Hooke's law, which relates stress and strain as [8]:

$$\varepsilon_x = \frac{1}{E}\left(\sigma_x - \nu\left(\sigma_y + \sigma_z\right)\right)$$

$$\varepsilon_y = \frac{1}{E}\left(\sigma_y - \nu\left(\sigma_z + \sigma_x\right)\right) \qquad \{1\text{-}7\}$$

$$\varepsilon_z = \frac{1}{E}\left(\sigma_z - \nu\left(\sigma_x + \sigma_y\right)\right)$$

For the case of biaxial stress, stress only acting in the x and y directions equations {1-7} simplify to

$$\varepsilon_x = \frac{1}{E}\left(\sigma_x - \nu\sigma_y\right)$$

$$\varepsilon_y = \frac{1}{E}\left(\sigma_y - \nu\sigma_x\right) \qquad \{1\text{-}8\}$$

$$\varepsilon_z = \frac{\nu}{E}\left(\sigma_x + \sigma_y\right)$$

For the case of an isotropic plate under biaxial strain Hooke's law simplifies to

$$\sigma = \left(\frac{E}{1-\nu}\right)\varepsilon \qquad \{1\text{-}9\}$$

Another important property for plates subjected to out of plane deformations is the bending rigidity. The bending rigidity, B, is defined as the energy per unit area, A, needed to curve an object

$$B = 2\frac{E_{bend}}{A}R^2 \qquad \{1\text{-}10\}$$

In this equation, R is the radius of curvature. In continuum mechanics the bending rigidity is usually defined in terms of the Young's, modulus, Poisson's ratio, and thickness, w, of the plate given by

$$B = \frac{Ew^3}{12(1-\nu^2)} \qquad \{1\text{-}11\}$$

Equation {1-11} assumes that the curved plate is stretching along its top surface and compressing along its bottom surface. However, when thicknesses approach the atomic scale the continuum model breaks down and the bending rigidity becomes an intrinsic property of the material due to chemical bond interactions [9], [10]. This is the case for graphene and we will discuss this further in Chapter 2.

A more in depth analysis of membrane and plate mechanics will be presented in Chapter 3.

1.4.2. Harmonic Oscillator

The harmonic oscillator has wide application in both classical and quantum physics and has played a pivotal role in the development of both. The simplest and most common used model is that of a mass attached to a spring and sliding along a frictionless surface. Another example is that of a pendulum with an oscillation frequency proportional to its length. This was fist observed in the early 17th century by Galileo. For small displacements a spring follows Hooke's law given by equation {1-2}. To solve the harmonic oscillator equation first we combine equations {1-1} and {1-2} to give

$$ma = m\frac{d^2x}{dt^2} = -kx \qquad \{1\text{-}12\}$$

Solving the differential equation we get the solution for the motion of the undamped harmonic oscillator given by

$$x(t) = A\cos(\omega_0 t - \varphi) \qquad \{1\text{-}13\}$$

where t is time, and ω_0 is the resonant frequency of the mass spring system and φ is the phase of the system. A is the amplitude of the harmonic motion and will depend on the initial conditions. The resonant frequency is given by

$$\omega_0 = \sqrt{\frac{k}{m}} \qquad \{1\text{-}14\}$$

Of course in real life situations a system there are rarely frictionless surfaces or media for the mass to pass through which means that we will need to introduce a damping term which dissipates vibrational energy. Also many vibrational systems are driven so we will introduce both a driving force with amplitude F and frequency ω and a damping term with constant of c. The damping will be proportional to the velocity of the oscillator. These two terms will modify equation {1-12} to become.

$$m\frac{d^2x}{dt^2} + c\frac{dx}{dt} + kx = F\cos(\omega t) \qquad \{1\text{-}15\}$$

The solution is similar to that of the undamped, undriven case with one exception, ω_0, the resonant frequency, is now ω , the drive frequency, in the cosine [11].

$$x(t) = D\cos(\omega t - \phi) \qquad \{1\text{-}16\}$$

where

$$D = \frac{F}{k}\frac{Q}{\sqrt{Q^2\left(1-\frac{\omega^2}{{\omega_0}^2}\right)^2+\left(\frac{\omega}{\omega_0}\right)^2}} \qquad \{1\text{-}17\}$$

$$\phi = \tan^{-1}\left(\frac{\omega\omega_0}{Q\left({\omega_0}^2-\omega^2\right)}\right) \qquad \{1\text{-}18\}$$

$$Q = \frac{m\omega_0}{c} \cong \frac{\omega_0}{\Delta\omega} \qquad \{1\text{-}19\}$$

The resonance frequency can also be expressed as $\omega_0 = 2\pi f_0$. Here Q is known as the quality factor and $\Delta\omega$ represents the frequency interval between the points on the amplitude curve that are at $1/\sqrt{2}$ of the maximum amplitude. Damping in the driven damped harmonic oscillator keeps the resonance amplitude from going to infinity when the drive frequency is at the resonance frequency.

Figure 1-3 shows the response of a damped driven harmonic oscillator. It should be noted that damping causes a lowering of the resonance frequency, ω_R , given by

$$\omega_R = \sqrt{{\omega_0}^2 - \frac{c^2}{2m^2}} \qquad \{1\text{-}20\}$$

and no resonance will occur if $c > m\omega_0$.

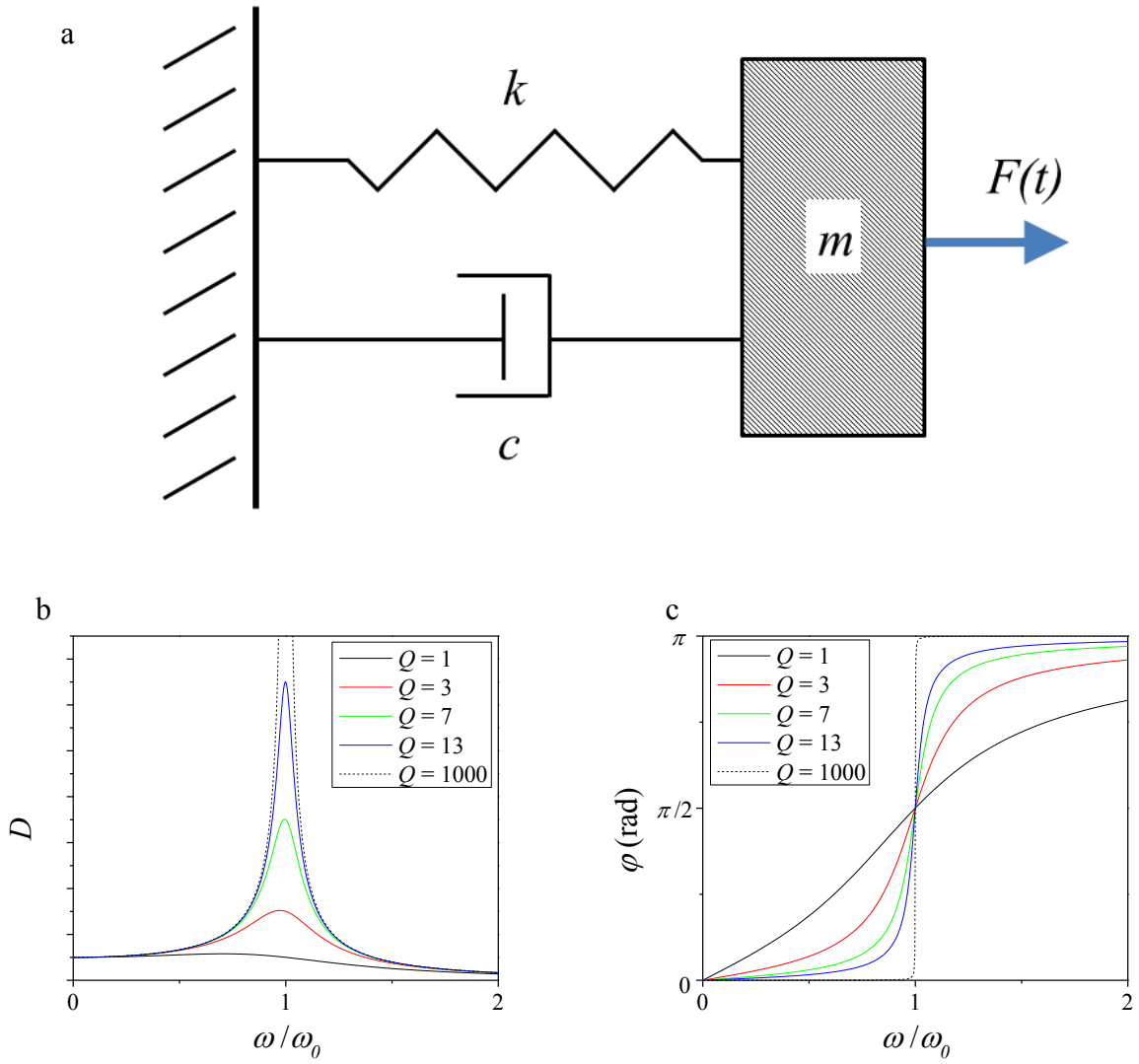

Figure 1-3 (a) Schematic of a damped driven harmonic oscillator with mass *m*, spring constant *k*, damping coefficient *c* and force *F*(*t*). (b) is the amplitude, *D*, and (c) is phase, *φ*, plotted as a function of the ratio of drive frequency *ω* to the resonant frequency, ω_0 plotted with various *Q*s for a damped driven harmonic oscillator. 1 corresponds to the drive frequency being equal to the resonant frequency.

1.5. Gas Separation Membranes

Membranes for gas separation have gained scientific interest due to their ability to be highly selective membranes that can exceed efficiency of traditional processes for separating gas species. A few such energy intensive separation processes that are traditionally used for gas separation are cryogenic distillation, condensation of organic vapors, and amine absorption [12], [13]. The three aforementioned separation processes suffer in efficiency due to a large amount of energy expenditure for gas-to-liquid and/or liquid-to-gas phase changes. Gas separation membranes have the advantage of not requiring phase change, having a smaller footprint, and having significantly less mechanical complexity. The most common type of gas separation membranes used today in industrial applications are polymeric membranes due to the relative simplicity of large scale production. Polymeric membranes are used in a variety industrial applications such as microfiltration, ultrafiltration, reverse osmosis, and gas separation. Although polymer membranes are the most commonly utilized separation membranes can also be made out thin metallic, glass, and ceramic materials or a combination of the four. The latter, composite membranes, are known as mixed matrix membranes and consists of one material as the matrix where a material with different transport properties is embedded in the matrix [14]. Commonly polymers are used as the matrix and hollow fibers, zeolite crystals, or ceramic materials are embedded to alter the transport and selectivity of varies molecules or particles [13]. In addition to the materials used to make a membrane, membranes can be homogeneous, consisting of one material phase, or heterogeneous, mixed matrix, symmetric or asymmetric, dense or porous.

Often membranes are classified by their pore size or size of the materials they are designed to separate. Figure 1-4 shows the size ranges of traditional filtration and separation membranes. Membranes with pores larger than 100 μm are in the conventional filtration range

and are used to separate course particles. Microfiltration commonly refers to separation and filtration of particles in the size ranges of 500 nm up to the millimeter range. Common materials targeted for microfiltration include yeast, pollen, bacteria, and other fine particles in this size range. Ultrafiltration and Nanofiltration operate in the ~1 nm up to the 1 μm range and are used for the separation of proteins, endotoxins, and viruses. Reverse osmosis (RO) membranes are used for purifying water and can separate dissolved salts from a few angstroms in size up to a few nanometers. Gas separation membranes typically have smaller pores than RO membranes or are dense polymeric or glassy that operate by solution diffusion.

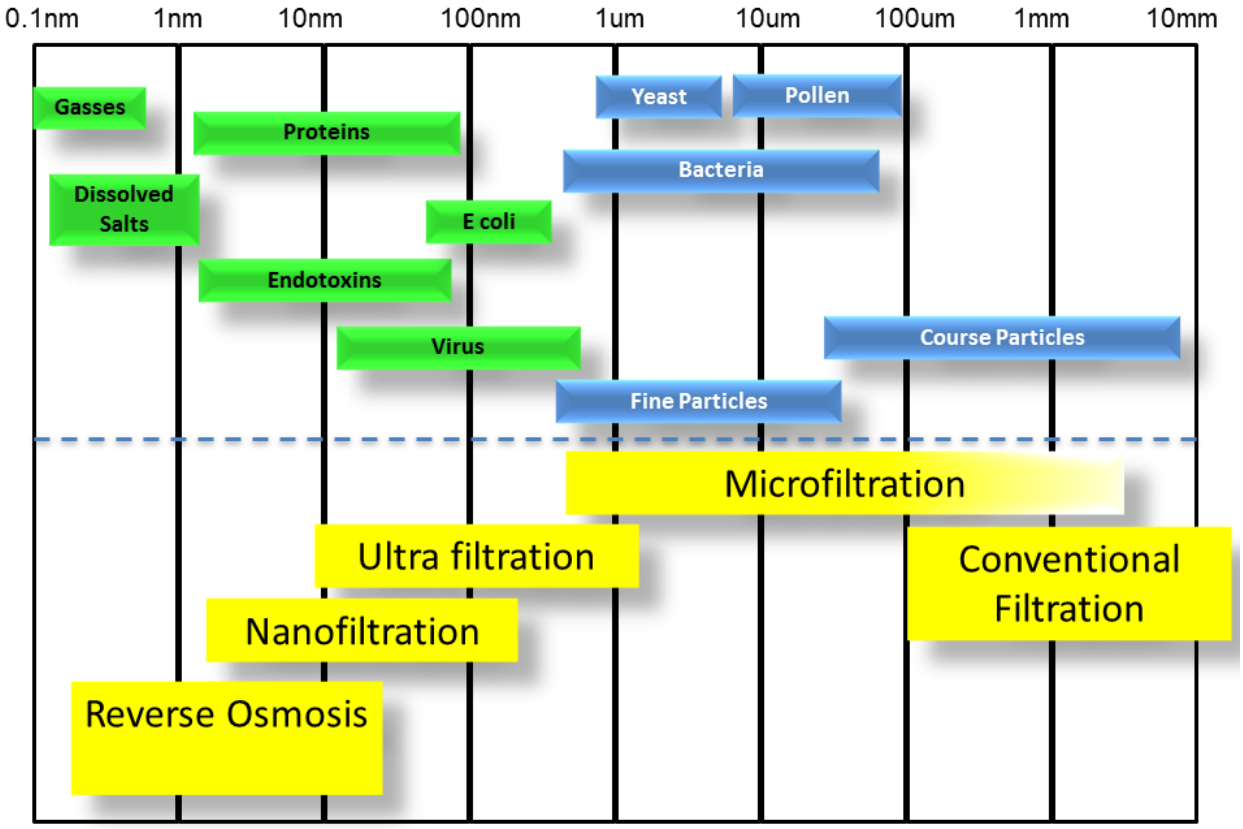

Figure 1-4 Chart of membrane filtration and separation size ranges. Top shows particles and material of interest for separation. Bottom shows size range of membrane pores.

1.5.1. Gas Transport Mechanisms

For gas separation membranes a number of transport mechanisms are possible depending on the permeant and the membrane being used. Figure 1-5 shows a schematic of the various transport mechanism for porous and dense membranes. The most common transport mechanisms in gas separation membranes are Poiseuille flow, Knudsen diffusion, surface diffusion (Figure 1-5a), and solution diffusion (Figure 1-5b). Effusion is also possible but rare due to the thickness of traditional membranes. For traditional porous membranes with pores larger than the molecular size of the permeant gas, transport occurs by Poiseuille flow, Knudsen diffusion, or a combination of the two. The degree to which Poiseuille flow or Knudsen diffusion are the dominant transport mechanisms depends on the ratio of the pore radius, r, to the mean free path of the gas, λ. The mean free path of a given gas molecule is given by [12]

$$\lambda = \frac{2\eta}{2P}\frac{\left(\pi RT\right)^{1/2}}{2M} \qquad \{1\text{-}21\}$$

where η is the viscosity of the gas, R is the universal gas constant, T is temperature, M the molecular weight, and P is the pressure. For values of $r/\lambda << 1$ Knudsen diffusion or effusion will dominate and for values of $\lambda/r << 1$ Poiseuille or viscous flow is the dominant transport mechanism. For a membrane with thickness, w, effusion will dominate when the mean free path of the molecule is much larger than the thickness of the membrane, $\lambda >> w$, so that there will be no collisions with the side wall of the pore during transport. When the mean free path of the molecule is one the order or smaller than the thickness of the membrane Knudsen diffusion will become the dominant transport mechanism.

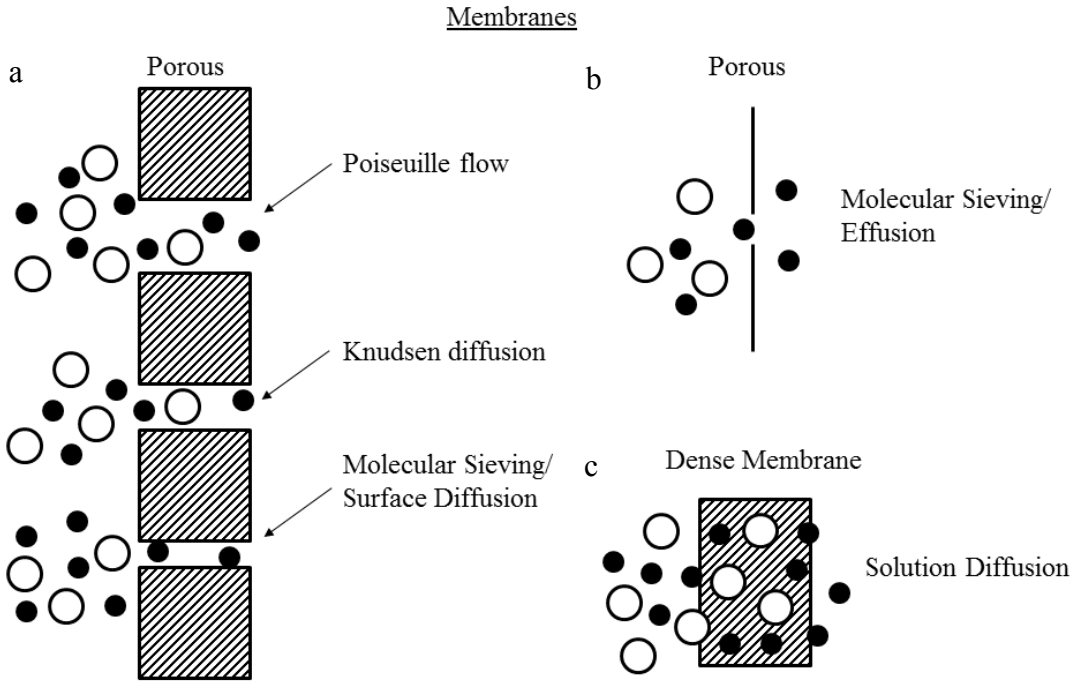

Figure 1-5 Schematic of transport mechanisms for permeation of gases through porous (a and b) and dense membranes (c). Schematic is adapted from [12].

From classical effusion of molecules out of a box, of volume, V, with a hole of area, A, flowing into a vacuum, the number of molecules in the box at time, t, is given by

$$N = N_0 e^{-\frac{A}{V}\sqrt{\frac{k_b T}{2\pi m}}t} \qquad \{1\text{-}22\}$$

where N_0 is the number initial number of molecules in the box at time t=0, m is the molecular mass of the effusing molecules, and k_b is Boltzman's constant. From equation {1-22} we can get the rate of molecules passing through a pore with a pressure difference, Δp, by first taking $\frac{d}{dt}$ at t=0 to get, *dN/dt,* [15], [16]

$$\frac{dN}{dt} = -N_0 \frac{A}{V}\sqrt{\frac{k_b T}{2\pi m}} \qquad \{1\text{-}23\}$$

To get an expression as a function of the pressure across the pore we can use the ideal gas law to substitute $\frac{N_0}{V} = \frac{\Delta p}{k_b T}$ to get[4]

$$\frac{dN}{dt} = \frac{A}{\sqrt{2\pi m k_b T}}\Delta p \qquad \{1\text{-}24\}$$

Equations {1-22} and {1-24} assume a point particle traveling through the pore with no interaction with the pore and thus perfect transmission. That is if the molecule strikes the pore it has 100% probability of getting to the other side. This is a valid assumption for molecules that are much smaller than the pore area. When the pore area is close to the size of the molecule passing through the interactions with the pore can become significant and make the transmission probability less than one. When the pore is near the size of the molecule the molecular shape and

[4] Not that the sign is just a function of which direction the flow is defined as. For this expression we take the flow to be positive across the membrane.

shape of the pore could also contribute to less than perfect transmission. One way to model a pore with less than perfect transmission is to add a term for the energy barrier that the molecule must overcome for transmission. For a pore with an energy barrier, E_B, for a given molecule equations {1-22} through {1-24} will have an additional term for the transmission probability, P_t, as a function of the energy barrier of [17]

$$P_t = e^{-\frac{E_B}{k_b T}} \qquad \{1\text{-}25\}$$

Of course the energy barrier will depend on the gas species for a given pore. Accounting for the transmission probability due to an energy barrier equations {1-22} and {1-24} become

$$N = N_0 e^{-\frac{A}{V}\sqrt{\frac{k_b T}{2\pi m}}t} e^{-\frac{E_B}{k_b T}} \qquad \{1\text{-}26\}$$

$$\frac{dN}{dt} = \frac{A e^{-\frac{E_B}{k_b T}}}{\sqrt{2\pi m k_b T}} \Delta p \qquad \{1\text{-}27\}$$

For a graphene membrane typical to this thesis (5 μm in diameter covering a cylindrical cavity of depth 300nm, see Chapters 4 and 5) with one 3 Å circular pore in a graphene membrane the time constant, τ_c, from equation {1-22}[5] for perfect transmission of hydrogen at room temperature would be $\tau_c \approx 0.2\,\mathrm{s}$ and thus all the gas in the cavity would escape on the order of seconds. From equation {1-24} the pressure normalized leak rate $\frac{dn}{dt}\Big/\Delta p$[6] for hydrogen going

[5] The time constant is defined as $\tau_c = \frac{V}{A}\sqrt{\frac{2\pi m}{k_b T}}$

[6] $\frac{dn}{dt}$ is used here since it is the molar flow rate which differs from $\frac{dN}{dt}$ by a factor of Avogadro's number.

through one 3 Å circular pore in a graphene membrane is $\frac{dn}{dt}\Big/\Delta p \approx 1\times10^{-20}$ mol s^{-1} Pa^{-1}. These calculated leak rates for a 3 Å pore are orders of magnitude faster than what is observed in Chapter 5 which suggest there is indeed an energy barrier leading to slower transport than predicted by classical effusion.

For traditional membranes with thicknesses similar to or larger than the mean free path of the molecule Poisuille flow, Knudsen diffusion, and surface diffusion are the dominant transport mechanisms. surface diffusion can occur in the pore when a gas is adsorbed to the pore surface and is mobile on the surface. The permeability of a porous membrane taking into account Poisuille flow, Knudsen diffusion, and solution diffusion mechanisms is given by [18]

$$F_0 = \frac{\varepsilon_p}{\tau}\left[\frac{c_1 r}{M^{1/2}} + \frac{c_2 r^2 \bar{P}}{\eta} + \frac{c_3 D_s}{r}\left(\frac{dx_s}{dp}\right)\right] \qquad \{1\text{-}28\}$$

where c_1, c_2, and c_3 are constants for Knudsen diffusion, Poisseuille flow, and surface diffusion terms, respectively, ε_p is the membrane porosity, τ is the pore tortuosity, $\bar{P}$ is the mean pressure in the system, D_s is the surface diffusion coefficient, and x_s is the percentage of occupied surface when compared to a monolayer. The membrane porosity, ε_p, is ratio of pore openings to membrane material and is between 0-1. 0 would be a dense membrane with no pores while 1 would be no membrane. The pore tortuosity, τ, is the ratio of the path length, l, a molecule must travel to the thickness, w, of the membrane i.e. $\tau = \frac{l}{w}$. The tortuosity will be 1 if the membrane has pores that are straight through the membrane with no twist or turns and greater than one for pores where the path length is greater than the membrane thickness.

From equations {1-28} and {1-24} it can be seen that both Knudsen diffusion and classical effusion lead to flow rates that are proportional to $m^{-1/2}$ and thus the ideal separation factor, α, of two gases of masses m_1 and m_2 is the ratio of the inverse square of the mass of the respective gas species. However, much higher selectivities can be achieved if the pore diameter in a membrane is between the size of the two gases being separated. The process of size exclusion separations is known as molecular sieving.

For dense membranes the primary mechanism for transport is solution diffusion. Solution diffusion takes place in three steps. First, gas is absorbed or adsorbed on the membrane surface at the upstream boundary. Second, the gas diffuses through the membrane. Third, the gas desorbs or evaporates on the downstream side of the membrane. The flux, J, of a single gas component through an isotropic dense membrane is given by[19]

$$J = \frac{DS\left(p_1 - p_2\right)}{w} \qquad \{1\text{-}29\}$$

where p_1 and p_2 are the pressures on either side of the membrane, w is the thickness of the membrane, D is the diffusion coefficient, and S is the solubility coefficient. The rate determining parameters in equation {1-29} are the D and S. The product of D and S is known as the permeability coefficient given by [19]

$$C_P = DS \qquad \{1\text{-}30\}$$

The transport of gas species through dense membranes is complicated and not entirely understood. Therefore, predicting the flux and selectivities of various gas species can be difficult especially for polymer systems. As a result most transport models for dense membranes are phenomenological and contain parameters that must be determined experimentally. One

important characteristic of gas separation membranes is that the flux rate is, in general, inversely proportional to the thickness of the membrane. This can be most easily seen in equation {1-29}. For this reason having the thinnest possible membrane is essential for high throughput/high efficiency membranes. With the first isolation of the thinnest possible material, graphene, in 2004 a wealth of theoretical studies have been published investigating the potential benefits of graphene as a separation membrane and results are promising [17], [20], [21], [22], [23], [24], [25].

1.6. Conclusions

In conclusion we have explored the basic concepts and theory relevant to the experimental works presented in Chapter 4, Chapter 5 and Chapter 6 of this thesis. A more in depth approached to studying the mechanics and adhesion of graphene membranes will be explored in Chapter 3. In the next chapter we will go over the properties of graphene.

2. Graphene

2.1. Introduction

Carbon is an amazing element that forms a wealth of materials from polymers to diamond to graphite. In fact carbon is the stuff of life, making up all of the organic compounds necessary for life, including DNA and other biomolecules and biopolymers. Beyond the organic compounds more than 107 synthetic molecules have been created in labs across the world, that rely on the strong and stable carbon-carbon bond [26]. In addition to a wealth of organic compounds that carbon forms it also forms a variety of pure carbon allotropes, different structural forms of an element. This is contrast to the organic compounds which are mostly carbon but are also made up of other elements such as hydrogen, oxygen, and nitrogen.

The ability for carbon to form so many different compounds comes from the fact that its 4 valence electrons have very similar energies, unlike other elements with 4 valence electrons such as silicon. The similar energy levels of the 4 valence electrons allow their wave functions to mix easily and hybridize. This unique hybridization ability sets carbon apart from other elements and allows it to form quasi-0D, quasi-1D, quasi-2D, and 3D structures. Some of the various allotropes are fullerenes (0D), carbon nanotubes (1D), graphite and graphene (2D), and diamond and amorphous carbon (3D). These carbon allotropes allow carbon to exhibit a wide range of physical properties. Figure 2-1 shows some of the most common carbon allotropes.

In this Chapter we will explore graphene, its properties, and some applications for this amazing 2D material.

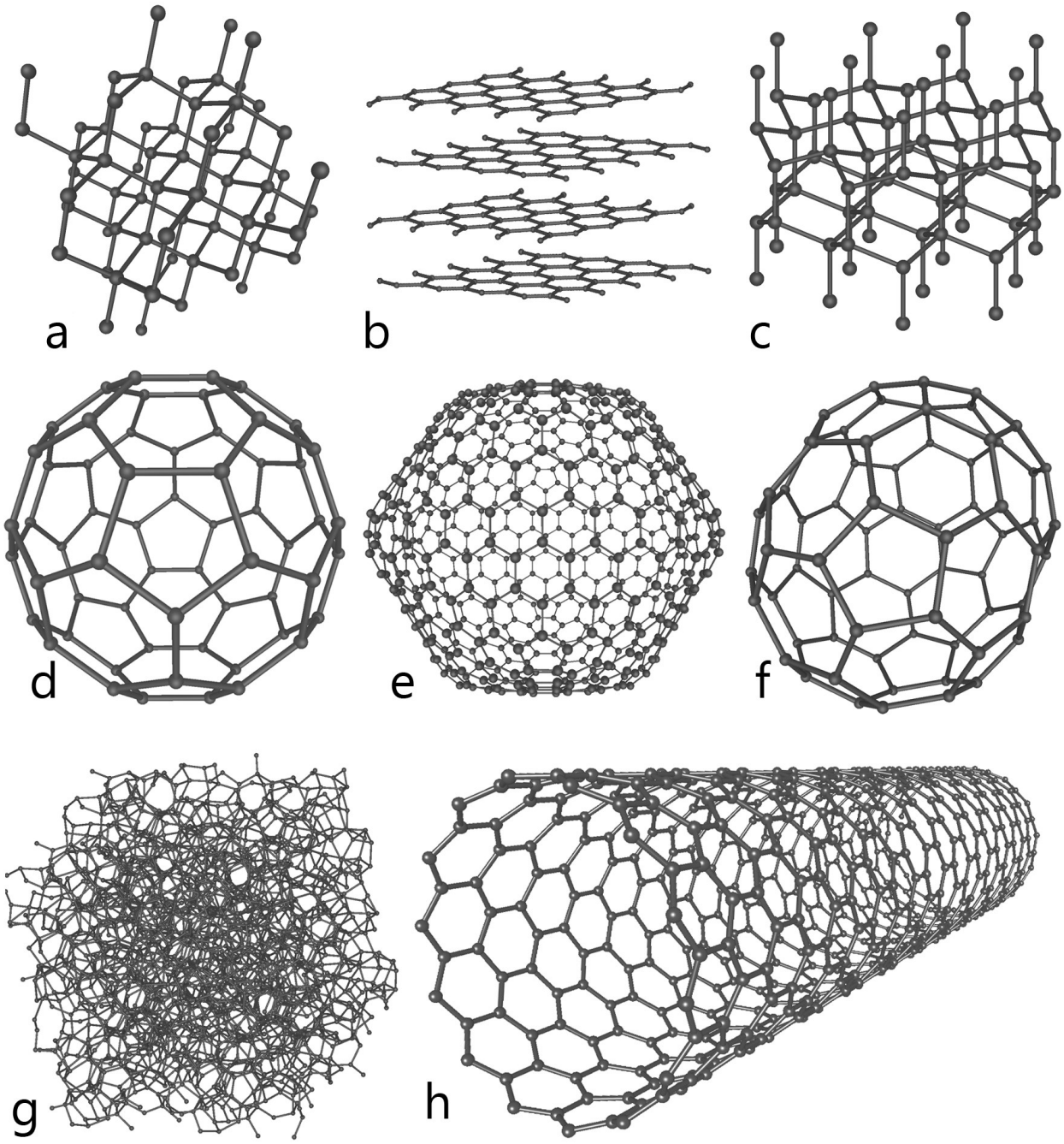

Figure 2-1 Carbon allotropes. (a) diamond, (b) graphite, (c) lonsdaleite, (d)-(f) fullerenes (C_{60}, C_{540}, C_{70}) (g) amorphous carbon, and (h) carbon nanotube. Wikipedia.com: Allotropes of Carbon.

2.2. Graphene

Graphene is a single layer of carbon atoms covalently bonded into a flat hexagonal lattice, a schematic of which is shown in Figure 1-1. When sheets of graphene are stacked together they form graphite, which is used in pencils to write. The individual plans of graphene in graphite are bonded together by the weak van der Waals force, as opposed to the strong covalent bonding in the plane. The weak bonding between sheets of graphene allow them to slide with respect to each other. This is what allows graphite to be used as a writing tool and also as a solid lubricant. The weak inter layer interaction is also what lead to the first isolation of graphene in 2004 by Konstantin Novoselov and Andre Geim [27].

Since its first isolation, graphene, as a research field has increased immensely, much like carbon nanotubes before it. Figure 2-2 shows a plot of the number of publications per year for fullerenes, carbon nanotubes, and graphene. Graphene is still a little behind carbon nanotubes in terms of the number of research articles published each year but it is on pace to pass carbon nanotubes in the next couple of years. The reason for the initial research surge into graphene was its electronic properties. The most notable aspect of graphene's electronic properties is its unique band structure which, in part, arises from its two-dimensional nature. It is also notable that it exhibits the quantum hall effect (QHE). Graphene is a zero band gap semiconductor, in which the conduction and valence band meet at 6 points in k-space. These are known as the Dirac points. Near the Dirac points the band structure has a linear dispersion cone which leads to graphene displaying interesting physics where the electrons behave as massless or relativistic

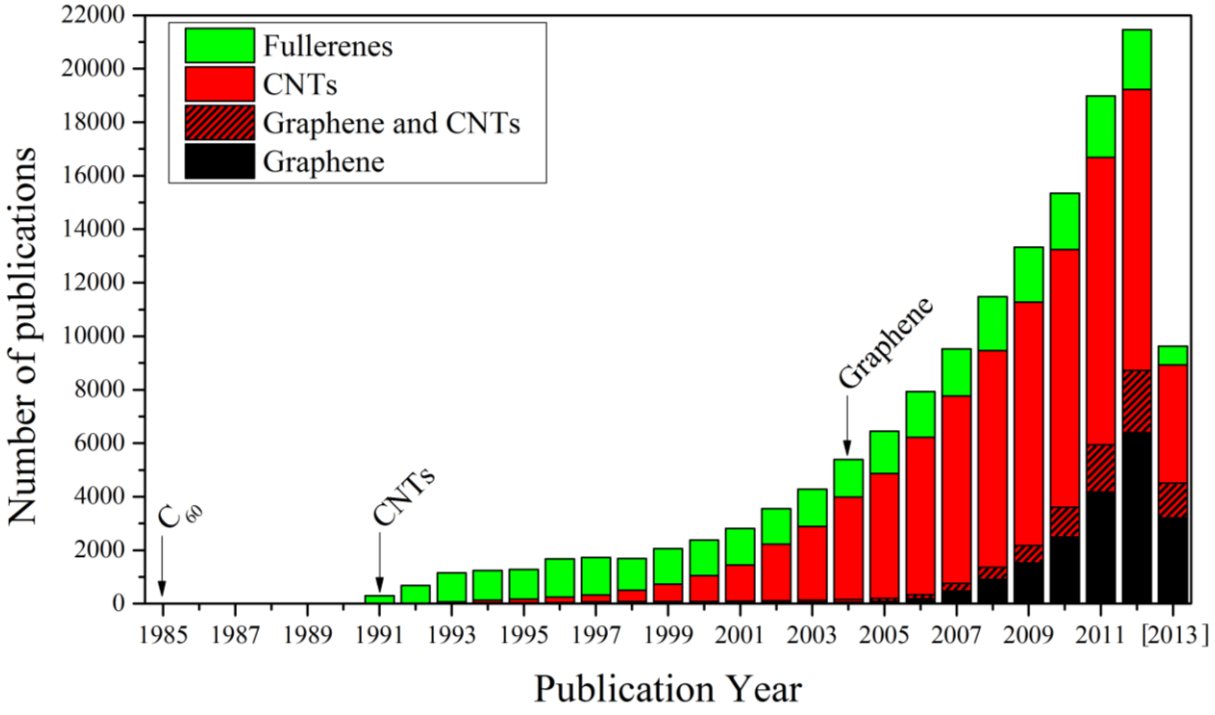

Figure 2-2 Number of publication per year for fullerenes, carbon nanotubes (CNTs) and Graphene. Due to the significant overlap between graphene and CNT publications the publication that cover both topics are plotted as such[7].The recent discovery year of each material is labeled in the graph.

[7] Number of publication was found by doing a topic search by year for each of the subjects on Web of Science. 2013 is for search date of July 8, 2013.

fermions[8]. Using graphene's electronic properties has led to a wide range of proposed applications. In addition to its superior electronic properties it is also nearly transparent, absorbing 2.3% of light per layer of graphene, which has led to additional applications in touch screen sensors and current collectors in solar cells [28].

Graphene is also an amazing material from a mechanical perspective. For being one atom thick, it is amazingly strong and has a Young's modulus (E) of ~1 TPa. Other mechanical properties that are important for graphene are its breaking stress σ_{int} and strain ε_{int} and its bending rigidity B. It was found that graphene has a breaking stress of σ_{int} = 42 N/m and a breaking strain of ε_{int} = 25% [29]. Since graphene is two dimensional its bending rigidity is unlike that of ordinary materials where the bending rigidity is defined by the Young's modulus and the thickness of the material (see equation {1-11}). In continuum mechanics the bending rigidity originates from simultaneous stretching and compression of the deformed material. Since graphene is only one layer of atoms the continuum model breaks down because there is not a top and bottom surface to bend and stretch. Instead the resistance to bending is an intrinsic property of the material that arises from interactions of the π and σ bonds. It should also be noted that the thickness of a monolayer of graphene cannot be unambiguously defined in the continuum sense [30]. As a result the bending rigidity of graphene is much less than the value derived from continuum mechanics [9], [10], [31]. Through molecular dynamics simulations the bending rigidity is estimated to be $B \approx$ 1-2 eV [32], [33] for single layer graphene and is 2 orders of magnitude lower than two and few layer graphene [9].

[8] In the interest of brevity I will leave it to the reader to explore the electronic properties of graphene and carbon nanotubes in the following resources [189][190].

A direct measure of the bending rigidity remains difficult due to the fact that the bending rigidity is so small that it will not mechanically dominate a system enough to be easily measured independently. Measurements on bilayer and multilayer graphene have been conducted and measurements for multilayer graphene agree well with the predicted values [34], [35]. A study by Lindahl *et al*. measured the bending rigidity of bilayer graphene and reported a bending stiffness of 35 eV [36] which is lower than predicted value of 160 eV from *ab initio* calculations [9]. Lindahl *et al*. also estimated the bending rigidity for monolayer graphene to be 7 eV but due to a limited number of data points they admit this is not an accurate measure of the bending stiffness [36].

2.2.1. Graphene Fabrication

The first successful technique for isolating graphene is known as the Scotch tape method, or mechanical exfoliation [37]. The Scotch tape method is remarkably simple. It consists of putting a piece of graphite on Scotch tape and then sticking the Scotch tape together and peeling it apart until the piece of tape is covered with a thin layer of graphite (Figure 2-3). Next, the graphite covered tape is then pressed onto an oxidized silicon wafer and upon peeling the tape off of the wafer they then looked under a microscope. Using this technique occasionally lead to micron sized pieces of single and few layer graphene. This technique is great for producing small scale yet high quality graphene samples for scientific research and proof of concept experiments. In fact this is the technique used to for the experiments in chapters 4 and 5.

The Scotch tape method only produces small amounts of graphene at a time and it is unpredictable as to the size and location of the graphene flakes produced. For this reason much of the research into graphene has been focused on scaling up the production of graphene. The

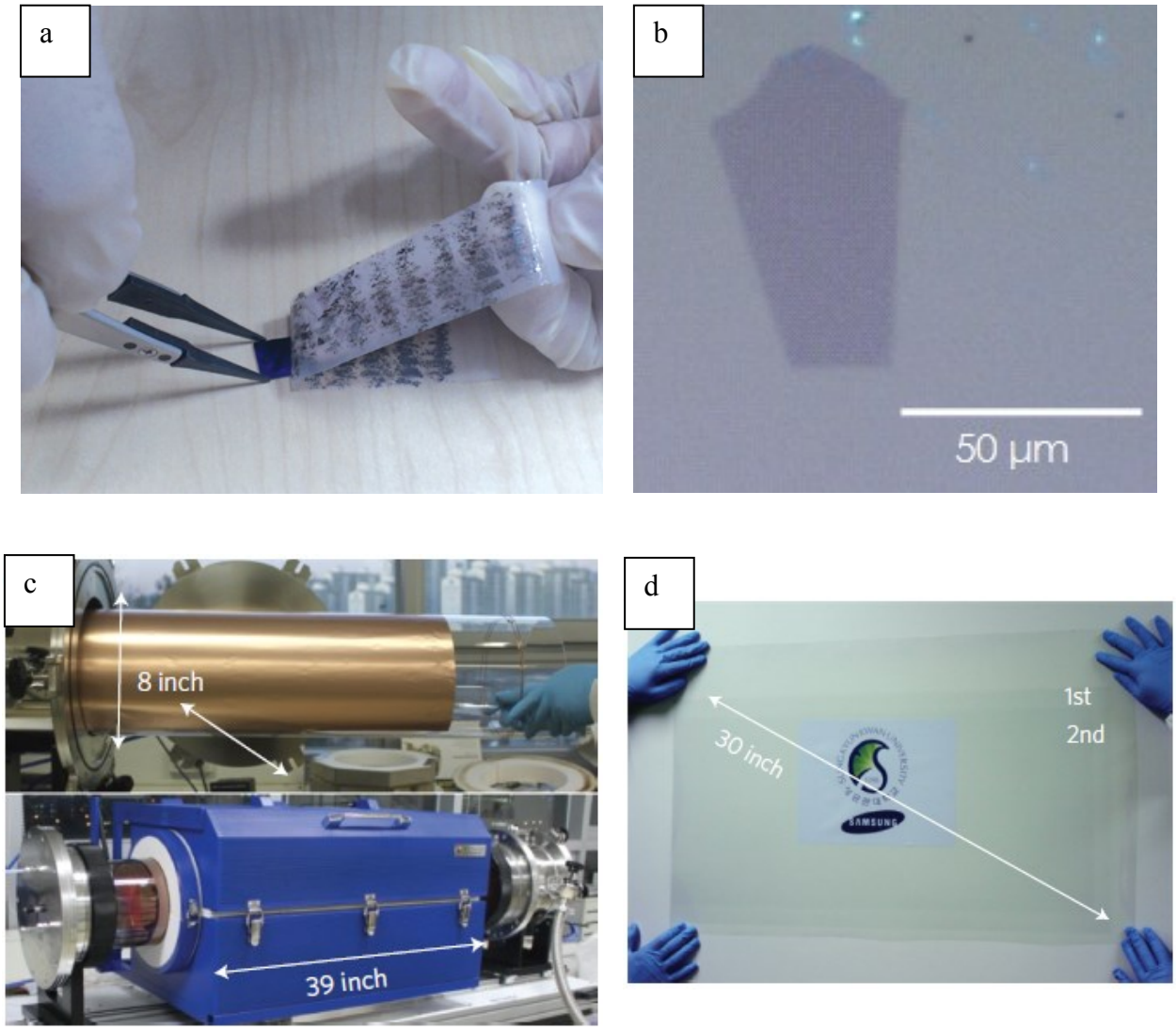

Figure 2-3 (a) Scotch tape method for exfoliating graphene from bulk graphite [38]**. (b) Optical image of graphene flake exfoliated onto 90nm of SiO_2. (c) Graphene being grown on copper by CVD in an 8 inch tube furnace. The final product is a graphene film 30 inches diagonal. (d) 30 inch graphene film transferred to a polymer support** [39]**.**

most promising results came in 2009 when several groups used Chemical Vapor Deposition (CVD) to grow few layer graphene on nickel [6], [40] and single layer graphene on copper [41]. Both of these techniques allowed for the CVD grown graphene to be transferred to arbitrary substrates [42], [43], [44], [45]. Quickly following the discovery of CVD grown graphene groups around the world began to grow graphene films, one such group grew graphene films 30 inches across (see Figure 2-3c and d) [39].

2.2.2. Raman Spectroscopy

Raman spectroscopy is used to measure the vibrational modes in a crystal structure. Raman works by measuring the energy shift of light due to inelastic scattering with phonon vibrations in the crystal lattice. The energy shift, or Raman shift, can then be correlated to a vibrational mode. Raman spectroscopy has quickly become a power full tool for characterizing graphene. It can be used to verify the number of layer [46], [47], probe defects in the crystal lattice [48], determine the amount of strain [49], [50], measure thermal conductivity [51], and detect electronic doping [52]. The Raman spectrum of graphene can also provide insight into all sp2-bonded carbon allotropes since it is their fundamental building block [53]. Raman spectroscopy is perhaps the ideal characterization method for graphene. It is fast and non-destructive, offers high resolution, gives both structural and electronic information, and is applicable to both laboratory and mass production scales [53][54]. Even before the first Raman spectrum of graphene was taken in 2006 it had already become the one of the most popular techniques for characterizing fullerenes, nanotubes, diamond, and a variety of other carbon systems [47], [55].

Figure 2-4a shows the Raman spectrum of graphite and exfoliated graphene. The two main peaks, that are visible, are located at 1580 cm^{-1} and 2700 cm^{-1}, known as the G and 2D peaks respectively. The G peak is due to degenerate carbon-carbon atom vibration while the 2D peak is a higher order double resonance of the breathing mode. There is also a peak at 1350 cm^{-1}, known as the D peak, which is invisible in pristine graphene but becomes visible when there is a break in symmetry in the breathing mode of the aromatic ring. This break in symmetry can be due to absorbates, impurities, or the presence of sp-3 bonding. Figure 2-4b shows the spectrum of defective graphene with the peaks labeled. the D peak is the characteristic peak for defects in graphene while the D', D+D", D+D' and 2D' are higher order modes. A more in depth review of Raman spectroscopy of graphene can be found in reference [53].

Starting from single layer graphene, as layers are added the G peak will increase in intensity, with respect to the 2D peak, but will retain its shape (Figure 2-4c). In contrast the 2D peak will change shape when layers are added up to ~5 layers where the spectrum looks similar to that of graphene (Figure 2-4c). Looking at the 2D peak shape is a convenient way to determine the number of layers for fewer than 5 layers. A more sophisticated method for determining the number of layers can be used which was presented by Koh, et, al. (2011) and is used in Chapters 4 and 5 [46]. The method consists of comparing the ratio of the integrated peak intensity of the G peak (I(G)) of graphene to the silicon (Si) peak (I(Si)). Since each layer of graphene absorbs 2.3% of light comparing the ratio of the peak intensity provides a way to reliably count the number of layers. Figure 2-4d shows the ratio I(G)/I(Si) for n=1 to n=10 layers showing a stepwise increase in the ratio which can be used to determine the number of graphene layers. Other more subtle variations such as precise peak position and width can be used to give us more information about graphene but they are outside the scope of this thesis.

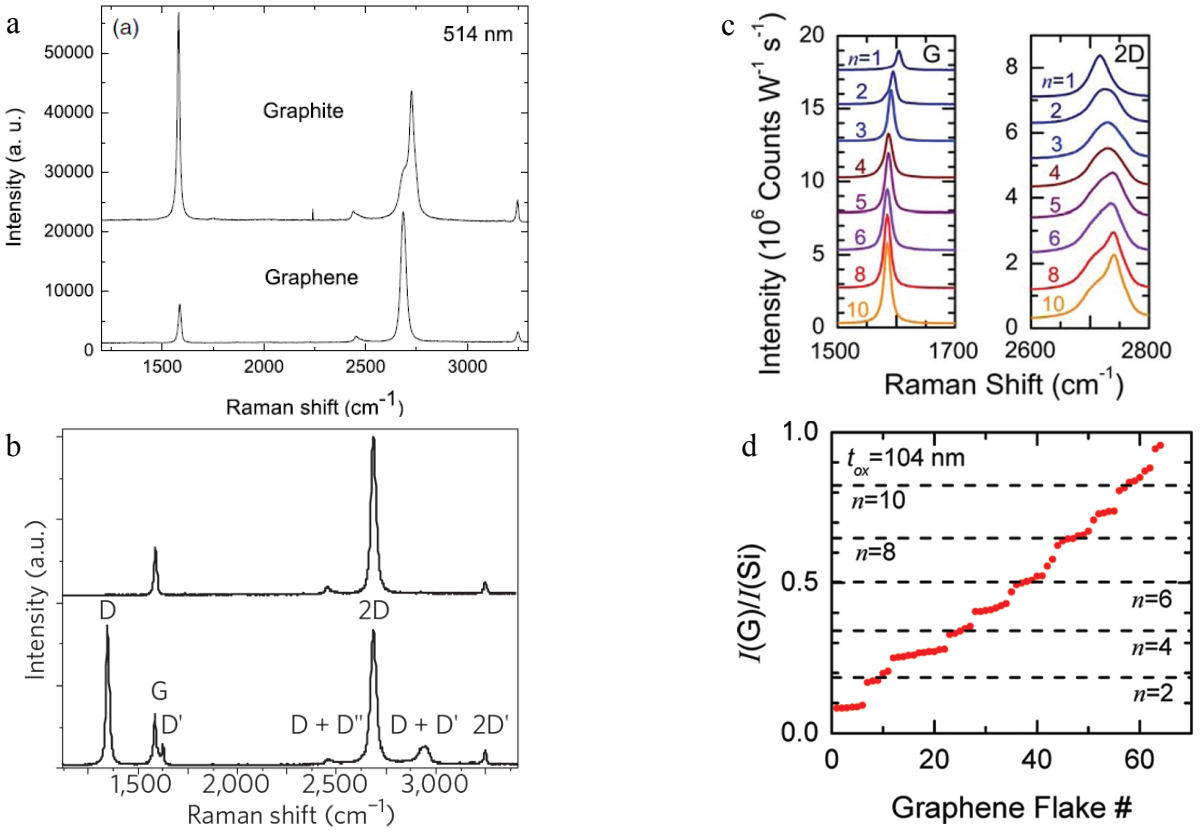

Figure 2-4 (a) Raman spectrum of graphite and exfoliated graphene (from [47]**). (b) Raman spectrum of pristine graphene (top) and defective graphene (bottom) (from** [53]**). (c) Evolution of the G and 2D peaks from *n*=1 to *n*=10 layers of graphene. (d) Ratio of intergrated intensity for *n*=1 through *n*=10 layers showing the stepwise increase. (c) and (d) are from** [46]**.**

2.2.3. Graphene as a Membrane Material

Not long after its initial isolation, Bunch *et al* experimentally demonstrated that graphene, in its pristine form, is impermeable to all standard gas atoms including helium [56]. Soon after, theoretical papers began to emerge to explain the origin of graphene's impermeability [57]. The impermeability of graphene is attributed to its high crystal quality, low defect density, and the fact that the electron density of graphene's aromatic rings is large enough to repel atoms and molecules trying to pass through [17], [57]. Due to its impermeability, pores must be made in the graphene lattice to allow for selective transport of molecules.

The first theoretical study on graphene as a separation membrane was on the selective transport of ions across nanopores in a graphene sheet with different functional groups terminating the pore [24]. This study showed the viability of graphene as an ion separation membrane showing selectivity to anions or cations depending on pore functionality. Jiang *et al* followed this up with the seminal theoretical study of porous graphene as a membrane for gas separations [17]. Jiang *et al* studied both the permeability and selectivity of both nitrogen and hydrogen terminated pores in graphene and showed remarkable potential of graphene as a gas separation membrane for the separation of H_2 and CH_4. Figure 2-5a shows the mixed nitrogen and hydrogen terminated pore and Figure 2-5c shows the pore size due to the electron cloud. Their results showed an amazing H_2 permeance of 1 mol m^{-2} s^{-1} Pa^{-1} for a porous graphene membrane with a selectivity of 10^8 for H_2/CH_4. This result is a 10^7 improvement in permeance and a 10^5 to 10^7 improvement in selectivity over state of the art silica membranes. Additionally Jiang *et al* calculated an even higher selectivity for their all H-terminated pore of 10^{23} (Figure 2-5b & d). A number of other studies have shown similarly remarkable gas separation properties

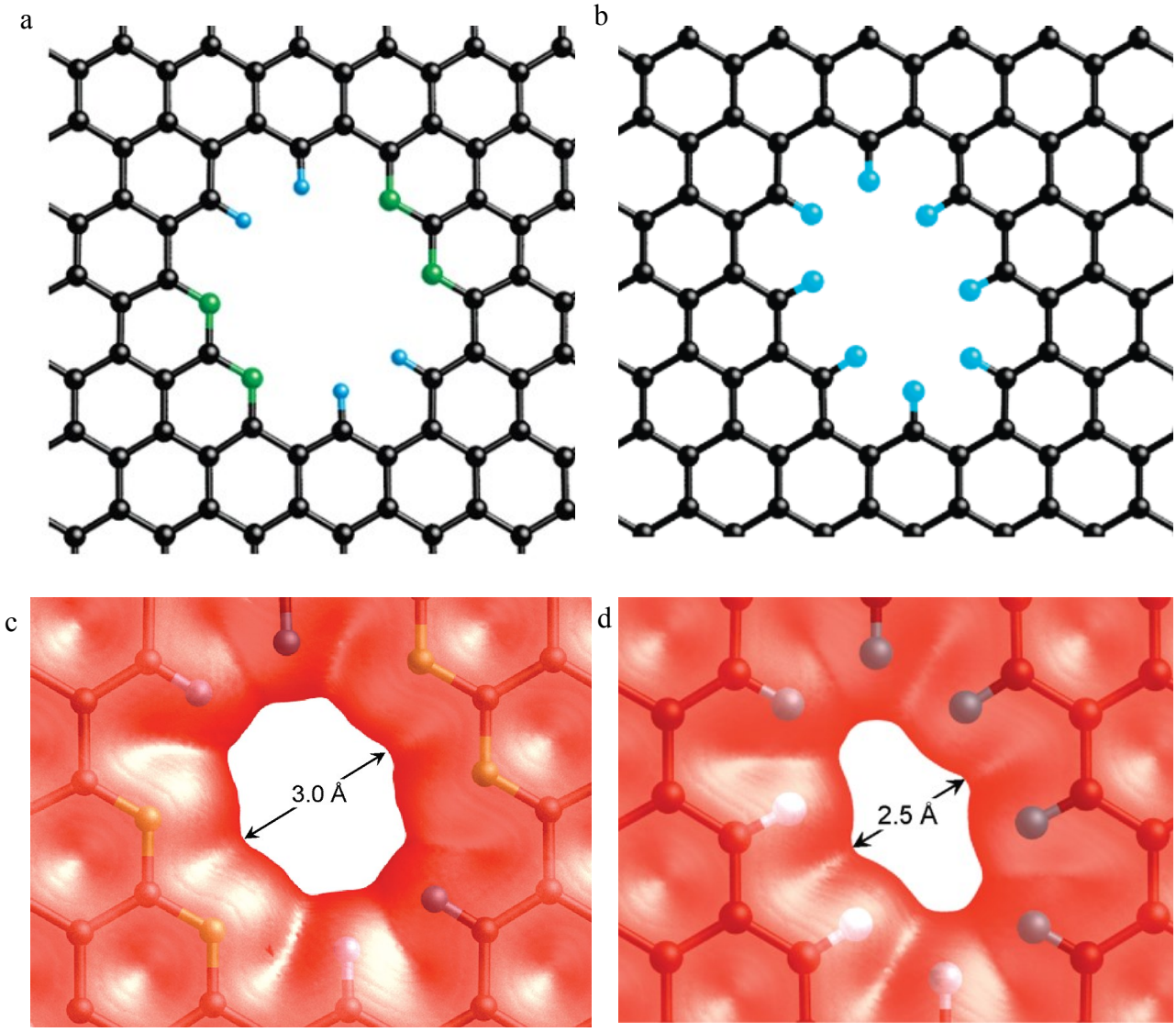

Figure 2-5 Graphene pores with mixed nitrogen (green) and hydrogen (blue) termination (a) and all hydrogen terminated pore (b). Equivalent pore size from electron density calculations for nitrogen and hydrogen terminated pore (c) and pure hydrogen terminated pore (d). Adapted from [17].

of porous graphene with pores of varies sizes and functionalization [21], [22], [23], [58]. Perhaps even more remarkably, recent theoretical studies have shown that porous graphene has the ability to separate isotopes of helium and hydrogen gasses[59], [60], [61], [62].

Despite the promise of graphene as a gas separation membrane, prior to this work, no experimental results have demonstrated its utility for gas separations. In Chapter 5 of this thesis the first work on porous graphene as a gas separation membrane will be presented.

2.3. Conclusions

In this chapter we have explored the properties and some applications of graphene as well as other allotropes of carbon. Table 2.1 summarizes some of the properties of graphene that are relevant to this thesis. In the next chapter we will explore the mechanics and adhesion of membranes.

Table 2.1 Summary relevant properties of pristine graphene.

Property	**Symbol**	**Value**
C-C bond length	d	1.42 Å
Graphite interlayer spacing	w	3.35 Å
Optical Absorbance (per layer)	A	2.3%
Young's Modulus	E	1 TPa
Poisson ratio	v	0.16
Breaking Stress	σ_{max}	42±4 N/m
Breaking Strain	ε_{max}	0.25
Intrinsic bending rigidity (monolayer)	B	1-2 eV

3. Mechanics and Adhesion of Membranes

3.1. Introduction

Dating back to the dawn of recorded history, humans have contemplated the origin of what causes bodies to move and what causes others to be stuck in place, i.e. natural forces. The ancient Greeks postulated that only two forces, one attractive and one repulsive, were needed to describe all natural phenomena, love and hate [63]. Improvement on the ideas of the Greeks has continued for over 2000 years leading modern physicist to accept four fundamental interactions in nature, electromagnetism, gravitation, and the nuclear weak and strong interactions. Despite the wealth of knowledge attained on interactions by scientist and the amazing predictive capabilities that quantum mechanics has brought, much still remains to be explored and understood when it comes to the understanding of intermolecular and surface forces. One of the conclusions from quantum mechanics, by way of the *Hellman-Feynman theorem*, is that all intermolecular forces can be attributed to arising from electrostatic interactions from the subatomic particles that make up atoms and molecules. Although this seems, at first glance, to have solved all the "problems" when it comes to intermolecular interactions, fortunately for graduate students such as myself, exact solutions to the Schrödinger equation remain hard to come by, often being intractable, even for a system as simple as two hydrogen atoms interacting in a vacuum.

One such case in which there remains much to be understood in terms of intermolecular interaction is that of graphene, a two-dimensional hexagonal crystal of carbon atoms, interacting with its environment. Single layers of graphene were first isolated on an SiO_2 for electrical measurements [20]. Many subsequent studies involving graphene have also been carried out with

graphene on an SiO_2 surface due to the ability to easily identify even single layer graphene optically on both 90 nm and 285 nm thick oxide layer on an Si wafer [64], [65]. Since much of the graphene research and applications center around graphene on an SiO_2 substrate and layers of graphene adhering together, many of the theory and modeling of graphene have focused on graphene interacting with itself and an SiO_2 substrate [66]. Additionally, a number of recent experimental efforts have focused on measuring the adhesion energy of graphene on a number of surfaces [67], [68], [69], [70]. In this thesis, a pressurized blister test was used to test both the mechanical properties and the adhesive properties of graphene adhered to an SiO_2 substrate. Therefore, the rest of this chapter will focus on the relevant adhesion theory as well as bulge and blister testing techniques will be explored.

3.2. A Brief History of Adhesion

The first theory and experimental measurement of adhesion came in the 1880s when Hertz studied the contact mechanics of solid glass spheres of radius R_1 and R_2 pressed together with a load P [71]. Hertz demonstrated that the size and shape of the contact area was attributed to the elastic deformation of the bodies in contact. The contact radius, a_0, for two elastic spheres is given by:

$$a_0^{\,3} = \frac{3}{4}\left(k_1 + k_2\right)\frac{R_1 R_2}{R_1 + R_2}P \qquad \{3\text{-}1\}$$

where k_1 and k_2 are related to the elastic constants, the Poisson ratio, v, and Young's modulus, E, of the material each sphere is made of, such that $k_i = (1 - v_i^2)/E_i$. A similar expression for a sphere contacting a rigid flat surface can be expressed as (a schematic of which is shown in Figure 3-1)

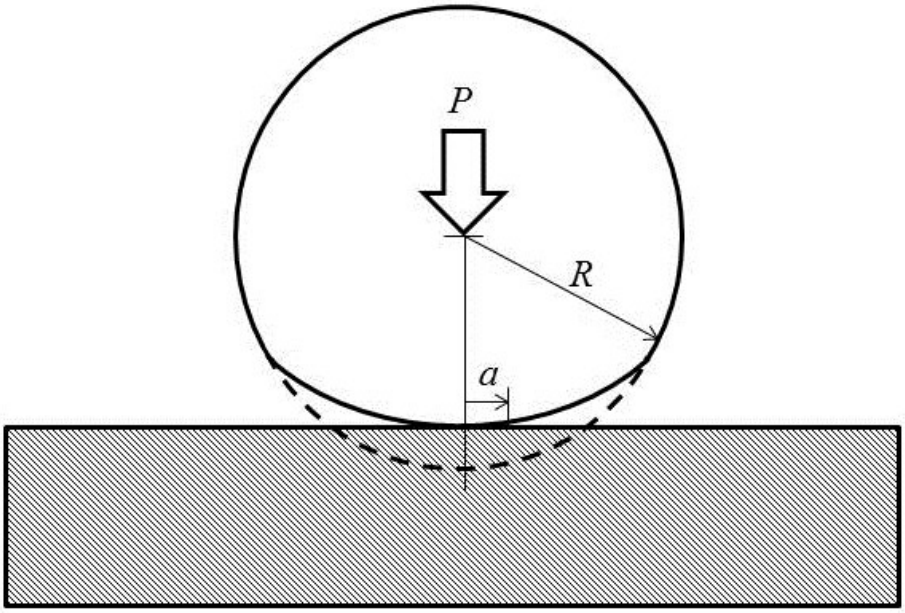

Figure 3-1 Sphere of radius *R* pressed into a rigid surface with a load *P*. The contact radius of the sphere is given by *a*.

$$a_0^3 = \frac{3}{4} kRP \qquad \{3\text{-}2\}$$

Later it was shown that as the load, P, was reduced to zero the contact area of the spheres was larger than predicted by the Hertz model and that the contact area approached a finite value as the load approached zero, whereas the contact area would approach zero as the load approached zero for the Hertz model. The Hertzian contact model was advanced further in the 1930s by papers by both Bradley, and Hamaker. Bradley proposed that deformations in contacting bodies could be accounted for by surface adhesion between the contacting bodies [72]. Shortly after Bradley, Hamaker proposed that the surface forces were related to the density of atoms of the contacting bodies, ρ_1 and ρ_2 [73]. Now known as the Hamaker constant, A, the interaction parameter relating the density of atoms and the van der Waals forces is given by

$$A = \pi^2 C \rho_1 \rho_2 \qquad \{3\text{-}3\}$$

where C is the atom-atom pair potential given by the van der Waals interactions.

In 1971 Johnson, Kendall, and Roberts (JKR) extended the theory presented by Hertz to account for surface forces at the interface of two contacting bodies. The work done by JKR was based on experiments on rubber spheres where they observed a larger contact area than predicted by Hertz. The model put forth by JKR (known as the JKR model) was the result of a balance between the elastic energy stored in the system, the mechanical energy from the applied load, and the surface energy. Taking into account the three energy terms, JKR came up with a modified Hertz relationship given by [74]

$$a_0^3 = \frac{R}{K}\left[P + 3\Gamma\pi R + \sqrt{6\Gamma\pi RP + (3\Gamma\pi R)^2} \right] \quad \{3\text{-}4\}$$

Where Γ is the adhesion energy or Dupré energy, R is radius of the two contacting spheres (i.e. $R = \frac{R_1 R_2}{R_1 + R_2}$), and K is the effective elastic constants of the two contacting spheres (i.e. $1/K = E_1/(1-\nu_1^2) + E_2/(1-\nu_2^2)$).

Derjaguin, Muller, and Toporov (1975), known as the DMT model, used a thermodynamic approach to account for the surface forces in the contact area. In contrast to the JKR model the DMT model assumes that the surface forces outside of the contact region are small and therefore deformation of the spheres outside the contact zone is assumed to be Hertzian. This assumption is valid for large values of the Young's modulus. The contact area predicted by the DMT model is [75]

$$a_0^3 = \frac{3}{4}\frac{R}{K}\left[P + 2\Gamma\pi R \right] \quad \{3\text{-}5\}$$

Both the JKR model and the DMT model approach the Hertz solution for an adhesion energy of zero, $\Gamma = 0$. After examining both the JKR and DMT models it appears that these two theories are competing and contradictory. It was later determined by Tabor in 1977 that the two theories were actually at opposite ends of the adhesion spectrum [76]. On one end of the spectrum is the JKR model which is valid for materials with low Young's modulus, large sphere radius, and large surface forces, while the DMT model is more suitable for materials with high Young's modulus, small sphere radius, and small surfaces forces. The spectrum between the JKR and DMT models is parameterized by μ and given by [76]

$$\mu = \left(\frac{R\Gamma^2}{K^2 z_0^{\,3}} \right)^{1/3} \qquad \{3\text{-}6\}$$

where z_0 is the equilibrium separation of the contacting bodies. The JKR model is valid for large values of μ (μ>5.0) and the DMT model is valid for large values of μ (μ<0.1). Mueller et al. (1980) showed by using the Lennard-Jones potential that the spectrum between the two models is continuous between the JKR value (μ=5.0) and the DMT value (μ=0.1) [77].

3.2.1. Surface Forces

As mechanical structures and devices shrink down to the nano-scale the influence of surface forces play an increasing role due to a decrease in separation distances and a decrease in structural stiffness with decreasing device dimensions. The surface forces that are often dominant in micro- and nano-scale systems is that of the van der Waals forces. As shown by London, the van der Waals forces arise from temporary dipole moments from the instantaneous position of the electron cloud of an atom or molecule [78]. The temporary dipole moment can then polarize the electrons in a nearby atom or molecule resulting in an attractive energy that falls off as, $1/r^6$, where r is the distance between the two interacting atoms or molecules. This relationship only holds true for ranges from approximately 1-10nm, the range at which the nearby atom or molecule can be assumed to respond immediately [79]. As the separation of the molecules is increased the neighboring molecule responds more slowly due to the finite speed of information travel between the two molecules, which is governed by the speed of light [80]. The retarded van der Waals force, as it is known, has an energy distance dependence of, $1/r^7$, and is valid for distances greater than ~100nm [79]. Taking the assumption that the normal and retarded van der Waals forces are additive the respective forces between two flat smooth surfaces are,

$$F = \frac{A}{6\pi d^3} \qquad \{3\text{-}7\}$$

and

$$F = \frac{B}{d^4} \qquad \{3\text{-}8\}$$

where d is the separation of the two surfaces, A is the Hamaker constant, and B is the retarded van der Waals constant [80].

Interfacial energy or adhesion energy can be estimated from the surface energies or surface tensions of dissimilar surfaces. If the surface energies, the excess energy at the surface of a material compared to the bulk, of the two surfaces are known, γ_A and γ_B, then the adhesion energy of the surfaces can be estimated as [63]

$$\Gamma_{AB} = 2\sqrt{\gamma_A \gamma_B} \qquad \{3\text{-}9\}$$

Often γ_A and γ_B are found by measuring the contact angle of various liquids, of known surface tension, to the solid surfaces[9].

Electrostatic forces caused by static image charges on a flat conducting plate can also add to the adhesion energy. This is the case when a flat conducting plate is near or in contact with a dielectric substrate with trapped charges. The work needed to move a charge from a distance d from the conducting plane out to infinity is

$$W = \frac{1}{4\pi\varepsilon_0}\frac{q^2}{4d} \qquad \{3\text{-}10\}$$

[9] Surface energy, γ, and adhesion energy, Γ, are in units of J/m^2

where q is the fundamental charge, d is the distance the charge is away from the conducting plane and ε_o is the permittivity of free space [81]. The adhesion energy of the two surfaces is given by taking equation {3-10} and multiplying by the charge density, ρ, of the trapped charges giving an adhesion energy of

$$\Gamma = \frac{1}{4\pi\varepsilon_0}\frac{q^2}{4d}\rho \qquad \{3\text{-}11\}$$

Other surface forces such as capillary forces can also play a role in the adhesion of micro- and nano-scale mechanical structures and devices [82], [83], [84]. The capillary force, is the result of relative humidity in the environment and develops between two hydrophilic surfaces.

3.3. Methods of Adhesion Testing in Thin Films

In order to test the adhesion energy between surfaces, a number of experimental techniques have been devised including peel tests, pull tests, scratch tests, surface force apparatus, atomic force microscopy, collapsed single/double cantilever beam tests, and blister tests [85], [86], [87], [88], [89], [90]. The adhesion tests I will focus on are the blister tests, of which a variation is used in Chapter 4 to test the adhesion of graphene to an SiO_2 substrate. One of the advantages of the blister test over other methods is that it can also be used to measure the elastic constants of the adhered thin film, before delamination. After delamination the blister test can be used to measure the adhesion energy between the two surfaces. This is also referred to as the bulge test when only measuring the mechanical properties of thin films. Before going any further into the bulge and blister tests I will briefly review some typical methods for measuring adhesion energy of thin films.

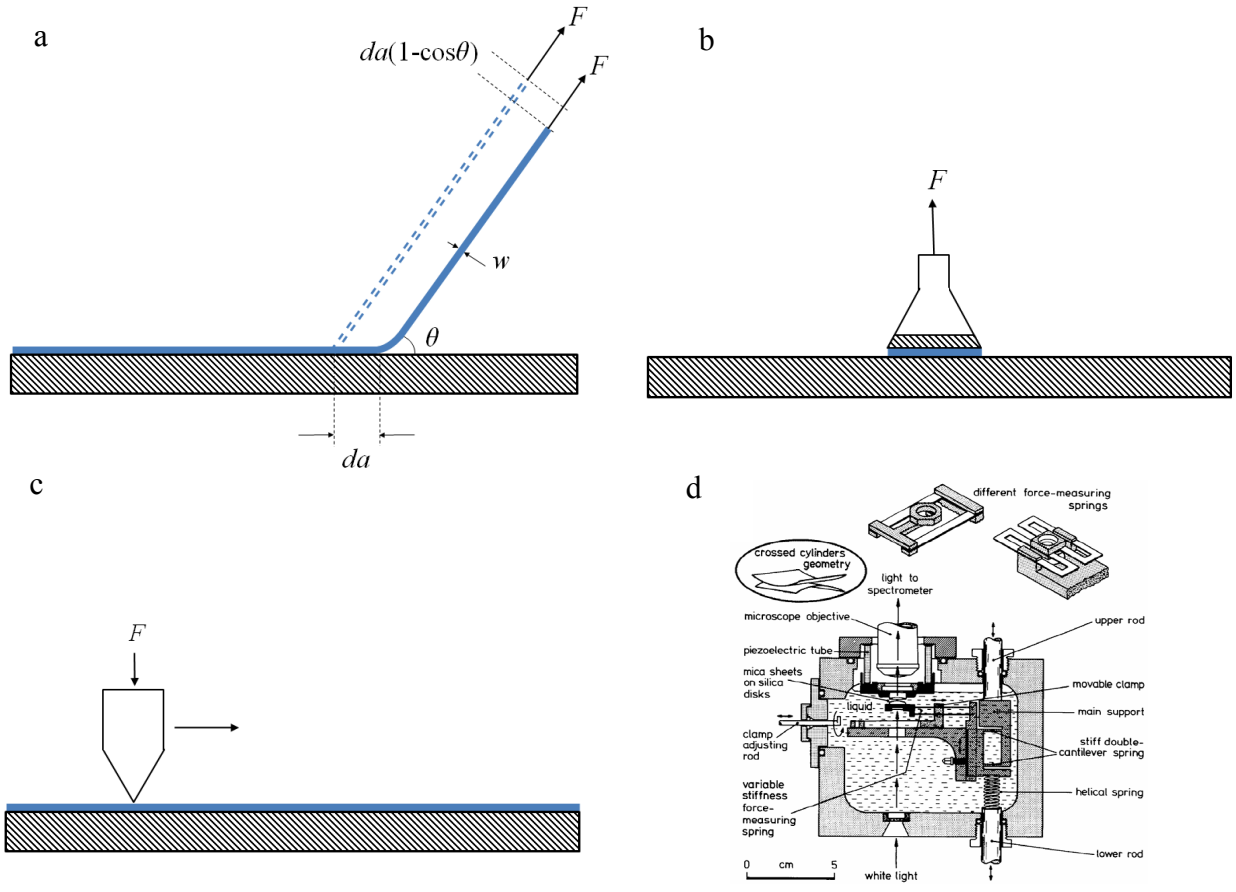

Figure 3-2 Schematics of (a) the peel test, (b) the pull test, (c) the scratch test, and (d) the surface force apparatus. (d) is adapted from reference [63]**.**

The **peel test** is a widely practiced test in the thin film industry due to its simplicity. A diagram of the peel test can be seen in Figure 3-2a. This method uses a blanket film that is then patterned into a strip, of width *b*. The patterning can either be done by photolithography or by scribing. Once the strips are released a force, *F*, is then applied at some angle θ to one end of the strip until it starts to peel from the substrate. The adhesion can be calculated from the force needed to peel the thin film and the strain, ε, the film underwent due to the applied force by [91]

$$\Gamma = \frac{F}{b}\left(1 - \cos\theta + \frac{\varepsilon}{2}\right) \qquad \{3\text{-}12\}$$

Studies have shown that the peel test is an accurate measure of the adhesion strength only under the condition, $6EF / w\sigma_y^2 < 1$, where σ_y is the yield stress of the adhered film [92], [93]. This condition requires much thicker films to be tested than would be used in typical application and is one of the main limitations of this technique.

A popular test that is often used in comparison with the peel test is the **pull test**. The pull test consist of a pin attached to the adhered film by either epoxy or solder (see Figure 3-2b) [94], [95]. The interface is then stressed through the application of a normal force, *F*, applied to the pin and the failure strength of the interface is measured. For an adhered circular film of radius, *a*, thickness, *w*, and bulk modulus, *B*, the adhesion energy can be found by the expression [95]

$$\Gamma = \frac{F^2 w}{2\pi^2 a^4 B} \qquad \{3\text{-}13\}$$

The limitations of this test arise from difficulties in assuring that (i) the applied force is normal to the surface, having no shear components, (ii) the failure occurs at the proper interface, not the one that is glued or soldered, and (iii) no defects in the film are present to act as stress

concentrations. A variation known as the **topple test**, where the force is applied to the pin parallel to the substrate, can be used to overcome the need for precise alignment needed with the pull test but the second and third problems still apply.

The **scratch test** consists of dragging a stylus across the surface of a film and increasing the applied load until the interface fails (Figure 3-2c). Films tested using this method are typically thin metal films [96], [97], [98]. Extracting the adhesion energy values is extremely complex which is attributed to the various failure modes experienced during this test. Only a few or the failure modes can be correlated to the interfacial energy [99]. Nevertheless, the scratch test remains widely used in the protective coating industry since the test closely resembles that of the final applications.

The **surface force apparatus** (SFA) is an instrument used to measure the interfacial interactions between two crossed mica cylinders in a prescribed environment [63]. A schematic of the SFA can be seen in Figure 3-2d. Though the cylinders typically used are made of mica they can be coated with thin layers of polymers or metals to test the surface interactions of various materials. The force sensitivity and distance resolution for the SFA are about 10 nN and 1 Å, respectively. Likewise the **atomic force microscope** (AFM) can also be used to measure the interfacial forces [63]. A sharp tip (radius ~10-100nm), attached at the end of a cantilever beam, can be used to measure the interfacial forces between the tip and a substrate. Separation between the substrate and the tip is varied with a resolution on the order of 1 Å and the force is determined my measuring the cantilever deflection. The resulting force-displacement data can be integrated to find the work of adhesion in a variety of environments, including liquids and ultrahigh vacuum.

The **collapsed single/double cantilever beam test** is advantageous over other techniques for testing adhesion in MEMS and NEMS structures because it uses the mating of micromachined surfaces to measure the adhesion. This is in opposition to other techniques where the surfaces are mated together and then pulled about or idealized cylinder/tip interactions are used to measure surface forces to predict the adhesion. This method involves fabricating cantilever beams suspended over a substrate and then forcing the cantilevers into contact using electrostatic loading, mechanical loading, or capillary forces from drying [100], [101], [102], [103], [104], [105]. Typically beams of various length are fabricated in series on a chip and the critical length for stiction is determined after the loading is applied to the cantilevers. A schematic of an adhered beam can be seen in Figure 3-3a while an SEM image of the critical length measurement can be seen in Figure 3-3b. This can also be done with doubly clamped beams although single cantilever beams are more commonly used.

3.4. Bulge Test

Since being first reported by Beams in 1959, bulge testing has become one of the standard techniques for measuring the in-plane mechanical properties of thin films, such as Young's modulus, Poisson's ratio, and residual stresses [106], [107], [108]. In its simplest form, the bulge test is carried out by applying a pressure, p, to a thin circular film of radius, a, resulting in a maximum deflection, δ, clamped at the boundary. A schematic of the bulge test of a thin circular clamped film can be seen in Figure 3-4. Often films are clamped with a retaining ring as shown in Figure 3-4 but the films can also be bonded to the substrate, either chemically of with an adhesive agent. In the case of graphene the films are clamped to the substrate by the van der Waals forces [56], [109], [110]. In order to relate the experimentally measured data with the in-plane mechanical properties of the thin films being tested a number of theoretical and numerical

a

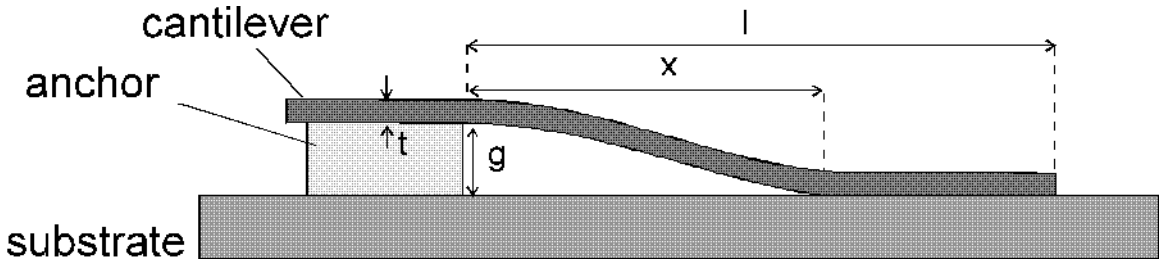

b

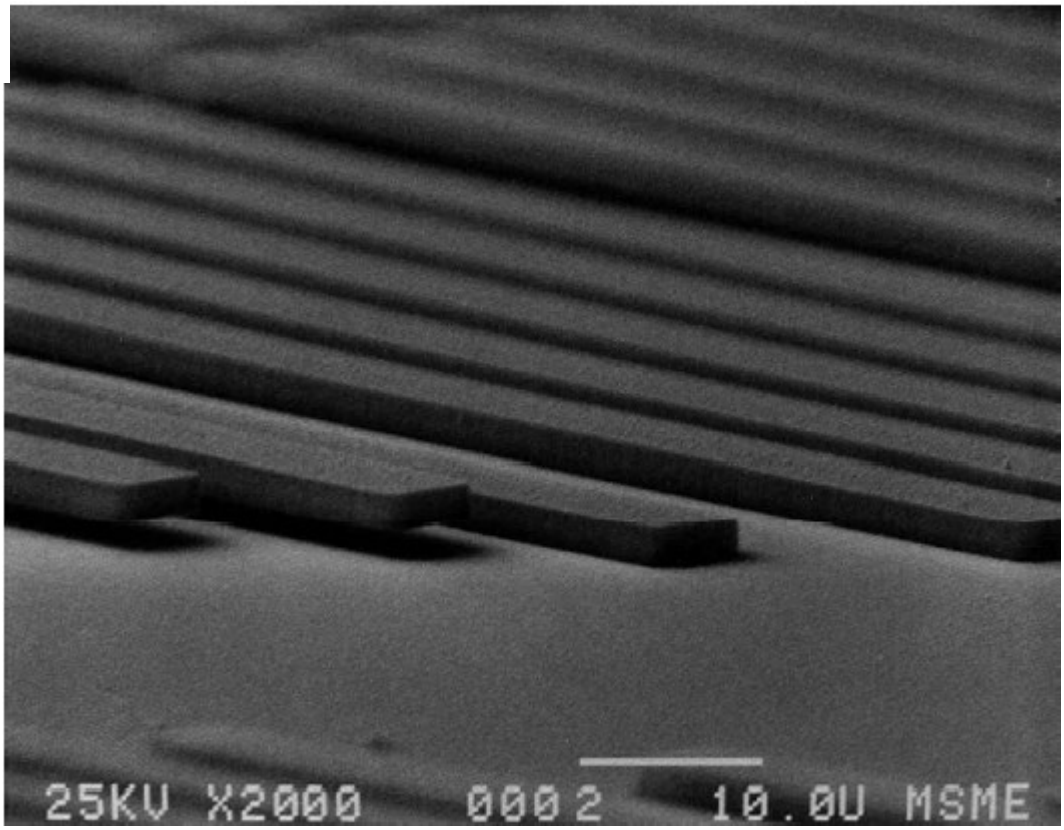

Figure 3-3 (a) schematic of the cantilever beam test [105]**. (b) SEM image of the critical beam length test** [102]**. Beams smaller than the critical length are still suspended while beams over the critical length are stuck to the substrate.**

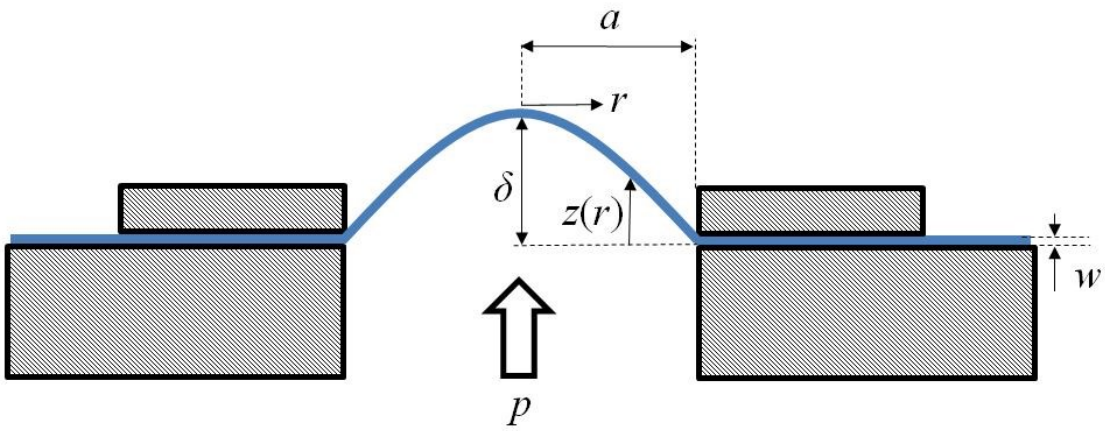

Figure 3-4 Schematic of bulge testing of thin films.

solutions have been put forth. There are two regimes to consider when pressurizing a thin film, the plate regime and the membrane regime. The plate regime is valid when the deflection of the thin film is on the order of the thickness of the membrane. At higher deflections, several times greater than the thickness of the membrane [111], the membrane model is dominant. The difference in the plate and membrane models is that the plate model takes into account the bending rigidity of the thin film where the membrane model assumes only in-plane stretching. The von Karman equations are used to solve for the equation of a linear elastic plate [112], [113]. Often numerical methods are used to solve for the plate mechanics of thin films [111], [114] but here we present an analytical solution similar to that presented by Timoshenko, Yue *et al.*, and Wang *et al.* [113], [115], [116].

3.4.1. Plate Mechanics

The deflection profile of a thin circular plate, of radius, a, and maximum deflection, δ, with a pressure difference applied across it is assumed to be [115], [116]

$$z(r) = \delta\left(1 - \frac{r^2}{a^2}\right)^2 \qquad \{3\text{-}14\}$$

where r is the distance from the center of the membrane. Equation {3-14} satisfies the boundary condition of zero-slope at the edge of the plate. The radial displacement is assumed to take the form

$$\mathrm{u}(r) = r\left(a - r\right)\left(c_1 - c_2 r\right) \qquad \{3\text{-}15\}$$

where c_1 and c_2 are two parameters to be determined.

By equations {3-14} and {3-15} the radial and circumferential components of the strain are obtained as

$$\varepsilon_r = c_1\left(a-2r\right)+c_2 r\left(2a-3r\right)+\frac{8\delta^2 r^2\left(a^2-r^2\right)^2}{a^8} \qquad \{3\text{-}16\}$$

$$\varepsilon_\theta = \left(a-r\right)\left(c_1-c_2 r\right) \qquad \{3\text{-}17\}$$

The circumferential strain is zero at the edge (r=a). The elastic strain energy consist of two parts, the elastic stretching strain energy, $U_s(r)$, and elastic bending terms, $U_b(r)$. The two terms are

$$U_s(r) = \frac{Ew}{2\left(1-\nu^2\right)}\left(\varepsilon_r{}^2+2\nu\varepsilon_r\varepsilon_\theta+\varepsilon_\theta{}^2\right) \qquad \{3\text{-}18\}$$

$$U_b(r) = \frac{D}{2}\left[\left(\frac{d^2z}{dr^2}\right)^2+\frac{1}{r^2}\left(\frac{dz}{dr}\right)^2+\frac{2\nu}{r}\frac{dz}{dr}\frac{d^2z}{dr^2}\right] \qquad \{3\text{-}19\}$$

The total potential energy of the plate is then

$$\Pi(a,\delta,c_1,c_2) = 2\pi\int_0^a\left[U_s(r)+U_b(r)\right]rdr-2\pi(p-p_0)\int_0^a z(r)rdr \qquad \{3\text{-}20\}$$

At equilibrium, the two constants c_1 and c_2 can be determined by setting $\frac{\partial\Pi}{\partial c_1}=\frac{\partial\Pi}{\partial c_2}=0$ which results in

$$c_1 = \frac{(179-89\nu)}{126}\frac{\delta^2}{a^3} \qquad \{3\text{-}21\}$$

$$c_2 = \frac{(13\nu-79)}{42}\frac{\delta^2}{a^4} \qquad \{3\text{-}22\}$$

Now we can set $\frac{\partial \Pi}{\partial \delta} = 0$ to obtain the non-linear plate solution given by

$$\Delta p = 64\eta \frac{Ew\delta^3}{a^4} + 64\frac{D\delta}{a^4} \qquad \{3\text{-}23\}$$

where $\eta = \frac{7505 + 4250\nu - 2791\nu^2}{211680(1-\nu^2)}$.

The volume of the bulge for the plate solution given by the profile in equation {3-14} is

$$V = \frac{\pi}{3} a^2 \delta \qquad \{3\text{-}24\}$$

For a plate with a deflection less than its thickness, and thus the bending rigidity is dominant, the linear plate analysis is sufficient [115]. The linear plate analysis ignores non-linear terms in the strain energy along with the stretching term of the strain energy. As a result equation {3-23} becomes

$$\Delta p = \frac{64D\delta}{a^4} \qquad \{3\text{-}25\}$$

which is the exact solution to the linear plate equations [111], [113], [115], [116].

3.4.2. Hencky's Membrane Solution

The other limiting case is when the deflection is much larger than the thickness so the bending rigidity can be neglected. Again the von Karman equations are solved but this time neglecting the effects of bending rigidity[10]. For this analysis we adopt the series solution of the

[10] This could be done by simply setting D=0 in equation {3-23} but the assumed deflection profile and boundary conditions are for a plate with a significant bending rigidity and therefore are not as accurate as this approach. The finite bending stiffness used in the plate model has an extra boundary condition of zero slope at the boundary.

von Karman equations obtained by Hencky [117] that culminates in a relation between the maximum deflection, pressure difference across the membrane, and the radius of the membrane [91], [118]. The Hencky solution assumes uniform lateral loading. Other membrane analyses use a membrane solution with uniform pressure loading but the Hencky solution has been shown to be most accurate for small graphene membranes such as the ones analyzed in this thesis [110], [115], [116], [119]. We start this analysis with the governing equations for radial and lateral equilibrium, respectively.

$$\sigma_\theta = \frac{d}{dr}\left(r\sigma_r\right) \qquad \{3\text{-}26\}$$

$$\sigma_r \frac{dz}{dr} = -\frac{pr}{2w} \qquad \{3\text{-}27\}$$

where σ_r and σ_θ are the radial and circumferential stresses, respectively, and p is the uniform pressure load. The stress-strain relationships are [120]

$$\sigma_\theta - \nu\sigma_r = Ew\varepsilon_\theta \qquad \{3\text{-}28\}$$

$$\sigma_r - \nu\sigma_\theta = Ew\varepsilon_r \qquad \{3\text{-}29\}$$

and the strain-displacement relationships are

$$\varepsilon_\theta = \frac{u}{r} \qquad \{3\text{-}30\}$$

$$\varepsilon_r = \frac{du}{dr} + \frac{1}{2}\left(\frac{dw}{dr}\right)^2 \qquad \{3\text{-}31\}$$

The boundary conditions at the clamped edge are

$$z(a) = 0 \qquad \{3\text{-}32\}$$

$$u(a) = 0 \qquad \{3\text{-}33\}$$

Combining equations {3-26} through {3-31} the resulting equations are

$$\frac{r}{Ew}\frac{d}{dr}\left[\frac{d}{dr}\left(r\sigma_r\right)+\sigma_r\right]+\frac{1}{2}\left(\frac{dz}{dr}\right)^2 = 0 \qquad \{3\text{-}34\}$$

$$\sigma_r \frac{dz}{dr} = -\frac{1}{2}pr \qquad \{3\text{-}35\}$$

Substituting equation {3-35} into equation {3-34} gives

$$\frac{\sigma_r^{\,2}}{Ew}\frac{d}{dr}\left[\frac{d}{dr}(r\sigma_r)+\sigma_r\right]+\frac{1}{8}p^2 r = 0 \qquad \{3\text{-}36\}$$

Following Hencky, we assume a power series for the total radial stress to obtain the solution

$$\sigma_r = \left(\frac{Ep^2a^2}{64w^2}\right)^{1/3}\sum_{n=0}^{\infty} B_{2n}\left(r/a\right)^{2n} \qquad \{3\text{-}37\}$$

with $B_2 = -1/B_0^{\,2}$, $B_4 = -2/3B_0^{\,5}$, $B_6 = -13/18B_0^{\,8}$, $B_8 = -17/18B_0^{\,11}$, $B_{10} = -37/27B_0^{\,14}$, $B_{12} = -4077/189B_0^{\,17}$, and so on [118], [120], [121]. B_0 is a function of the Poisson ratio, *v*. From this, we can solve for the circumferential stress and the deflection profile to obtain

$$\sigma_\theta = \left(\frac{Ep^2a^2}{64w^2}\right)^{1/3}\sum_{n=0}^{\infty}\left(2n+1\right)B_{2n}\left(r/a\right)^{2n} \qquad \{3\text{-}38\}$$

$$z(\mathrm{r}) = \left(\frac{pa^4}{Ew}\right)^{1/3}\sum_{n=0}^{\infty} A_{2n}\left[1-(r/a)^{2n}\right] \qquad \{3\text{-}39\}$$

with $A_0 = 1/B_0$, $A_2 = 1/2B_0^4$, $A_4 = 5/9B_0^7$, $A_6 = 55/72B_0^{10}$, $A_8 = 7/6B_0^{13}$, $A_{10} = 205/108B_0^{16}$, and so on [118], [120], [121]. We can now find an expression for the maximum deflection, δ, of the membrane where r=0, δ=z(0).

$$\delta = \left(\frac{pa^4}{Ew}\right)^{1/3} \sum_{n=0}^{\infty} A_{2n} \qquad \{3\text{-}40\}$$

We can rewrite this to get the pressure difference as a function of the elastic constants, membrane radius and maximum deflection, and substituting the constant $K(\nu) = \sum_{n=0}^{\infty} 1/A_{2n}^{\,3}$

$$\Delta p = K(\nu)(Ew\delta^3)/a^4 \qquad \{3\text{-}41\}$$

By integrating $z(r)$ over the crack area using equation {3-39}, we can find the area under the bulge to be.

$$V_b = \int z(r) 2\pi r dr = C(\nu)\pi a^2 \delta \qquad \{3\text{-}42\}$$

The constants $C(\nu)$ and $K(\nu)$ can be found by solving for B_0 by satisfying the boundary condition expressed in equation {3-33}, which is

$$\frac{d}{dr}(r\sigma_r) - \nu\sigma_r\Big|_{r=a} = 0 \qquad \{3\text{-}43\}$$

or, equivalently,

$$(1-\nu)B_0 + (3-\nu)B_2 + (5-\nu)B_4 + (7-\nu)B_6 + \ldots \qquad \{3\text{-}44\}$$

As can be seen from equation {3-44} B_0, and thus $C(\nu)$ and $K(\nu)$, vary only with ν [11]. Solving for B_0 in equation {3-44} to get $K(\nu)$, which varies with Poisson's ratio as follows: $K(\nu=0.10)=2.93$, $K(\nu=0.20)=3.22$, $K(\nu=0.30)=3.45$, to $K(\nu=0.30)=4.75$. For the case of graphene, taking $\nu=0.16$, $K(\nu=0.16)=3.09$ and $C(\nu=0.16)=0.524$.

Hencky was the first to report an analytical solution for the simplest case of the pressurized circular membrane [91], [117]. Hencky's solution to the membrane problem was later generalized by the work of Campbell to account for residual stresses in the membrane. The Hencky solution for a thin circular membrane with residual stress, S_0, is given by [121]

$$\Delta p = K(\nu)(Ew\delta^3)/a^4 + (4S_0\delta)/a^2 \qquad \{3\text{-}45\}$$

Campbell showed that the deflection given by equation {3-40} is within 5% of the solution with S_0 taken into account (equation {3-45} when the non-dimensional parameter P>100, where P is given by [121]

$$P = \frac{\Delta p a}{Ew}\left(\frac{Ew}{S_0}\right)^{\frac{3}{2}} \qquad \{3\text{-}46\}$$

Mechanically exfoliated membranes like the ones presented in this thesis often have initial tensions, S_0, between 0.03-0.15 N/m [56], [122], [123]. For typical graphene membranes presented in this work values of a=2.5 μm, Ew=340 N/m and S_0=0.07, the non-dimensional parameter P is about 100 when the pressure load is about 400 kPa [119]. For the membranes presented in Chapter 4 and the first part of Chapter 5, most of the measurements are well above

[11] It is well known that the values of B_0 in Hencky's paper had errors. References [91], [118] corrected Hencky's error and the corrected version is used here.

500 kPa and initial tension can be ignored. For the later part of Chapter 5 membranes measured with the resonance method the pressures are well below 400 kPa and equation {3-45} is needed.

For non-circular plates and membranes, the solution for the problem becomes more complex and a number of solutions exist with the solution from Vlassak and Nix being the most widely used for rectangular and square geometries [106], [107]. Levy put forth an exact solution for pressurized square membranes but the complexity of this solution keeps it from being widely used [107], [124].

At pressures where the clamping conditions of the membrane are no longer sufficient to keep the membrane from sliding or delaminating from the substrate the membrane solutions become more complicated. Although the mechanics of membranes at these elevated pressures becomes difficult to evaluate, it is possible to study the interfacial adhesion energy between the thin film membrane and the substrate on which it is attached. This works best for flexible membranes that are bonded directly to rigid substrates. This is the case for graphene membranes suspended over cavities in a silicon dioxide substrate where the van der Waals forces clamp graphene to the edge of the cavity [56], [110].

3.5. Blister Test

Although the peeling test is a widely used method for testing the adhesion energy of interfaces, a number of problems exist that make this technique less than ideal for measuring thin film adhesion [125], [126]. Due to the ease of implementation and film preparation, the blister test has recently been adopted for measuring the adhesion energy of thin flexible membranes on rigid substrates. Since the first blister test was reported by Dannenberg, the blister test has taken on many other forms [127]. The blister test reported by Dannenberg is known as the **standard**

blister test. A schematic of the standard blister test can be seen in Figure 3-5a. In its simplest implementation, a vertical vent is drilled, either mechanically or chemically etched, through the substrate to create a feed through to apply a constant pressure to the thin film spanning the vent opening. As, p, is increased below the critical pressure, the membrane deflection increases with no debonding. In this regime the test is identical to the bulge test and the mechanical properties of the membrane can be measured. Once p reaches the critical pressure, p_{cr}, where debonding of the thin film begins [118], [125], [128]. The expression for p_{cr} for an axisymmetric blister under constant pressure assuming membrane behavior with Henkey's solution is given by [119]

$$p_{cr} = \left(\frac{4\Gamma}{5KC}\right)\frac{(Ew)^{1/4}}{a_0} \qquad \{3\text{-}47\}$$

where a_0 is the initial blister radius. It can be seen from equation {3-47} that for a constant adhesion energy, Γ, as a_0 is increased the critical pressure will decrease as a result. This leads to unstable blister growth once p_{cr} is reached since the new a_0 upon initial delamination will lower the effective p_{cr} while the applied pressure is still at the initial p_{cr} which is higher. As a result, the blister will grow until the entire film becomes detached from the substrate [118], [125], [128]. Two distinct disadvantages exist with the constant pressure blister test i) the measured adhesion energy is related to the initiation of debonding and not the propagation of debonding, ii) only a single measurement can be obtained per film tested making sample preparation more costly.

Since the time of Dannenberg many improvements and refinements have been made to the standard blister test [91], [129], [130], [131], [132], [133], [134], [135]. In addition to improvements to the standard blister test a number of modified blister test have been devised to overcome some of the short comings of the standard blister test. A few of the modified blister test are the constrained blister test [136], [137], [138],

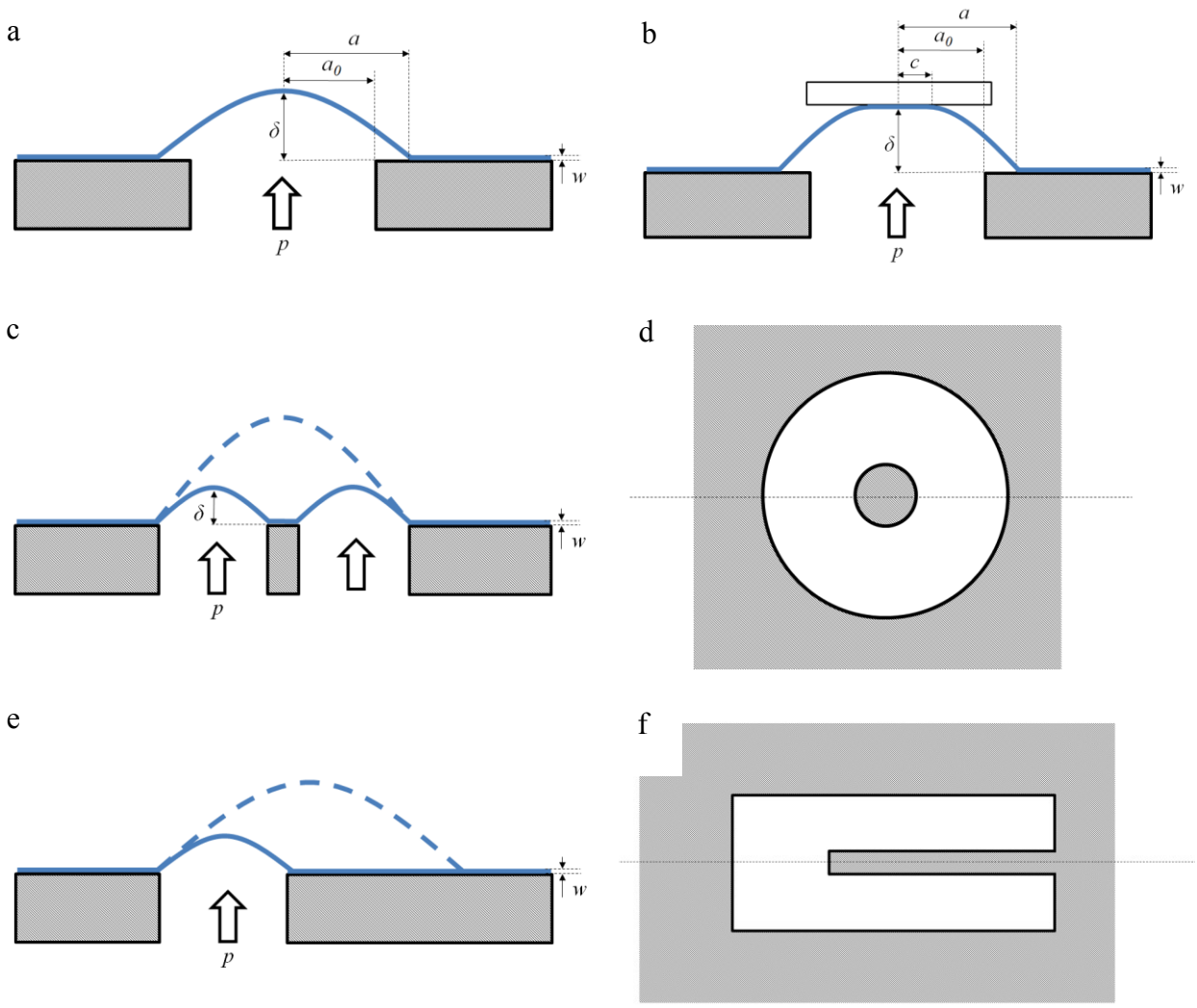

Figure 3-5 Cross-section schematics of blister test methods. (a) standard blister test, (b) constrained blister test, (c) island blister test with (d) top view, and the peninsula blister test with (f) top view. Dashed line in (c) and (e) is the membrane after debonding.

the island blister test [139], [140], the peninsula blister test [141], [142], and two blister tests with modified loading conditions [118], [125].

The **constrained blister test** is similar in geometry to the standard blister test with the addition of a plate positioned parallel to the substrate restricting the vertical deflection of the film. A schematic of the constrained blister test can be seen in Figure 3-4b. The constrained blister test can reduce the risk of film rupture prior to delamination since the constrained on the deflection reduces the stresses in the blister, which are maximum at the center of the blister for the unconstrained case. The constrained blister test also has the advantage of having a nearly constant energy release rate which makes the analysis much simpler. A disadvantage to this approach is that the specimen size must be on the order of tens of millimetres, since the there is a minimum distance at which the constrained plate can be accurately located above the substrate [143]. The size restriction on sample size makes this method unsuitable for small electronic parts such as those used in MEMS.

The **island blister test** developed by Allen and Senturia was first used for measuring thin polymer films on metal and polymer surfaces [139], [140]. A schematic of the island blister test can be seen in Figure 3-5c and d. The island blister test is similar to the standard blister test but in this case a small post is placed in the middle of the membrane. The membrane is initially adhered to the center post. As the pressure is increased to the critical pressure, the film will debond from the center post. From the critical pressure, the adhesion energy can be extracted. The advantage of the island blister is similar to that of the constrained blister test in that it can lower the pressure needed to peel and in turn reduce the stress in the membrane before debonding occurs. Additionally the island blister test includes less dissipative energy in the measurement compared to the standard blister test. The disadvantages to the island blister test are

more complicated sample preparation and analysis along with the fact that crack propagation is usually unstable and only one measurement per prepared membrane can be obtained.

The **peninsula blister test** developed by Dillard and Bao uses a peninsula as opposed to an axisymmetric island in the island blister test. See Figure 3-5e and f for a schematic of the peninsula blister test. The peninsula blister test further reduces the stresses in the film before and during debonding and further reducing the risk of film failure. The peninsula blister test also has the advantage of a constant energy release rate. Added advantages over the island blister test include a larger debond area and additional data points that can be obtained from a single specimen. The downsides to this testing technique are more complicated sample fabrication and more complicated analysis since the sample is no longer axisymmetric [141], [142].

Two alternative blister test have been developed that allow for stable debonding, the **shaft-loaded blister test** and the **pressurized blister test with fixed mass of working gas** [118], [125]. In the case of the shaft-loaded blister test sample preparation starts out similar to the standard blister test with a vent being drilled through the substrate. In this test, a shaft with a spherical cap is used to apply a load P_s to the membrane. Figure 3.6a shows a schematic of the shaft loaded blister test. The shaft is approximated as a point load and a straight edge conical blister profile is assumed. For linear elastic membranes the expression for the adhesion energy is [125]

$$\Gamma = \left(\frac{1}{16\pi^4 Ew}\right)^{1/3}\left(\frac{P_s}{a}\right)^{4/3} \qquad \{3\text{-}48\}$$

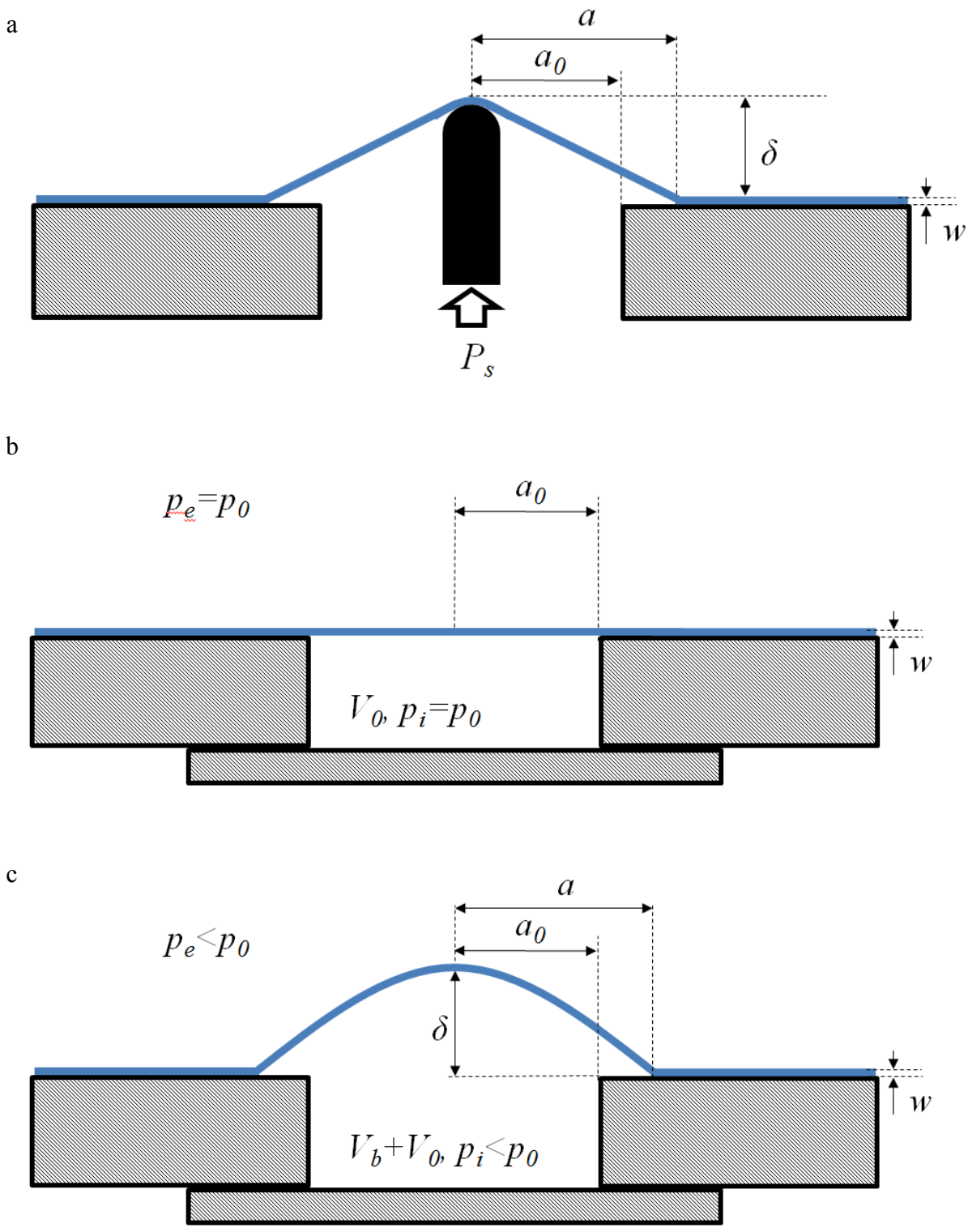

Figure 3-6 Schematics of the standard blister tests with modified loading conditions. (a) is the shaft loaded blister test. (b) and (c) are for the blister test with a fixed amount of working gas. In (b) and (c) the bottom of the cavity is sealed.

The second blister test with stable crack growth is the **pressurized blister test with constant mass of working gas** [118]. Sample preparation is similar to the constant pressure blister test and the shaft loaded blister test except that the substrate cavity created by drilling or chemical etching is sealed from the back side creating a fixed cavity volume under the membrane. Alternatively the hole can be drill in such a way that is does not go all the way through the substrate. This can also be achieved by drilling or etching a cavity in the substrate that does not go all the way through the substrate and then covering the cavity with the thin film membrane that is to be tested. After the cavity is sealed on both sides the cavity, with initial volume V_0, is then filled with an initial pressure of p_0 and the external pressure is also raised to p_0 so that the membrane is flat and no pressure difference exists across the membrane. The membrane is then bulged upward and delaminated by decreasing the external pressure to p_e. Upon lowering the external pressure the pressure difference across the membrane causes it to bulge upward increasing the volume of the cavity due to the deflection of the membrane. As the volume, $V = V_b + V_0$, increases the working gas expands isothermally causing the internal pressure, p_i, to decrease according to the idea gas law $p_i V = nRT$. The pressure difference across the membrane, $\Delta p = p_i - p_e$, will eventually cause the blister to debond from the substrate increasing a. The system will reach equilibrium once the debonding ceases leading to stable blister growth. The expression for the adhesion energy for this blister test is given by

$$\Gamma = \frac{5C}{4(KEw)^{1/3}}(\Delta p a)\left(\frac{4p_i p_0 - p_i^2 + p_e p_0}{4p_i p_0 - p_i^2 - 3p_e p_0}\right) \qquad \{3\text{-}49\}$$

where C and K are constants that depends on Poisson's ratio, and are defined previously.

3.6. Membrane Dynamics

The above sections describe membranes with a static load applied to them and are therefore in equilibrium. Membranes can also vibrate much like the mass spring system presented in chapter 1. An example of this is a drumhead. The frequency of a circular membrane under tension caused by a pressure difference Δp and initial tension S_0 can be described using the following equations [144]

$$f = \frac{2.404}{2\pi}\sqrt{\frac{S}{\rho_A a^2}} \qquad \{3\text{-}50\}$$

$$S = \frac{\Delta p a^2}{4\delta} + S_0 \qquad \{3\text{-}51\}$$

where f is the fundamental resonant frequency of the membrane, S is the total tension in the membranes, and ρ_A is the area mass density of the membrane. In equation {3-51} Δp is given by equation {3-45}.

3.7. Conclusions

A modified version of the constant mass of working gas blister test is presented in chapter 4 of this thesis to test the adhesion of graphene membranes on a thermally grown silicon oxide substrate. In addition to testing the adhesion of graphene, the mechanics of the graphene membranes were also tested before the graphene membranes delaminated from the substrate. The resonance of a graphene drum head resonator is used in chapter 5 to study the gas permeation though porous graphene membranes.

4. Ultrastrong Adhesion of Graphene Membranes

4.1. Introduction

As mechanical structures shrink down to the nanoscale regime, the influence of the van der Waals forces play an increasing role in device performance. Graphene is attractive for nanomechanical systems [109], [145] because it's Young's modulus and strength are both intrinsically high, but the mechanical behaviour of graphene is also strongly influenced by the van der Waals force [29], [56]. For example, this force clamps graphene samples to substrates, and also holds together the individual graphene sheets in multilayer samples. Here we use a pressurized blister test to directly measure the adhesion energy of graphene sheets with a silicon oxide substrate. We find an adhesion energy of 0.45 ± 0.02 J/m^2 for monolayer graphene and 0.31 ± 0.03 J/m^2 for samples containing two to five graphene sheets. These values are larger than the adhesion energies measured in typical micromechanical structures and are comparable to solid-liquid adhesion energies [63], [83], [103]. We attribute this to the extreme flexibility of graphene, which allows it to conform to the topography of even the smoothest substrates, thus making its interaction with the substrate more liquid-like than solid-like.

4.2. Experimental Geometry

Optical images of the devices used for this study are shown in Figure 4-1a-d. Graphene-sealed microcavities were fabricated by mechanical exfoliation of graphene over predefined microcavities (diameter ~5 μm) etched in an SiO_2 substrate. An array of circles with diameters of 5 and 7 μm was first defined by standard photolithography on an oxidized silicon wafer with a silicon oxide thickness of 285 nm. Reactive ion etching was then used to etch the circles into

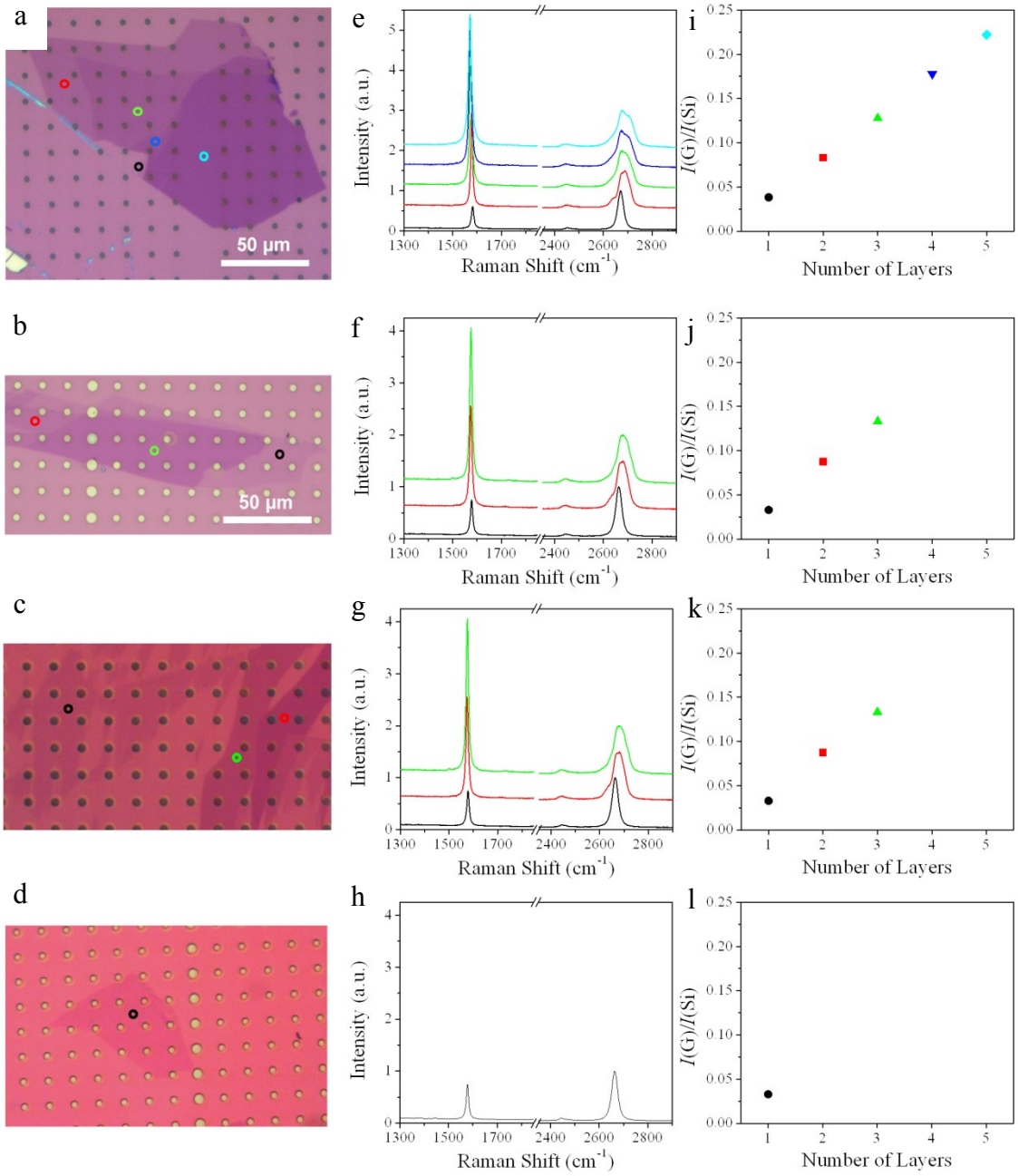

Figure 4-1 (a)– (d) Optical images of the graphene flakes used in this study. The graphene flakes were exfoliated on a wafer with 285nm oxide and wells etched in the SiO_2. The graphene flake in (a) has suspended regions of 2-5 layers while the flakes in (b) and (c) have regions of 1-3 layers and regions and the flake in (d) has only monolayer suspended graphene. The number of graphene layers was verified with a combination of Raman spectroscopy, optical contrast, AFM measurements, and elastic constants measurements. The colored circles denote the location at which Raman spectroscopy was taken (denoted as follows: black 1 layer, red 2 layers, green 3 layers, blue 4 layers, and cyan 5 layers). (e)– (h) Raman spectrum from the graphene flakes in (a)-(d). The color of each curve corresponds to the spot on the optical image. (i)– (l) Ratio of the integrated intensities of the first order silicon peak, I(Si), and the graphene G peak, I(G) (i.e., I(G)/I(Si)) for the corresponding color Raman spectrum sound in (e)-(h).

cylindrical microcavities with a depth of 250–300 nm, leaving a series of microcavities on the wafer. Mechanical exfoliation of natural graphite using Scotch tape was then used to deposit suspended graphene sheets over the microcavities [37]. Four exfoliated graphene flakes were used, yielding membranes with between one and five graphene layers, which were suspended over microcavities and clamped to the SiO_2 by the van der Waals force. The number of graphene layers was verified using a combination of Raman spectroscopy, optical contrast, AFM measurements, and elastic constants measurements [46], [47]. Figure 4-1e-h show the Raman spectrum taken from the spots of corresponding color from the respective flakes in Figure 4-1a-d, black is one layer, red is two layers, green is three layers, blue is four layers, and cyan is five layers. The ratio, I(G)/I(Si), of the integrated intensity of the first order optical phonon peak of silicon, I(Si), to the graphene G peak, I(G), was used to determine the number of layers in accordance with ref. [46]. The aforementioned ratios are shown in Figure 4-1i-l. Using this technique for determining the number of layers was verified using a combination of optical contrast, AFM measurements, as well as the measured elastic constants of the membranes [64], [146]. The close agreement of the Raman spectroscopy technique used here with the optical contrast, AFM measurements, and the measured elastic constants validates the utility of this technique. Of the 54 membranes measured, there were 14 one-layer, 13 two-layer, 18 three-layer, 4 four-layer, and 5 five-layer membranes. Six two-layer membranes, 4 three-layer membranes and 1 four-layer membrane were damaged before reaching the highest measured pressures.

After exfoliation the internal pressure in the microcavity, p_{int}, is equal to the external pressure, p_{ext} (ambient pressure) (Figure 4-2). In this state, the membrane is flat and adhered to

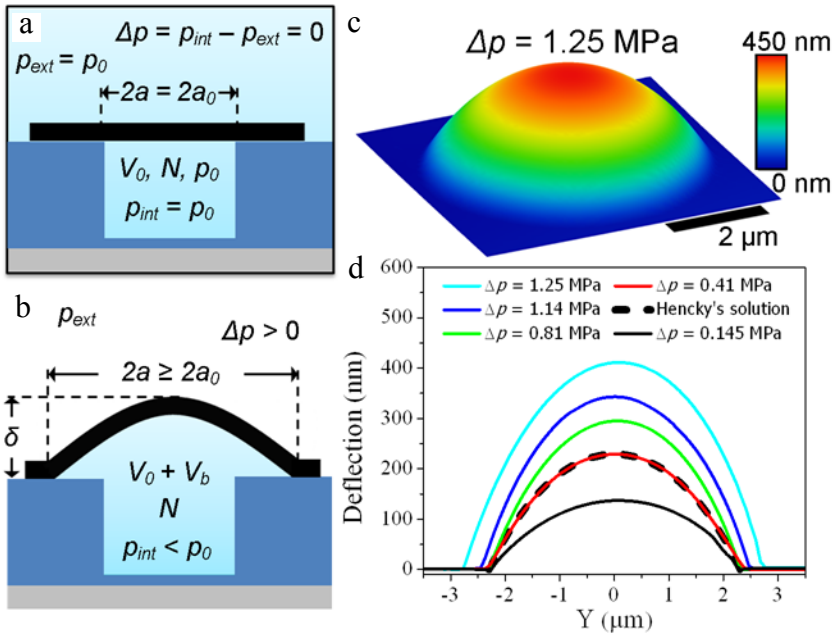

Figure 4-2 (a) and (b) schematics illustrating the pressurization of the graphene membranes. After exfoliation the pressure inside the microchamber is that of the ambient atmosphere, p_{ext}. (a) The graphene membranes are then placed in a pressure chamber and over pressurized, to p_0, for 4-6 days to bring $p_{int} = p_0$. (b) Upon removing the graphene membranes from the pressure chamber there is a pressure difference across the membrane causing it to bulge upward and eventually delaminate from the substrate at a critical pressure, causing the radius, a, to increase. (c) Three dimensional AFM rendering of the deformed shape of a monolayer graphene membrane with Δp =1.25 MPa. (d) Sequence of AFM line cuts from a typical monolayer graphene membrane as the pressure is increased from The dashed black line is the theoretical shape for Δp =0.41 MPa.

the substrate, and confines N number of gas molecules inside the microcavity. To create a pressure difference across the graphene membrane, we placed the sample in a pressure chamber and used nitrogen gas to increase, p_{ext} to p_0, which we call the "charging pressure" (Figure 4-2a). Devices were left in the pressure chamber at p_0 for four to six days to allow p_{int} to equilibrate to p_0. This is thought to take place through the slow diffusion of gas through the SiO_2 substrate [56]. We then removed the device from the pressure chamber, whereupon the pressure difference ($p_{int} > p_{ext}$) causes the membrane to bulge upward and the volume of the microcavity to increase (Figure 4-2b). An atomic force microscope (AFM) was used to measure the shape of the graphene membrane, which we parameterize by its maximum deflection, δ, and it's radius, a (Figure 4-2b).

This technique allows us to measure δ and a for different values of p_0. Figure 4-2d shows a series of AFM line cuts through the center of a monolayer membrane as p_0 is increased. At low p_0, the membrane is clamped to the substrate by the van der Waals force and δ increases with increasing p_0. At higher p_0 (for example, $p_0 > 2$ MPa), in addition to an increased deflection, we also observe delamination of the graphene from the SiO_2 substrate which leads to an increase in a (Figure 4-2d). In Figure 4-3, we plot δ versus p_0 for all the devices measured. The deflection increases nonlinearly until $p_0 \sim 2.5$ MPa and δ then begins to increase more rapidly. The blister radius stays constant until $p_0 \sim 2.5$ MPa and then abruptly increases with increasing p_0 (Figure 4-4).

4.3. Adhesion Energy

At large p_0 (for example, > 3.0 MPa), stable delamination occurs, with a increasing and thus Δp decreasing with increasing p_0 (Figure 4-5). All of the pressurized graphene membranes

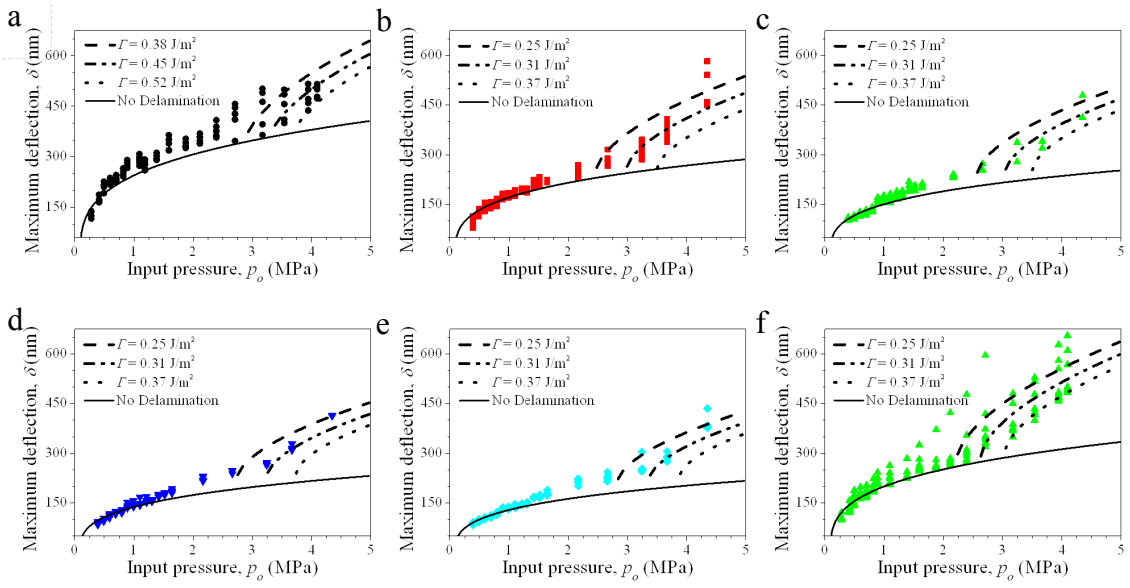

Figure 4-3 (a)– (f) Maximum deflection, δ, vs. input pressure, p_0 for 1-5 layer devices from samples in Figure 4-1a and 4-1b. The solid black line is a theoretical curve assuming no delamination of the membrane. The dashed curves are the calculated theoretical curves for three different adhesion energies using the fitted *nEw* values from Figure 4-8. (a) and (f) are one and three layer samples, respectively, from the flake in Figure 4-1b. (b)-(e) are 2-5 layer devices, respectively, from the flake in Figure 4-1a.

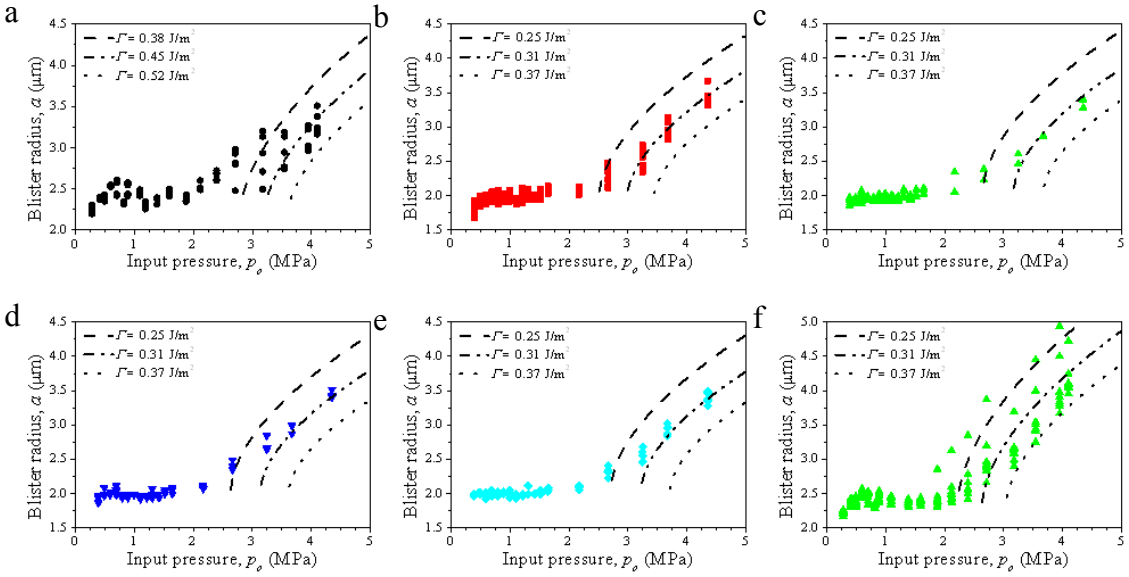

Figure 4-4 (a)– (f) Blister radius, a, vs. input pressure, p_0 for 1-5 layer devices from samples in Figure 4-1a and 4-1b. The dashed curves are the calculated theoretical curves for three different adhesion energies using the fitted *nEw* values from Figure 4-8. (a) and (f) are one and three layer samples, respectively, from the flake in Figure 4-1b. (b)-(e) are 2-5 layer devices, respectively, from the flake in Figure 4-1a.

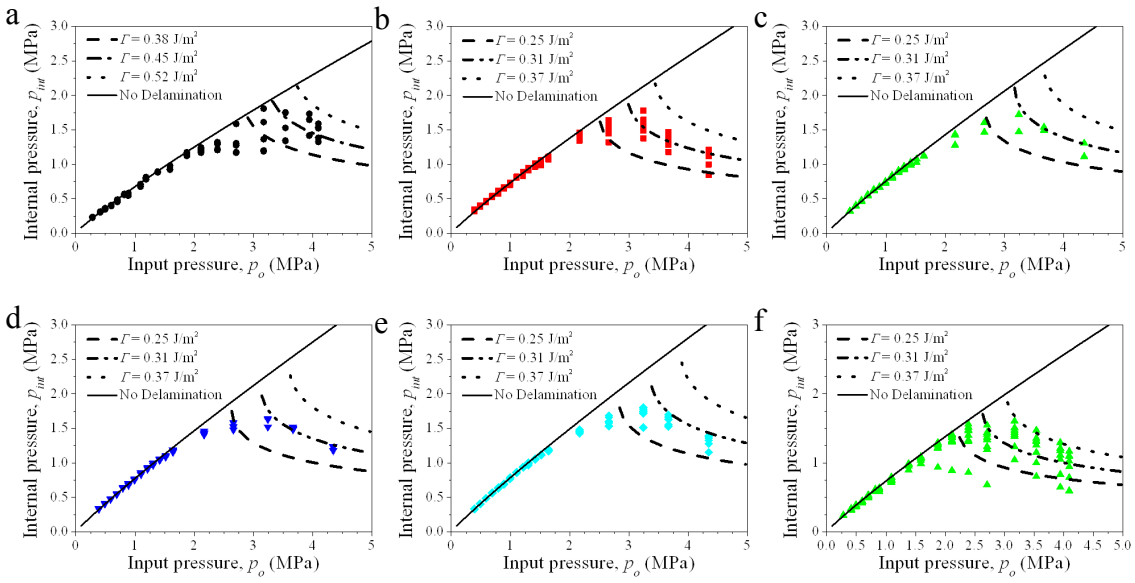

Figure 4-5 (a)– (f) Internal pressure, p_{int}, vs. input pressure, p_0 for 1-5 layer devices from samples in Figure 4-1a and 1b. The solid black line is a theoretical curve assuming no delamination of the membrane. The dashed curves are the calculated theoretical curves for three different adhesion energies using the fitted *nEw* values from Figure 4-8. (a) and (f) are one and three layer samples, respectively, from the flake in Figure 4-1b. (b)-(e) are 2-5 layer devices, respectively, from the flake in Figure 4-1a

show a great degree of axisymmetry in their deformation before and after delamination. Stable delamination is in stark contrast to the common constant pressure blister test, which results in unstable crack growth at the onset of delamination [132]. As a result we call this the 'constant *N* blister test', because the number of molecules in the microcavity is constant during blister delamination. Although a macroscopic counterpart of the constant *N* blister test has been demonstrated [118] (although not widely used), the novelty here is in the use of the adhesive between graphene and SiO_2 to prepare an impermeable seal for gas in the microcavity – filling and emptying of the chamber are accomplished via diffusion through SiO_2, which is slow enough to allow reliable measurements of stable delamination[56].

We use the measured membrane profile (deflection δ and blister radius a versus p_0) in the constant *N* blister test to determine the graphene/SiO_2 adhesion energy. To this end, we describe the deformation of the membrane using Hencky's solution [91], [117] for the geometrically nonlinear response of a clamped isotropic circular elastic membrane subjected to a pressure difference Δp across the membrane equation {3-45} assuming no initial tension. This solution provides the membrane profile in the form of an infinite series in radial position, and also the relationship between the pressure difference and blister height, $\Delta p = K(v)(Ew\delta^3)/a^4$ (equation {3-41}), and the volume of the blister $V_b(a) = C(v)\pi a^2\delta$ (equation {3-42}). The $K(v)\delta^3/a^4$ term primarily describes the geometrical nonlinear deflection pressure response of the circular membrane, as $K(v)$ is a coefficient that is fixed for a specified v. For graphene, we take $v = 0.16$ [147] and so $K(v = 0.16) = 3.09$ and $C(v = 0.16) = 0.524$.

To determine the adhesion energy we model the constant N blister as a thermodynamic system with free energy:

$$F = \frac{(p_{\text{int}} - p_{ext})V_b}{4} + \Gamma\pi\left(a^2 - {a_0}^2\right) - p_0 V_0 \ln\left[\frac{V_0 + V_b}{V_0}\right] + p_{ext}V_b \qquad \{4\text{-}1\}$$

where V_0 is the initial volume of the microcavity, Γ is the graphene/SiO_2 adhesion energy, and a_0 is the initial radius before delamination [118]. In equation {4-1} the four terms represent, respectively, i) stretching of the membrane due to the pressure difference across it, $\Delta p = p_{int} - p_{ext}$ (we calculate this by equating the strain energy in the deformed membrane to the work done by the expanding gas during deformation, which is easier to directly calculate, and then simplifying the result using Hencky's relation for the pressure-deflection and pressure-blister volume); ii) graphene/SiO_2 adhesion iii) expansion of the gas in the chamber from an initial volume V_0 to a final volume $V_0 + V_b$; and iv) work done by the gas held at a fixed external pressure p_{ext}. To deduce $\Delta p = p_{int} - p_{ext}$ across the membrane we used the ideal gas law and assume isothermal expansion of the trapped gas with a constant number of molecules, N. Doing so led to $p_0V_0 = p_{int}(V_0 + V_b)$, where V_0 is the initial volume of the microcavity and V_b is the volume of the pressurized blister after the device is brought to atmospheric pressure and bulges upward. The assumption of constant N is valid considering that the deflection does not change over the ~20 min that the AFM images are acquired, suggesting that no significant change in N, due to gas 'leaking', occurs on the timescale of the experiment.

Minimizing the free energy with respect to a provides a relationship between Γ, δ, and a:

$$\Gamma = \frac{5C}{4}\left(p_0 \frac{V_0}{V_0 + V_b(a)} - p_{ext}\right)\delta \qquad \{4\text{-}2\}$$

We use equation {4-2} to determine Γ with prescribed values of p_0 and p_{ext}, (a, δ) pairs measured

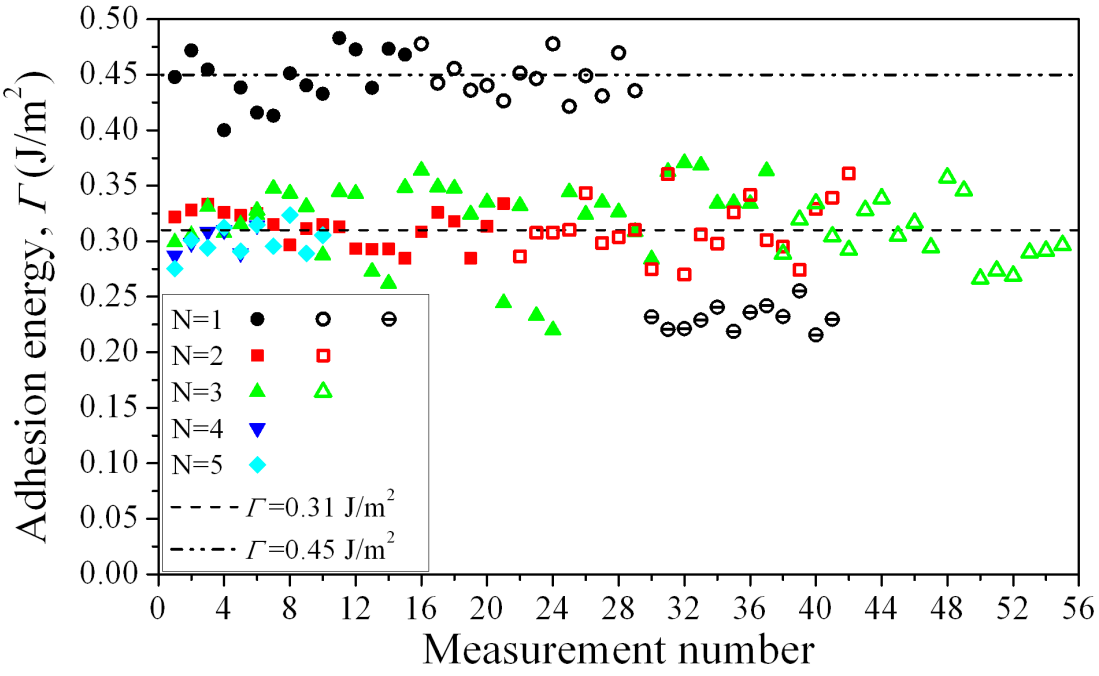

Figure 4-6 Measured adhesion energy for each graphene membrane in this study. Black circles are 1 layer samples, red squares are 2 layer samples, green up triangles are 3 layer devices, blue down triangles are 4 layers, and the cyan diamonds are 5 layer devices. The upper dashed line corresponds to an adhesion energy, Γ = 0.45 J/m^2 while the lower dashed line corresponds to Γ = 0.31 J/m^2.

by AFM, V_0 determined by the microcavity geometry and $V_b(a)$. Values of adhesion energy extracted in this manner are shown for all devices in Figure 4-6. The value $\Gamma = 0.31$ J/m^2 describes the multilayer graphene/SiO_2 adhesion well, but not the monolayer which has a value of 0.45 J/m^2 for two of the samples measured that contained monolayers (samples from Figure 4-1 b and c). A third monolayer sample (sample from Figure 4-1e) was also measured and had a measured adhesion energy of 0.23 J/m^2 , about half of the previously measured adhesion energy for monolayer graphene. The origin of the lower adhesion energy measured in this sample is not entirely understood but could be due to differences in processing of the SiO_2 after lithography and etching.

Our measured adhesion energies are approximately four orders of magnitude larger than adhesion energies commonly found in MEMS where van der Waals forces across non-contacting regions between asperities and capillaries formed in humid environments play a significant role and approximately five times larger than adhesion in gold-coated submicron beams [82], [83], [103], [148], [149]. They are also twice that of previous estimates for multilayer graphene to a SiO_2 substrate[68]; however, those results are extracted from a model that uses an estimate of Young's modulus of graphene that is one-half of that measured here. Our results are comparable to values deduced from experiments on collapsed carbon nanotubes[150]. Using values derived from the measured surface energies of graphite (γ = 165-200 mJ/m^2) and SiO_2 (γ = 115-200 mJ/m^2), one expects an adhesion energy from equation {3-9}, i.e. $\Gamma = 2\ (\gamma_{SiO2} \times \gamma_{graphite})^{1/2}$ = (0.275 - 0.4) J/m^2 [63], [150]. The close agreement between our measured adhesion energy and this estimate suggests that graphene makes close and intimate contact with the SiO_2 substrate [151], [152]. It shows that atomically thin structures like graphene demonstrate conformation over the SiO_2 surface that is more reminiscent of a liquid than a solid.

The reason for the higher adhesion of monolayer graphene to multilayer graphene is not entirely understood. We ruled out bonding due to induced image charges from buried charges in the SiO_2 substrate (see APPENDIX 1) and Sabio, J. *et al*. show that other possible interactions, including electrostatic, are expected to be between one and eight orders of magnitude lower than that measured here [153]. A possible explanation for the discrepancy between one and two to five layers is the increased ability of monolayer graphene to conform to the contours of the surface due to its flexibility. Figure 4-7 shows the roughness measurements of various layers of graphene on the SiO_2 substrate (Images analysed are from the sample in Figure 4-1b taken with the AFM show a decreasing roughness with increasing layer number (about 197 pm for bare SiO_2 (denoted 0 layers in Figure 4-7), 185 pm with one layer, and 127 pm with 15 layers of graphene) suggesting that monolayer graphene conforms more closely to the SiO_2 substrate. Recent theory that idealizes the substrate roughness as a sinusoidal profile shows a jump in adhesion energy with wavelength and amplitude [154], [155], [156] We modified this theory to account for effects of multilayer graphene and it supports the suggestion of a jump to contact that results in increased adhesion energy as the number of layers decreases, however the model is too simple to quantitatively predict that this jump occurs between $n = 2$ and 1 layers [157].

4.4. Mechanical Properties

As mentioned, the deformation of the membrane can be described using Hencky's solution for the geometrically nonlinear response of a clamped circular elastic membrane subjected to a pressure difference Δp across the membrane. The dashed line in Figure 4-1e compares the calculated profile using Hencky's solution [91], [117] with our measured profile. The close agreement validates the use of a and δ to parameterize the deformation. Figure 4-2c shows the equilibrium pint versus p_0 for the bilayer devices. The solid lines in Figure 4-2a and c

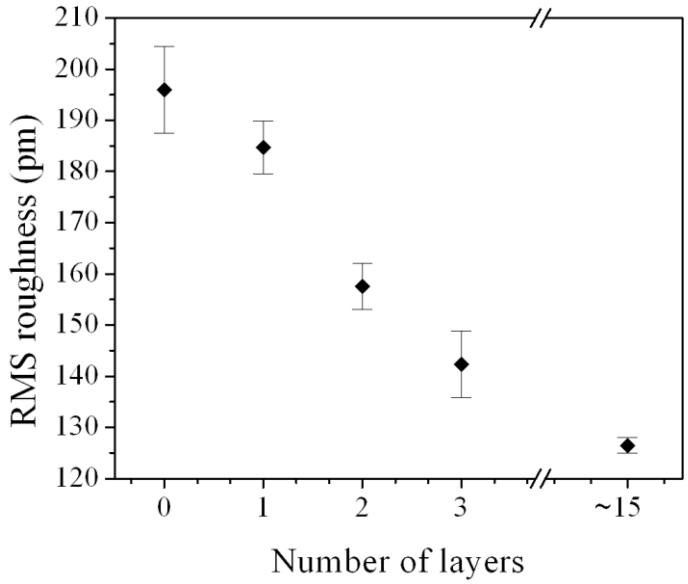

Figure 4-7 RMS roughness measurements taken by non-contact AFM of the substrate (0 layers), 1, 2, and 3 layers as well a thick graphene sample that was ~5 nm (~15 layers) thick as determined by the AFM. Error bars are ±1 standard deviation.

are the solutions of equation {3-41} for a constant $a = a_0$ (no delamination) where we used the fitted value of *Ew*. This provides a good fit until delamination begins ($a > a_0$) at $p_0 = 2.5$ MPa (Figure 4-4). The dashed lines in Figure 4-3, Figure 4-4, and Figure 4-5 are theoretical predictions of δ, a, and p_{int} versus p_0 using the average adhesion energy values from Figure 4-6 and the fitted value of *Ew*.

Figure 4-8a shows $K(\upsilon)\frac{\delta^3}{a^4}$ versus Δp for the monolayer graphene membrane before delamination begins as well as a linear fit to equation {3-41} to determine $Ew = 347$ N/m. This agrees well with previous measurements for graphene and the in plane modulus ($E = 1$ TPa) and interatomic spacing of graphite ($w = 0.335$ nm) [29], [56], [147]. Figure 8b-e shows $K(\upsilon)\frac{\delta^3}{a^4}$ versus Δp for membranes containing two to five graphene sheets. Included are linear fits to the data for $\Delta p > 0.50$ MPa (dashed lines). Theoretical estimates with *nEw* (solid lines) where $Ew = 347$ N/m (our monolayer measurement) and $n = 1$-5 (corresponding to the number of graphene layers) are also plotted, and the *Ew* values obtained by both methods are compared in Figure 4-8f. The good agreement between these values demonstrates that the additional graphene layers are sufficiently well-adhered to the substrate and each other by the van der Waals force so that the pressure is carried by all the layers and no significant sliding or delamination occurs up to pressures as large as 0.50 MPa [158], [159]. For $\Delta p < 0.25$ MPa the effect of initial tension in the membrane cannot be neglected and for $\Delta p > 0.50$ MPa the data show considerably more scatter.

Figure 4-9 shows the results from repeating the elastic constant measurements for pressures up to $\Delta p = 0.50$ MPa for the device in Figure 4-1a. This was done by first pressurizing the sample up to $\Delta p = 0.45$ MPa and then letting the pressure decrease back to $\Delta p = 0$ MPa

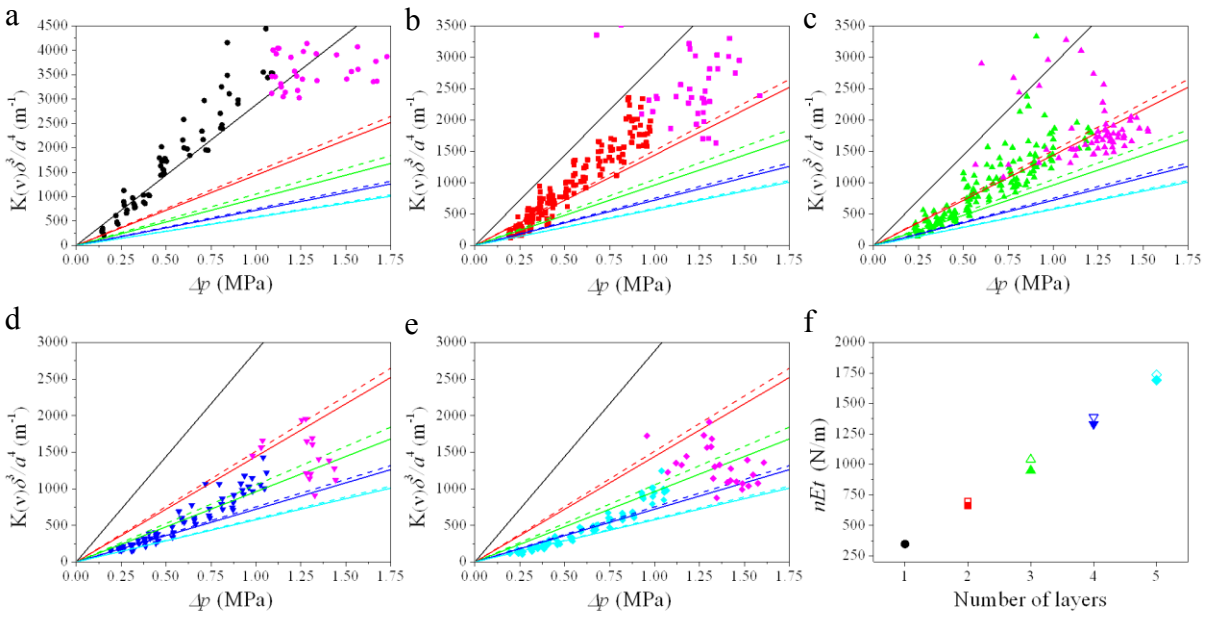

Figure 4-8 (a) $K(\delta^3/a^4)$ vs Δp for the monolayer graphene devices before (black circles) ($a = a_0$) and after (magenta circles) delamination. The black line is a linear fit to all the data has a slope corresponding to Ew= 347 N/m. (b)- (e) $K(\delta^3/a^4)$ vs Δp for 2-5 layer graphene membranes before ($a = a_0$, color shapes) and after ($a > a_0$, magenta shapes) delamination. Red squares are 2 layer samples, green up triangles are 3 layer devices, blue down triangles are 4 layers, and the cyan diamonds are 5 layer devices, the respective magenta shapes denote after delamination. The lines of respective color have slopes corresponding to nEw = 347, 694, 1041, 1388 and 1735 N/m. The dashed lines show linear fits to the data for $\Delta p > 0.75$ MPa and have slopes corresponding to Ew = 661, 950, 1330 and 1690 N/m for 2-5 layers respectively. (f) Plot of the Ew vs. number of layers closed shapes are for the fitted lines and the open shapes are the nEw based on the monolayer fit.

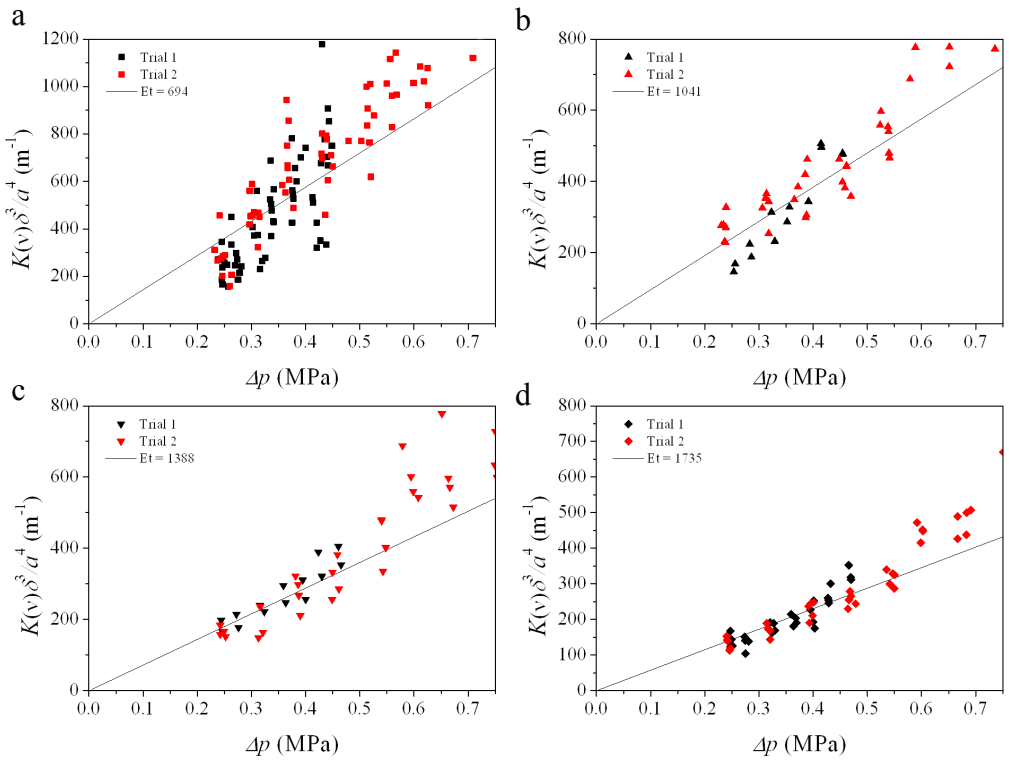

Figure 4-9 (a)- (d) $K(\delta^3/a^4)$ vs Δp for 2-5 layer devices. The black points are from the first pressure cycling of the upper device in Fig. 3.1a. After the highest pressure was measured the pressure was allowed to decrease back to atmospheric pressure and the measurements were repeated and carried higher pressures. This shows that up to $\Delta p \approx 0.5$ MPa there is no altering of the membrane properties between measurements.

before repeating the measurements again. After the membranes were pressurized a second time the pressure was then continually increased until significant delamination was observed. From the repeatability of the elastic constant measurements seen in Figure 4-9 for two to five layers (Figure 4-9a to Figure 4-9d, respectively) we conclude that pressurizing the membranes does not cause sliding or change the membrane properties when $\Delta p < 0.50$ MPa and therefore the membranes can be considered to be well clamped to the substrate in this pressure range. Further work is necessary to understand the origin of the scatter for $\Delta p > 0.50$ MPa, but two possibilities are small amounts of sliding or early stages of delamination, which are difficult to measure by AFM.

4.5. Conclusions

In conclusion, we have demonstrated a simple yet reliable constant N blister test and used it to measure the adhesion energy of the thinnest nanostructures possible, single and multilayer graphene sheets, to SiO_2. This is the first direct measurement of the adhesion energy of one-to-five-layer graphene to SiO_2, a substrate on which the majority of graphene electrical and mechanical devices are fabricated. This result can be used to guide developments in graphene-based electrical and mechanical devices where adhesive forces are known to have an important role, and it should also provide opportunities for fundamental studies of surface forces in the thinnest structures possible [56], [160], [161], [162], [163].

5. Selective Molecular Sieving Through Porous Graphene

5.1. Introduction

The ideal selective membrane should be as thin as possible to maximize flux, mechanically robust to prevent fracture, and have well-defined pore sizes to increase selectivity. Due to its atomic thickness [145], high mechanical strength[29], relative inertness, and impermeability to all standard gases [56], [57], [164], [165], graphene is the ultimate starting point for a size-selective separation membrane[17], [21], [22], [23], [25], [58], [59], [60]. However, this requires the introduction of pores which can exclude larger molecules, while allowing smaller molecules to pass through. To accomplish this, we use UV-induced oxidative etching to introduce pores [166], [167] onto μm-sized graphene membranes and a pressurized blister test and mechanical resonance to measure the transport of a number of gases including H_2, CO_2, Ar, N_2, CH_4, and SF_6 through these pores. The experimentally measured leak rate, separation factors, and Raman spectrum agree well with effusion through a small number of angstrom-sized pores. These porous atomically-thin graphene membranes represent a new class of "ideal" molecular sieves, where gas transport occurs by effusion through angstrom-sized pores with atomic-sized channel lengths.

5.2. Leak Rate though SiO_2

Suspended graphene membranes were fabricated by mechanical exfoliation of graphene over predefined 5 μm diameter wells etched into silicon oxide [37], [110]. After exfoliation, the pristine graphene flakes that span the microcavity form suspended membranes that are impermeable to all standard gas molecules [56] and clamped to the silicon oxide substrate by

surface forces [110]. Gas species can enter and exit the microcavity through the substrate by slow diffusion. To fill the microcavity with a desired gas species, the sample is put in a chamber pressurized to 200 kPa above ambient pressure with a "charging" gas (Figure 5-1a). Prior to this pressurization, the chamber is flushed with the "charging" gas to exclude any other species. The samples are left in the pressure chamber for 4-12 d (depending on the gas species used) to allow for the internal, p_{int}, and external pressure, p_{ext}, of the microcavity to equilibrate to the "charging" pressure, p_0. Upon removing the sample from the pressure chamber the higher pressure inside the microcavity compared with ambient atmospheric pressure causes the membrane to bulge upward (Figure 5-1b). This technique allows preparation of a graphene-sealed microcavity with an arbitrary gas composition at a prescribed pressure.

To measure the leak rate of gas species we used both a pressurized blister test and mechanical resonance test [56]. The pressurized blister test was used for leak rates on the order of minutes to hours while the mechanical resonance was used to measure leak rates on the order of seconds to minutes. For the pressurized blister test, an atomic force microscope (AFM) is used to measure the shape of the bulged graphene membrane, which is parameterized by its maximum deflection, δ (Figure 5-1e). The maximum deflection, δ, vs. time, t, for a pristine graphene membrane pressurized to 200 kPa, above atmospheric pressure, of H_2 gas is shown in Figure 5-1f (black). The deflection decreases slowly with time consistent with a leak of H_2 gas through the underlying silicon oxide [56], [110].

5.3. Porating Graphene

UV-induced oxidative etching was used to introduce pores in the pristine graphene membranes [166], [167], [168], [169] (see appendix). The H_2 gas pressurized graphene membranes were exposed to UV light (λ_1 = 185 nm, λ_2 = 254 nm; Jelight Model 42 UV ozone

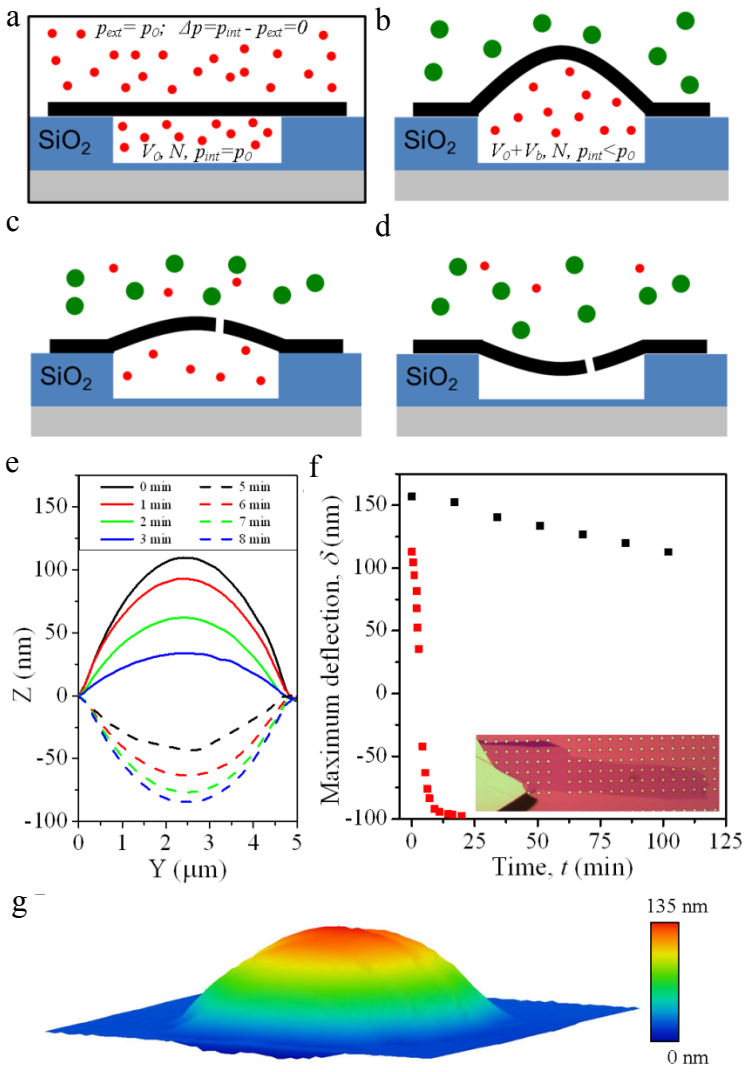

Figure 5-1 (a) Schematic of a microscopic graphene membrane. We start with pristine graphene fabricated by exfoliation and fill the microchamber with 200 kPa of H_2 (red circles) in a pressure chamber. Equilibrium is reached ($p_{int} = p_{ext}$) by diffusion through the silicon oxide. (b) After removing the graphene membrane from the pressure chamber the membrane is bulged upward. (c) Upon etching of the graphene membrane pore(s) bigger than that of H_2 are introduced allowing the H_2 to leak rapidly out of the microchamber through the graphene membrane. If the pore(s) are smaller than that of air molecules (mostly N_2 and O_2, denoted as green circles), air will be blocked from entering the microchamber causing the deflection of the graphene membrane to continue to decrease until all of the H_2 molecules exited the microchamber. (d)After all the H_2 molecules have leaked out of the microchamber the membrane will be bulged downward. (e) Deflection versus position, 0 min (black) through 8 min (dashed blue) after etching, (f) Maximum deflection vs. *t* for one membrane that separates H_2 from air as measured by AFM. H_2 leak rate before (black) and after (red) etching. Inlay: Optical image of the bilayer graphene flake used in this study. (g) Three dimensional rendering of an AFM image corresponding to the line cut at *t* = 0 in (e).

cleaner) at ambient conditions for several minutes. A number of other etching techniques have been proposed and demonstrated on graphene [24], [168], [170], [171], [172], [173], [174], [175] but the UV oxidative etching used here is simple and slow enough to allow for the creation of these sub-nanometer-sized selective pores as demonstrated later in this paper. Other etching techniques, including oxygen plasma etching, were tried but UV oxidative etching proved to be the only successful method for controllably introducing sub-nanometer pores. In order to visualize pores created by the UV induced oxidative etching, one membrane was over-etched to create much larger pores so we could image the pore formation and distribution with AFM. Figure 5-2 shows a monolayer membrane that was over-etched (22 min total with 1 min etching steps) in order to visualize the pore growth. Figure 5-2a shows the 500 nm x 500 nm AFM scan over the suspended region of the over-etched graphene membrane. This membrane was not selective to any of the gas species tested and the leak rates were too fast to measure. The results of the pore size distribution seen in Figure 5-2b and Figure 5-2c are comparable to previous oxidative etching of graphene and graphite

In order to etch the graphene membranes, we first pressurized them with pure H_2 up to 200 kPa (gauge pressure) above ambient pressure. After the microcavity reached equilibrium we removed it from the pressure chamber and measured the deflection using atomic force microscopy (AFM). We then did a series of short UV etches (30 s) followed by AFM scans between each etching step to see if the leak rate increased significantly. When pore(s) were created that were selective to allow the H_2 to pass through, but not allow the molecules in the air to pass, the deflection would rapidly decrease and become negative, consistent with a vacuum inside the microcavity. For the case of the “Bi- 3.4 Å” membrane in this chapter, this etching took 75 min (150, 30s etching steps). Each etch step took about 5 min to complete. Once the

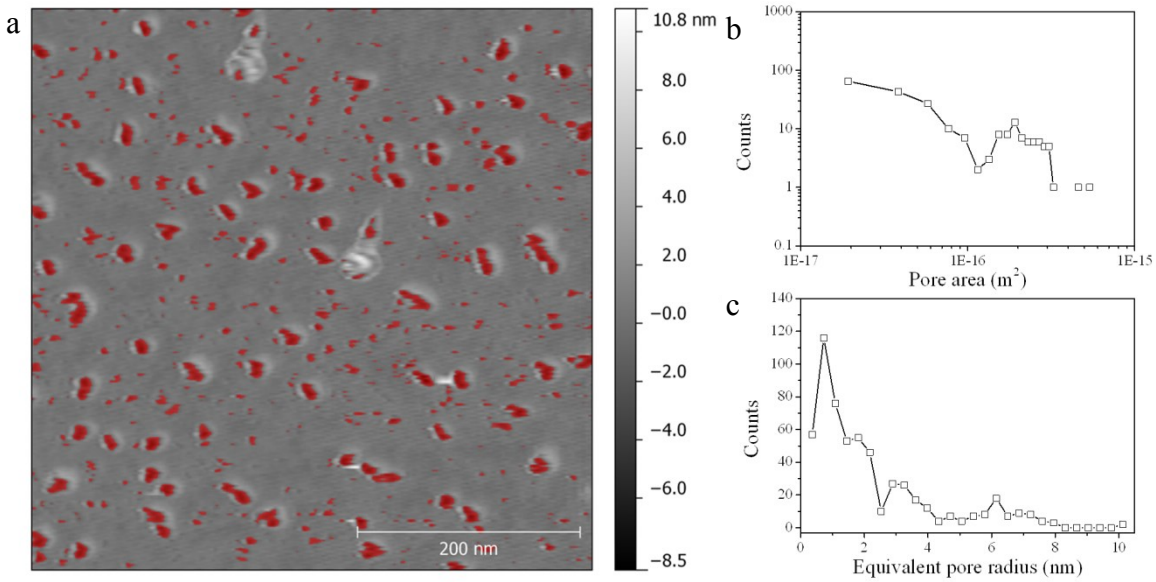

Figure 5-2 (a) AFM scan of a membrane etched for a longer time to visualize the pore growth. The red areas are pits created by the UV etching. (b) Histogram of the number of pores versus the approximate pore area. (c) Histogram of the number of pores versus the equivalent radius of the pore. (b) and (c) indicate a nucleation and growth mechanism for pore evolution.

sample was out of the pressure chamber for over an hour during the etching process, and the deflection had decreased 20 nm, we then returned the sample to the pressure chamber overnight to allow the pressure inside the microchamber to once again reach 200 kPa. The etching process was then continued the next day. For membrane "Bi- 4.9 Å" in the main text, the total etching time was 15 min using 1 min etching steps. From the etching experiments it was noted that longer etch steps required significantly less total etching time

After each oxidative etch step, δ is again measured versus t (Figure 5-1e and Figure 5-1f, red). The maximum deflection decreases rapidly (several minutes as opposed to hours for the unetched case) and eventually leads to a downward deflection of the membrane (Figure 5-1c-f). Figure 5-1e shows a series of cross sections through the center of the membrane taken by AFM as time elapses from 0 to 8 min and Figure 5-1g shows a three dimensional rendering of the AFM image for t=0 in Figure 5-1e. Here 0 min is defined to be the time at which the first AFM image was captured after removing the sample from the pressure chamber. The change in deflection, as depicted in Figure 5-1c & d, results from increasing the H_2 leak rate, through etching, while preventing significant changes in the N_2 leak rate into the microcavity from the ambient atmosphere.

5.4. Molecular Sieving

The molecular selectivity of the fabricated porous graphene membrane is demonstrated by measuring the time rate of change of δ, $-d\delta/dt$, for the same membrane pressurized with a number of different gases. Figure 5-3a shows δ vs. t for H_2, CO_2, Ar, and CH_4 before and after

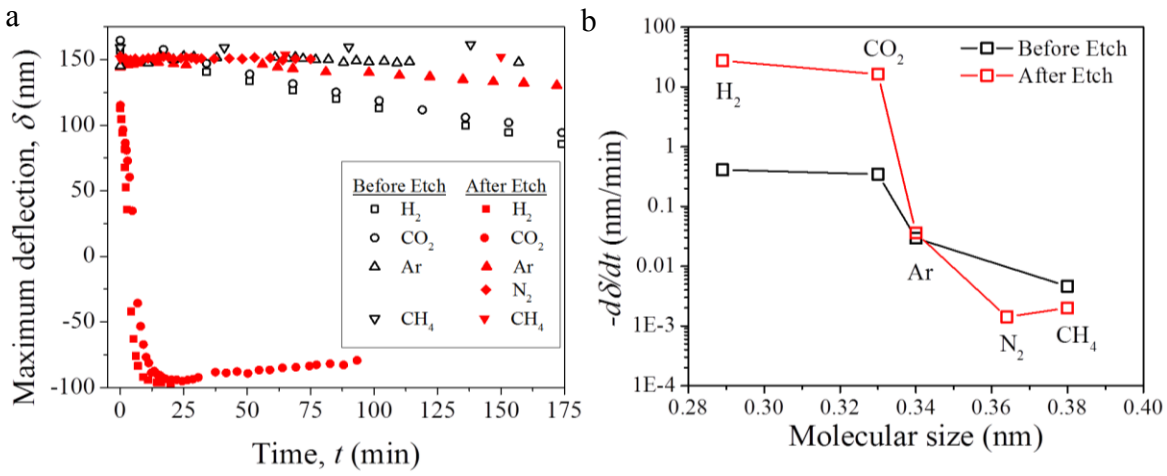

Figure 5-3 (a) Maximum deflection, δ, versus t before (black) and after etching (red). (b) Average -$d\delta/dt$ versus molecular size found from the slopes of membrane deflection versus t in (a) for before (black) and after (red) introducing pores in the same graphene membrane. The connecting lines show the measurements before (black) and after (red) etching.

etching and N_2 after etching[12]. At short times, $-d\delta/dt$ is approximately linear (Figure 5-3a). This rate, $-d\delta/dt$, versus kinetic diameter [176] is plotted for all the gases measured for the same membrane/microcavity in Figure 5-1 before and after etching (Figure 5-3b). After etching, there is an increase in $-d\delta/dt$ of two orders of magnitude for the leak rate of H_2 and CO_2, while Ar and CH_4 remain relatively unchanged. This suggests that the etched pores change the transport mechanism for H_2 and CO_2, while leaving the transport of Ar and CH_4 nearly unchanged. Since the kinetic diameter cut off in this bi-layer graphene membrane is nominally that of Ar, 3.4 Å[176], this membrane will heretofore be referred to as "Bi- 3.4 Å".

The leak rate of various gases across the porous graphene membranes can also be measured by using a mechanical resonance test. This is accomplished by measuring changes in the mechanical resonant frequency, *f*, of the membrane vs. *t* using an optical drive and detection system previously used to measure mechanical resonance in suspended graphene resonators (schematic in Figure 5-4a) [56], [109]. A pressure difference applied across the membrane leads to a pressure-induced tensioning of the membrane, which increases *f* of the stretched membrane. If the gas molecules introduced external to an initially evacuated microcavity can leak through the membrane, the gas will pass through and reduce the tension in the membrane, thus decreasing *f*. If the gas molecules cannot leak through the membrane, *f* stays constant. An example of this is shown in Figure 5-4a where an etched porous graphene membrane was put in a vacuum of 0.1 torr for a several days to ensure the microcavity has equilibrated to the pressure of the vacuum chamber. Next, a pure gas species is introduced into the vacuum chamber at a given pressure (~100 torr for the case in Figure 5-4b and ~80 torr for the inlay of Figure 5-4b) and the resonant frequency is measured. The resonant frequency decreases with time, and from

[12] We did not measure the N_2 leak rate for this particular device before etching, but measurements for 12 other ones located on the same flake are shown in Figure 5-5 and labelled "Pristine Avg" for comparison with the after-etch leak rate.

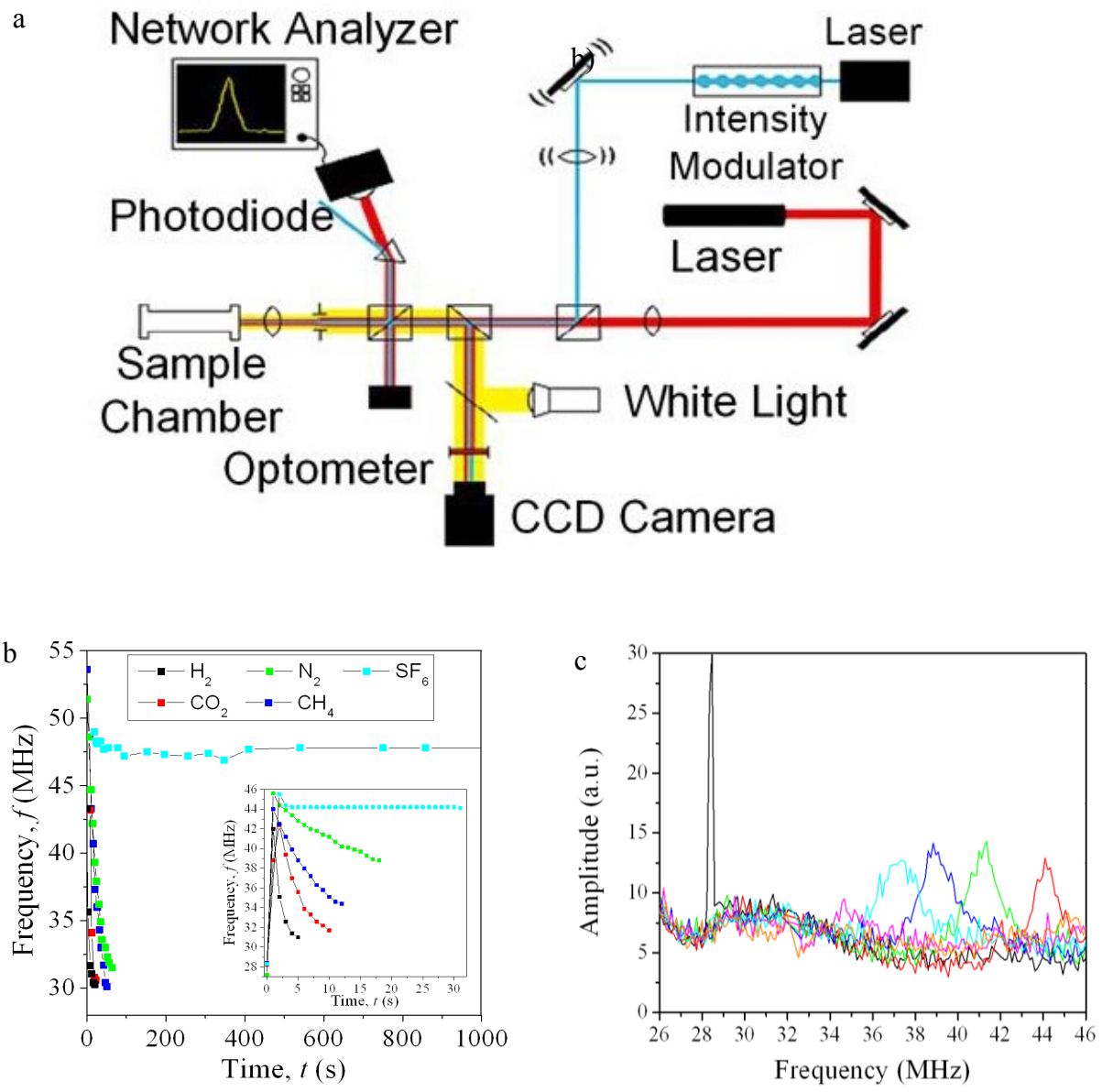

Figure 5-4 (a) schematic of optical drive and detection for measuring frequency of graphene drum resonators. (b) Frequency, *f*, vs *t* for H_2 (black), CO_2 (red), N_2 (green), CH_4 (blue), and SF_6 (cyan). With a pressure of 100 torr (~13.3 kPa) introduced into the vacuum chamber. Inlay is data from the same device with an 80 torr (~10.7 kPa) pressure introduced. (c) Amplitude vs drive frequency for 80 torr of CH4. The data corresponds to the frequencies shown in the inlay of (b) taken at *t* = 0 s (black), *t* = 1 s (red), *t* = 3 s (green), *t* = 5 s (blue), *t* = 7 s (cyan), *t* = 11 s (magenta), and *t* = 13 s (orange). Clearly the quality factor is too low after 13 s to reliably find the frequency.

the rate of decrease, we determine the leak rate through porous graphene membrane. We could not observe the frequency return back to its original value due to significant gas damping when $\Delta p \sim 0$ (see Figure 5-4b). As can be seen from Figure 5-4a, the leak rate of H_2, CO_2, N_2, and CH_4 is several seconds while SF_6 shows no significant change in resonant frequency for the several minutes measured. This membrane will be referred to as "Bi- 4.9 Å" since it is a bilayer membrane with a nominal sieving kinetic diameter of SF_6, 4.9 Å [176].

We derive the following expression for the molecular flux out of the pressurized "blister" microcavity, *dn/dt*, using the ideal gas law and Hencky's solution (equation {3-45}) for a clamped circular membrane assuming no initial tension in the membrane(i.e. S_0 =0). The ideal gas law is given by

$$PV(\delta) = nRT \qquad \{5\text{-}1\}$$

where P is the absolute pressure inside the microcavity, $V(\delta)$ is the volume of the microcavity when the membrane is bulged with deflection δ, $V(\delta)=V_o+V_b(\delta)$, $V_b(\delta)=C(\nu)\pi a^2\delta$, for graphene $C(\nu = 0.16) = 0.52$, n is the number of moles of gas molecules contained in the microcavity, R is the gas constant, and T is temperature [110]. Substituting $(\Delta p+p_{atm})$ for P and dividing both sides by $V(\delta)$ into equation{5-1}, and inserting for equation {3-45} Δp with S_0 =0 we get:

$$\left(K(\nu)\left(Ew\delta^2\right)/a^4 + p_{atm}\right) = \frac{nRT}{V_0 + V_b(\delta)} \qquad \{5\text{-}2\}$$

Now we can take the time derivative of both sides and solve for *dn/dt* to get the flux of gas molecules out of the membrane

$$\frac{dn}{dt} = \frac{\left[3K(\nu)\left(Ew\delta^2\right)/a^4 \bullet \qquad \left(C(\nu)\pi a^2\right)\right]}{RT} \bullet \qquad \{5\text{-}3\}$$

where a is the radius of the membrane, E is the Young's modulus, w is the thickness of the membrane, R is the molar gas constant, T is temperature, $V(\delta)$ is the total volume of the microcavity in the bulged state, and $C(\nu)$ and $K(\nu)$ are geometric coefficients which depend on the Poisson's ratio, ν, of the membrane. For the case of graphene, the Young's modulus and Poisson's ratio are E = 1 TPa and ν = 0.16, respectively, and the thickness per layer is 0.34 nm [29], [56], [110], [147]. Using ν = 0.16 gives coefficients of $K(\nu{=}0.16)$ = 3.09 and $C(\nu{=}0.16)$ = 0.524. Figure 5-5 shows the normalized dn/dt (normalized to the partial pressure difference across the membrane) for the "Bi- 3.4 Å" membrane before UV etching (black squares) and after UV etching (red squares). Also included is the average normalized dn/dt for 24 different unetched (12 for the case of N_2) membranes on the same graphene flake shown in the Figure 5-1f inlay that contains "Bi- 3.4 Å" (black circles).

Similarly, dn/dt, can be calculated from the linear approximation of the rate of frequency decay, df/dt. We do this by first combining equations {3-45} and {3-51}. We do not take S_0 to be zero in this case since the pressure difference and thus the deflection of the membrane are small compared with the case of the blister test.

$$S^3 - 4S^2 + 5SS_0^2 - 2S_0^3 = K(\nu)\left(Ewa^2\Delta p^2\right)/64 \qquad \{5\text{-}4\}$$

Since S is larger than S_0 we can neglect the cubic order term of S_0. Now we can insert the expression for S into equation {3-50} and solve for Δp, and then insert this expression for Δp into the ideal gas law in a similar fashion as the bulge test equation. Since the deflection of the membrane is small in this case we take V to be constant. After doing this and taking time

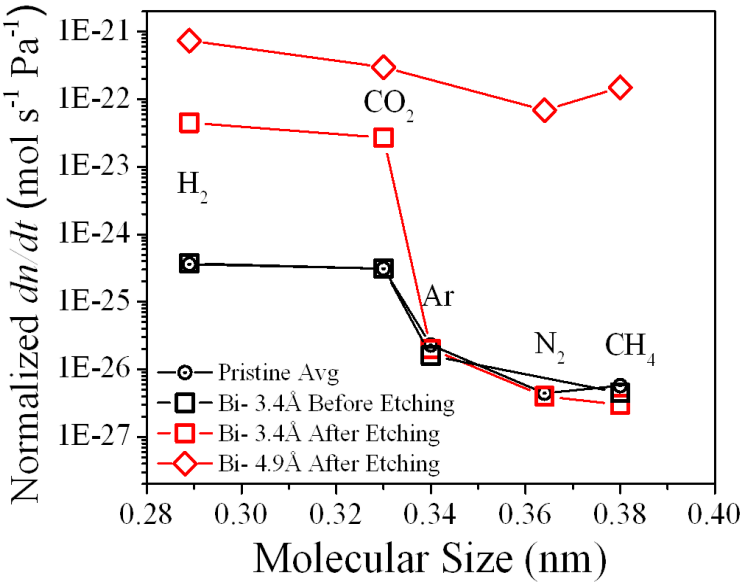

Figure 5-5 Leak rate out of the microcavity for: "Bi- 3.4 Å" membrane before etching (black squares) and after etching (red squares), "Bi- 4.9 Å" membrane after etching (red diamonds), and the average before etching of 24 membranes (12 for N_2) on the same graphene flake as "Bi- 3.4 Å" membrane (black circles with dot). (Note: the latter are hidden by black squares for several gases.)

derivative and solving for *dn*/*dt* we arrive at the expression:

$$\frac{dn}{dt}=\frac{V}{RT}\left[\frac{\frac{1}{2}\left(\frac{\left(c_1\rho_A-2c_2{\rho_A}^2a^2f^2\right){S_0}^2+c_3{\rho_A}^3a^4f^4}{4KEw}\right)^{1/2}+\frac{c_3{\rho_A}^3a^4f^4-c_2S_0{\rho_A}^2a^2f^2}{\left(KEw\left(\left(c_1\rho_A-2c_2{\rho_A}^2a^2f^2\right){S_0}^2+c_3{\rho_A}^3a^4f^4\right)\right)^{1/2}}}\right]\frac{df}{dt} \qquad \{5\text{-}5\}$$

where c_1 = 8744, c_2 = 47785/2, and c_3 = 81589. To get *dn*/*dt* (*mol*/*s*) we can use *df*/*dt*, the rate of the frequency decay from the linear fit of the membrane frequency versus time data. We then normalize the leak rate by dividing the calculated *dn/dt* by the pressure driving force for each of the gases measured to get the leak rate (normalized *dn/dt*) into the graphene-sealed microcavity. The leak rate versus molecular size for the "Bi- 4.9 Å" membrane is shown in Figure 5-5a (red diamonds).

The changes in leak rates associated with UV etching are consistent with the introduction of a pore(s) which allow size selective permeation of gas molecules. For the "Bi- 3.4 Å" membrane in Figure 5-3, the selectivity between CO_2 and Ar suggests that the pore(s) size(s) introduced into the graphene membrane are comparable to the kinetic diameter of Ar (3.4 Å) [176] and that the porous graphene is sieving molecules above and below this size. Similarly for the "Bi- 4.9 Å" membrane in Figure 4-3, there are likely pore(s) larger in size than that of the "Bi- 3.4 Å" membrane, since effective molecular sieving is seen for molecules smaller than SF_6 (4.9 Å compared to 3.8 Å for CH_4)[176]. Due to the fact that there is likely only a small density of pores in the 5 μm diameter membranes, imaging of the pore is not possible (see supporting online text). However, the small density of pores is supported by Raman spectroscopy on the etched membranes.

The gas leak rates measured can be compared to results of computational modelling by Jiang, et al. and Blankenburg et al. [17], [58]. In the work of Jiang et al, the authors calculate a H_2 leak rate on the order of $\sim 10^{-20}$ mol s^{-1} Pa^{-1} for a H-passivated pore in graphene consisting of 2 missing benzene rings at room temperature (see appendix)[17]. For the work of Blankenburg et al., the H_2 leak rate was calculated to be on the order of $\sim 10^{-23}$ mol s^{-1} Pa^{-1} through a smaller H-terminated pore consisting of a single missing benzene ring [58].

Our measured H_2 leak rate on "Bi- 3.4 Å" was ~4.5 x 10^{-23} mol s^{-1} Pa^{-1}. This value is several orders of magnitude lower than Jiang et al, suggesting our pores have an overall higher energy barrier for H_2 (and other species) than in their calculations. The similarity between our H_2 leak rate with that modelled by Blankenburg et al suggests a similar H_2 energy barrier in our pore. Nonetheless, we do not match their calculated H_2/CO_2 selectivity (2 versus $\sim 10^{17}$). This suggests that having a bilayer graphene membrane with different chemical pore termination from the oxidative etching can be quite important.

We can also compare the H_2 and CO_2 measured leak rates between the "Bi- 3.4 Å" and "Bi- 4.9 Å" membranes (Figure 5-5). The one with the smaller pore size, "Bi- 3.4 Å", (red squares) had a H_2 and CO_2 leak rates (in units of 10^{-23} mol s^{-1} Pa^{-1}) of 4.5 and 2.7, respectively, compared to H_2 and CO_2 leak rates (same units) of 75 and 25, respectively, for the larger pore membrane (red diamonds). The closeness between the magnitude of these 2 values, and the magnitudes calculated in the cited modelling, suggests that in both cases a low density of size-selective pores are participating in the transport across the graphene membrane and the faster leak rate for the "Bi- 4.9 Å" membrane is consistent with larger pores (and/or lower diffusional energy barriers) than the "Bi- 3.4 Å". This is also consistent with the rapid effusion of gas

expected from the ~μm^3 confined volume of gas in the porous graphene sealed microchamber [56].

Both graphene membranes presented here were bilayer graphene membranes due to the more controlled etching and stability of the pores fabricated on bilayer versus monolayer graphene membranes. This is consistent with previous results showing slower etching for bilayer graphene compared with single layer graphene[168]. However, similar results were observed on two additional monolayer graphene membranes. The first monolayer sample in Figure 5-6 ("Mono- 3.4 Å") shows similar behavior as seen in "Bi- 3.4 Å" of the main text. This monolayer sample was filled with 150 kPa above ambient pressure with pure H_2. The pore was not stable and additional measurements could not be taken. The second monolayer sample shown in Figure 5-7 was measured using the mechanical resonance scheme presented in the main text. This membrane showed a similar pore instability as the previous sample. The order of the leak rate measurements taken on this membrane were N_2 (black), H_2 (red), CO_2 (green), and CH_4 (blue). Next, N_2 was measured a second time (cyan) showing a drastic increase in the N_2 leak rate. After the repeat of the N_2 data, we then introduced SF_6, and the results show that the membrane is slowly allowing SF_6 to permeate indicating that this pore is larger but similar in size to SF_6 (4.9Å) [176]. We attribute this increase in N_2 leak rate to etching of the pore during the resonance measurement.

Two additional bilayer membranes from the same graphene flake found in Figure 5-1(containing membrane "Bi- 3.4 Å") of the main text are shown in Figure 5-8. Figure 5-8a is a membrane that has larger pores than that of the sample presented in the main text. The membrane in Figure 5-8a was damaged before CH_4 leak rate data could be taken. Figure 5-8b is

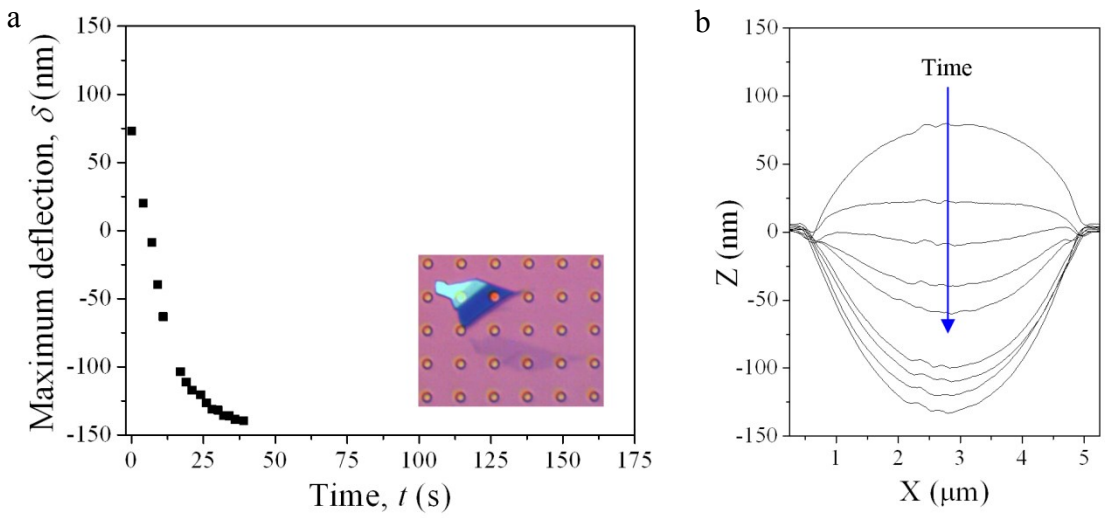

Figure 5-6(a) Maximum deflection, δ, vs, t for a monolayer membrane. The rapid decrease in deflection that becomes negative is consistent with the results seen in Fig 1 of the main text. Inlay: optical image of the monolayer graphene membrane covering one well in the substrate. (b) AFM line scans of the membrane in (a) as time passes.

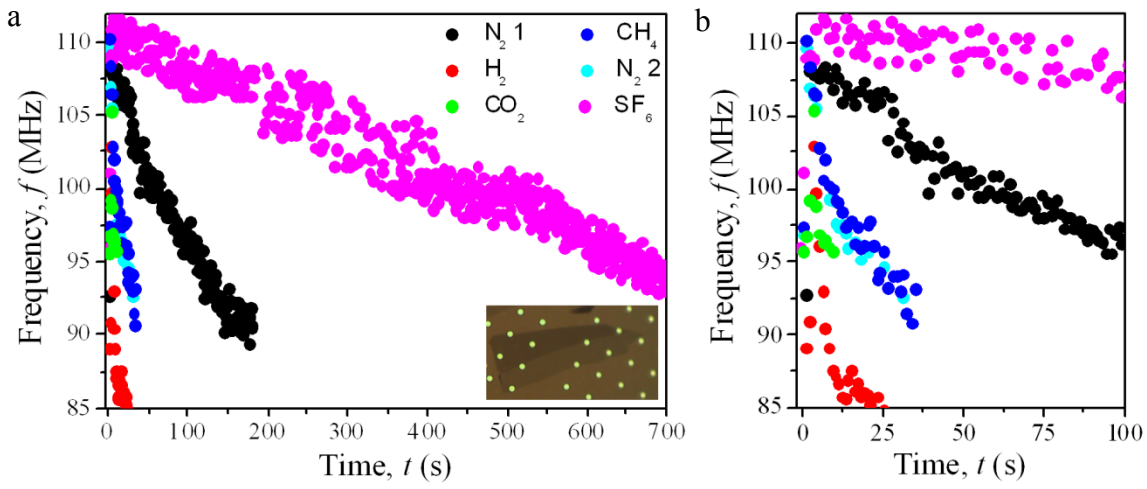

Figure 5-7(a) Frequency vs time for N_2, H_2, CO_2, N_2, CH_4, and SF_6, taken in that order. (b) A zoom in of (a). The change in N_2 leak rate indicates that the pore(s) in monolayer graphene are not stable and the pore size can change. After the pore was enlarged, the membrane was able to allow SF_6 to leak through the membrane.

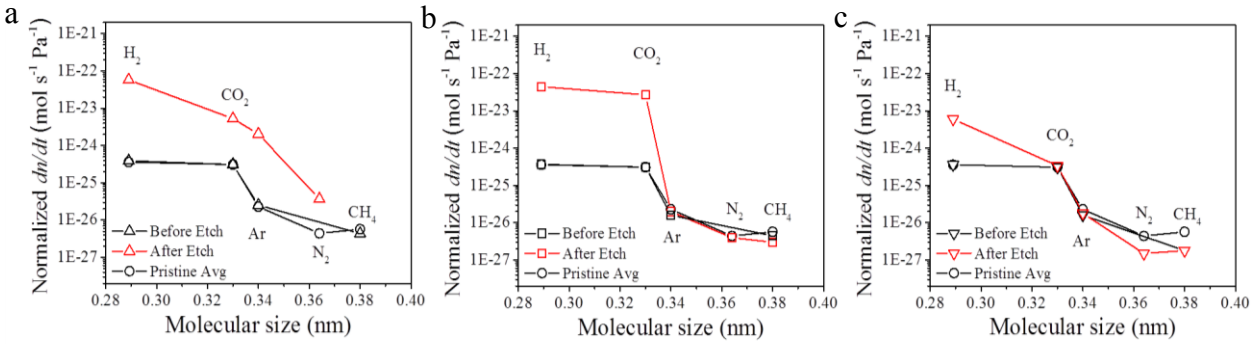

Figure 5-8 (a) Normalized *dn/dt* vs. Molecular size showing permeation of all gas species larger than CH_4 before and after etching. This membrane was damaged before the CH_4 data could be taken. (b) Normalized *dn/dt* vs. Molecular size for the membrane "Bi-3.4 Å" before and after etching. (c) Normalized *dn/dt* vs. Molecular size for a membrane showing an increase in the leak rate of H_2, and no significant increase in the leak rate for CO_2, Ar, N_2, and CH_4. (a), (b), and (c) where all from the same graphene flake that can be found in the inlay of Fig 1f from chapter 4.

the sample presented in Figure 5-5 ("Bi-3.4Å") but is included here for comparison, and Figure 5-8c shows the leak rate of a membrane that showed molecular sieving of H_2 versus CO_2 and larger molecules (Ar, N_2, and CH_4). This suggests that the pore size for the membrane in Figure 5-8c is between 2.89 Å and 3.3 Å [176].

5.5. Conclusions

In conclusion, we have demonstrated selective molecular sieving using porous, μm-sized, atomically-thin graphene membranes. Pores were introduced in graphene by UV-induced oxidative etching and the molecular transport through them was measured using both a pressurized blister test and mechanical resonance. Our results are consistent with theoretical models in the literature based on effusion through angstrom-sized pores [17], [58]. The results presented here are an experimental realization of graphene gas separation membranes by molecular sieving and represent an important step towards the realization of macroscopic, size-selective porous graphene membranes. The approach used here can also be used to probe the fundamental limits of gas transport by effusion through angstrom-sized pores with atomic-sized channel lengths.

6. Towards Large Scale Graphene Membranes for Gas Separations

6.1. Introduction

In Chapter 5 we demonstrated proof of concept results on the ability for graphene to act as a molecular sieving gas separation membrane. However, this was on a small scale (~5 um diameter membranes) and much work needs to be done to make graphene gas separation membranes a viable technology for industrial applications. This chapter focuses on strategies to scale up the micron sized porous graphene to the mm size scale. The goal of this chapter is to take the next step in realizing industrial scale porous graphene membranes for gas separations. This will be accomplished by using graphene films grown by CVD on copper or nickel foils [41]. Once the graphene films are grown via CVD on copper foils graphene films will then be transferred to porous ultrafiltration support membranes [39], [42], [43], [44], [177]. This will result in an asymmetric membrane were selectivity of gases will be accomplished by molecular sieving through the porous graphene layer.

The first step in realizing CVD graphene gas separation membranes will be to produce impermeable graphene films grown by CVD. Since CVD graphene films are polycrystalline defects in the crystal boundaries could potentially be detrimental to the selectivity of such a membrane [17], [177]. In addition CVD graphene films are subject to voids in the film during growth were the individual grains did not connect in the growth process [178], [179]. In order to make highly selective membranes a method of creating continuous impermeable films has been explored. The primary method for producing impermeable graphene membranes will be to stack multiple single layers graphene films together on the porous support [180]. The advantage to this technique that the defect free zones of individual layers will stack on the defective grain

boundaries of the adjacent layers. Our initial results on micron-sized graphene flakes show that etching of bilayer flakes is more controllable and leads to more stable pores suitable for gas separations.

Once impermeable graphene films are created, etching will then be done to open up size selective pores to separate gases. Etching to open up pores in the graphene films will initially be done using UV-induced oxidative etching similar to what was reported in Chapter 5. Permeation of the mm-scale graphene membranes will be measured using a time lag permeation apparatus that was recently built in our lab. A schematic of the time lag permeation apparatus can be seen in Figure 6-1a and b picture of the set up can be seen in Figure 6-1b. The next section will focus on time lag permeation measurements and the measurement apparatus built in our lab.

6.2. Measurement of Large Scale Graphene Membranes

The experimental set up of the time lag permeation measurements can be seen in Figure 6-1 (a and b). The set up consist of a membrane cell with pressure sensors on each side of the membrane to monitor the upstream and downstream pressures as a function of time. The membrane accepts circular membranes with a diameter of 8 mm. The upstream side is connected to a gas source with pure component gasses being used. Typically H_2, CO_2, O_2, N_2, and CH_4 are used due to their well-known kinetic diameters of 2.8 Å, 3.3 Å, 3.46 Å, 3.64 Å and 3.8 Å respectively. The downstream side is connected to a vacuum pump to evacuate the downstream side to a negligible level prior to experimentation. Figure 6-1c shows a typical downstream pressure versus time measurement for a dense membrane. Once steady state is reached, i.e. the pressure verse time relation becomes linear, a line with the same slope as the linear region can be

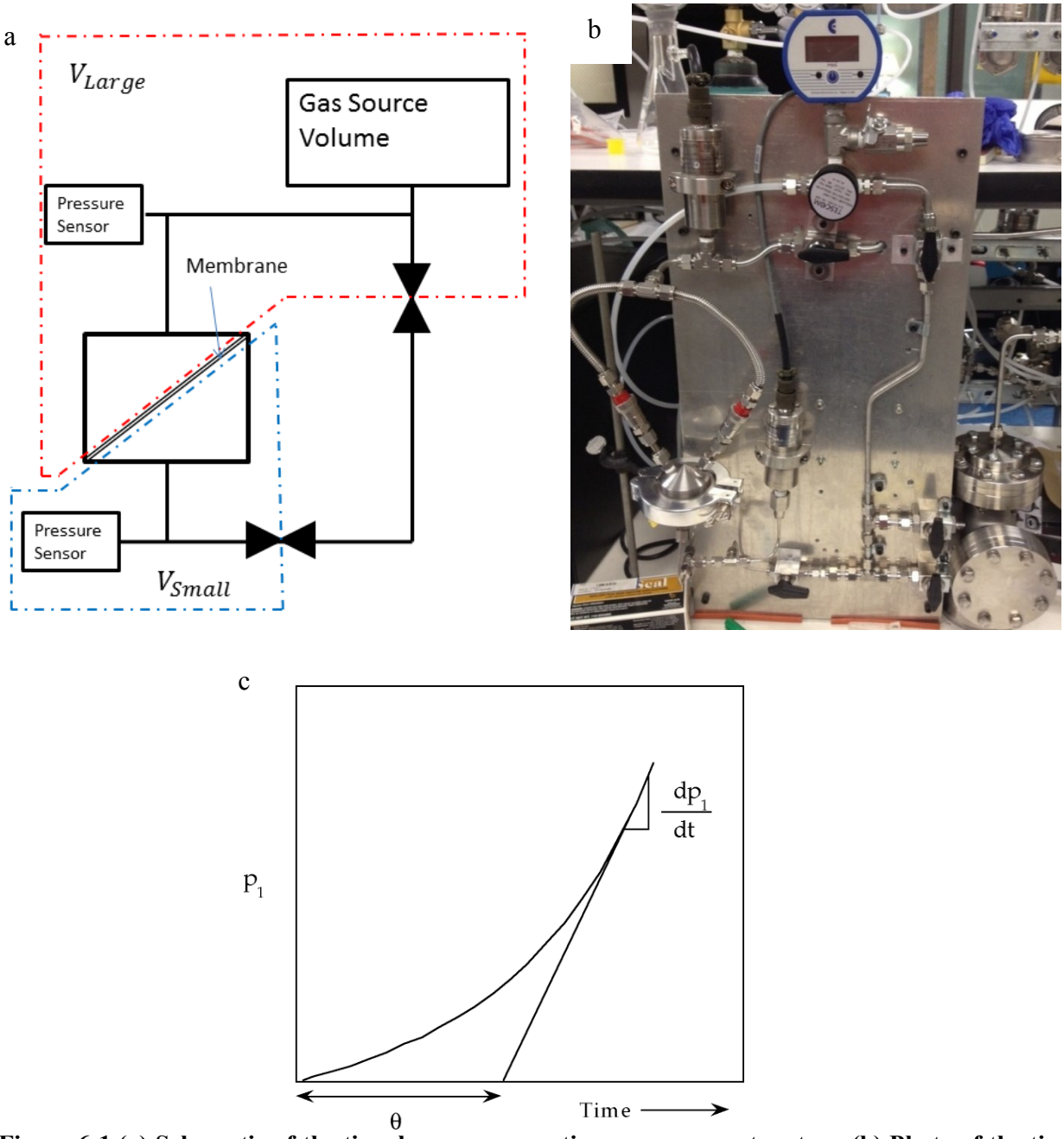

Figure 6-1 (a) Schematic of the time lag gas permeation measurement system. (b) Photo of the time lag permeation measurement system used in this study. (c) Schematic of a typical downstream pressure response for a dense membrane undergoing solution diffusion.

traced down to the x-axis to find the time lag. This time lag is how long it took the membrane to saturate. The slope of the line dp/dt is the steady state rate of pressure rise and can be used to compute the permeability rate P with the following equation [181]:

$$P = \left(\frac{dp}{dt}\right)\frac{VT_0L}{A\Delta pTP_0} \qquad \{6\text{-}1\}$$

where P is the permeability coefficeient also the permeability rate, dp/dt is the steady state rate of pressure rise on the downstream side of the membrane, V is the calibrated downstream volume (see APPENDIX 2), Δp is the pressure difference across the membrane, A is the area of the membrane, L is the thickness of the membrane, T is the measurement temperature, and T_0 and P_0 are the standard temperature and pressure, respectively. After finding the permeability rate of each component the ideal separation factor (α_{AB}) can be calculated. The ideal separation factor is defined the ratio of permeation rate of component A over B

$$\alpha_{AB} = \frac{P_A}{P_B} \qquad \{6\text{-}2\}$$

where P_A is the permeation rate of component A and P_B is the permeation rate of component B.

6.3. Large Scale Graphene Membrane Fabrication

To date two techniques have been explored to fabricate large scale graphene gas separation membranes using CVD graphene grown on copper foils. For both techniques graphene is grown on 25 μm thick copper foils[13] in a tube furnace with Ar, CH_4 and H_2 flow at 1000˚C at ambient pressure[14] [39]. After growth the graphene is transferred to a polymer support.

[13] Copper foils are from Alfa Aesar and are ordered with no chromium oxide passivation layer.
[14] Flow rates for the gases are 5sccm CH_4, 6sccm H_2, 200 sccm Ar. Growth time was 10 min. H_2 and Ar were flowing during the heating process.

I will refer to these techniques as the polymer carrier transfer technique and the press transfer technique [43], [44], [177]. The polymer supports used here are either porous Polysulfone (PSf) ultrafiltration membranes with a nominal molecular cut off of 70mg/mol supplied from GE infrastructure. We used Ammonium persulfate [$(NH_4)_2S_2O_8$] as the oxidative etching solution at a concentration of 1 M to etch away the copper foils. When the graphene is grown on the copper foils both sides are initially coated with graphene(Figure 6-2a). For the following transfer techniques one side of the graphene needs to be removed. We do this by etching one side of the graphene by floating it in the etching solution for a short time (Figure 6-2b) and then removing it from the solution and rinsing it with deionized (DI) water to rinse the graphene off of that side (Figure 6-2c).

6.3.1. Polymer Carrier Transfers

This technique consists of first casting a polymer layer over the graphene layer grown on copper (Figure 6-2d). This is typically accomplished by spin casting to get a thin polymer layer, and Poly(methyl methacrylate) (PMMA) is the polymer typically used for such transfers[180]. We used PMMA with a molecular weight of 966k dissolved in Anisole at 80 mg/ml. Once the polymer is cast on top of the graphene, the copper foil is then placed in an oxidation bath to etch away the copper foil leaving behind a layered composite of PMMA on top of graphene (Figure 6-2e). Next, the graphene/PMMA is gently transferred to a bath of DI water to wash away the Ammonium persulfate and other residuals from the etching process (Figure 6-2f). Once the graphene/PMMA is in the DI water the substrate it is to be transferred to is submerged in the DI water and placed directly under the graphene/PMMA stack. Finally the DI water is slowly drained out of the container and the graphene/PMMA is lowered onto the substrate and the substrate/graphene/PMMA stack is left to dry overnight (Figure 6-2g) [42].

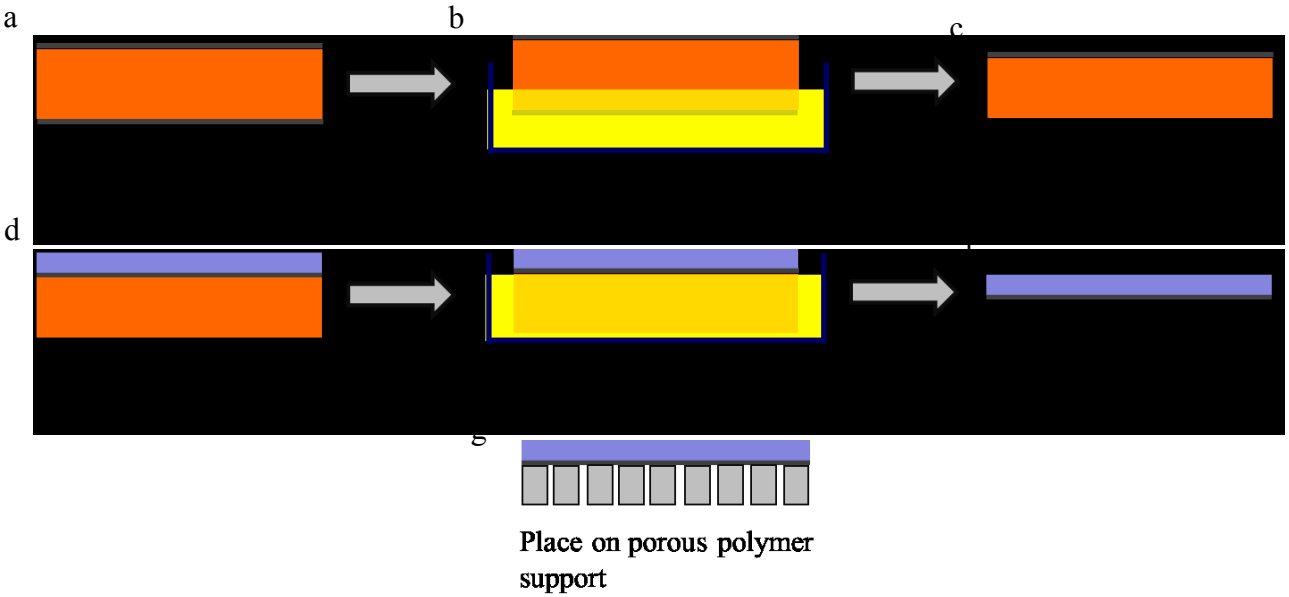

Figure 6-2 Graphene transfer process. (a)-(c) is used to remove the graphene layer from the backside of the copper foil. (d)-(g) are the steps for the polymer carrier transfer technique.

To make multilayer graphene films, the graphene/PMMA stack can be transferred to another copper foil with graphene grown on top of it in the same fashion as describe above for transferring to a polymer support. Now we have a copper foil with 2 layers of graphene followed by the PMMA carrier layer. Next, the 2 layer graphene plus PMMA stack can be transferred by etching the copper foil. This can repeated to get until the desired number of layers are attained and then the graphene layers with PMMA on top can be transferred to the polymer support. We did not wash or burn the PMMA off due to the fact that the PSf support was sensitive to both treatments. The final product is a PMMA, n-layer graphene, PSf support stack.

6.3.2. Press Transfers

The press transfer technique was developed to eliminate the need for the polymer carrier layer which is influential in the gas transport measurements [44], [177]. We start with a copper foil with graphene on one side. Next, we place our polymer support directly onto the copper foil with the graphene, sandwiching the graphene between the polymer support and the copper foil. We then place it between two glass microscope slides and apply ~20psi at 70˚C for 90 minutes (Figure 6-3a). After the pressure and heat treatment, we remove the copper foil/graphene/polymer support from the glass slides and place this in the etching solution to remove the copper foil (Figure 6-3b). After the etching of the copper foil, we are left with graphene adhered to the polymer support. We remove this from the etching solution and place it a DI water bath to clean the graphene from residual etching solution (Figure 6-3c). Once removed from the DI water bath, we dry it in air overnight.

Using this method, we can also make multilayer graphene films. In order to do this, we press the graphene/polymer support against another piece of graphene grown on a copper foil.

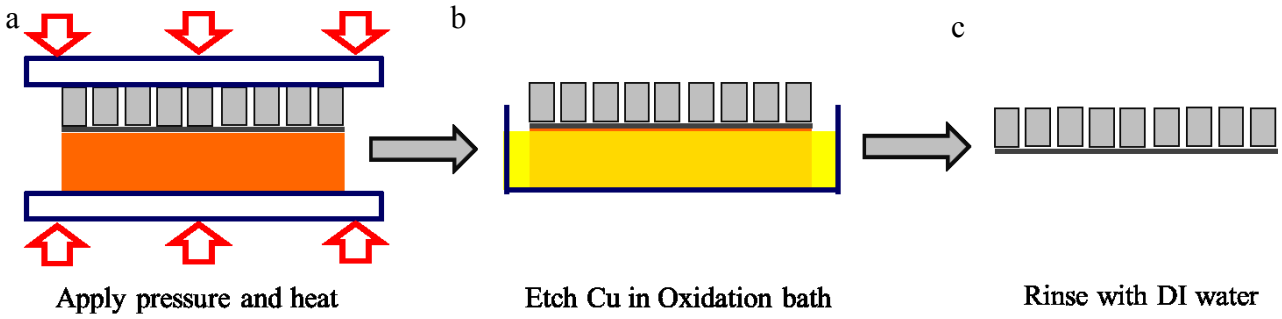

Figure 6-3 (a)-(c) Schematic of press transfer technique.

We then repeat the above procedure and are left 2 layers on top of our polymer support. We can then repeat this procedure until we have the desired number of graphene layers.

6.4. Results

Single component gas permeation rates were measured for transferred CVD graphene films with 1 through 6 layers of graphene using both the polymer carrier layer technique and the press transfer technique mentioned above. Both sets of results are for graphene transferred to a porous PSf support. Figure 6-4a shows the results for bare PSf along with PMMA transferred to the PSf support and 1 layer of graphene transferred to the PSf support with the PMMA layer on top of the graphene. We can see that the PMMA and graphene are both acting as barriers and the graphene is blocking some of the pores in the PSf support. Figure 6-4b shows the results for1, 2, 3, 4, and 6 layers of graphene with PMMA on top of the graphene layers. The general trend is that additional graphene layers act as an increased barrier but there is significant scatter in the results. This could be due to variations in the quality of the graphene grown or variations in the thickness of the PMMA layer.

To avoid variation in the PMMA layer thickness we moved to the press transfer method in which PMMA is not used in the transfer process. The results for PSf, pressed with an annealed copper foil but without any graphene grown on the copper foil as a control for the press technique and 1 through 4 layers of graphene transferred to the PSf support. Figure 6-4c shows the results which are similar to that of the PMMA transfer technique expect that the permeation rates are higher than the PMMA transfer technique due to the absence of the PMMA layer. The trend of the addition of graphene layers acting as a barrier is less clear in this data as opposed to

a

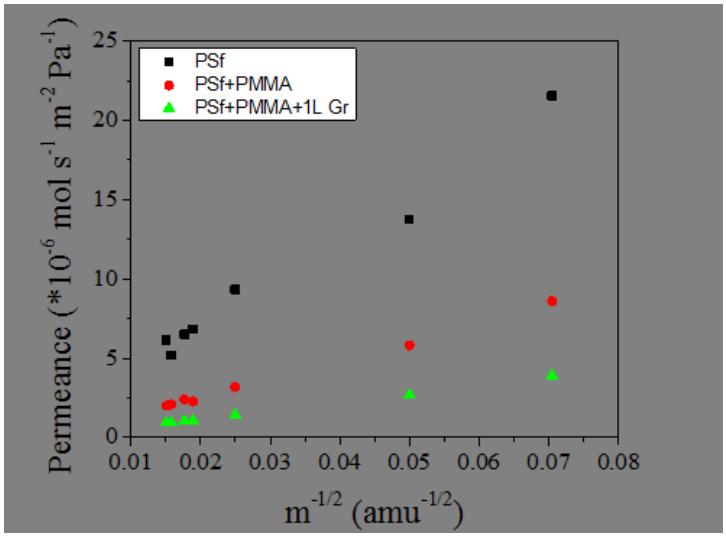

b

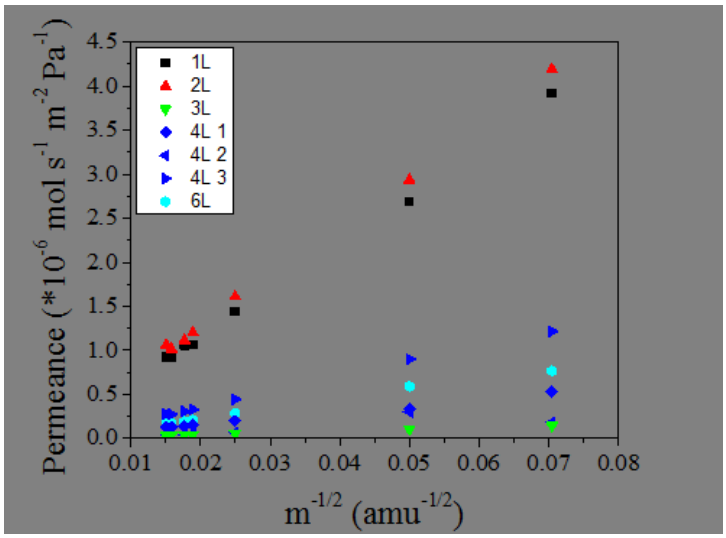

c

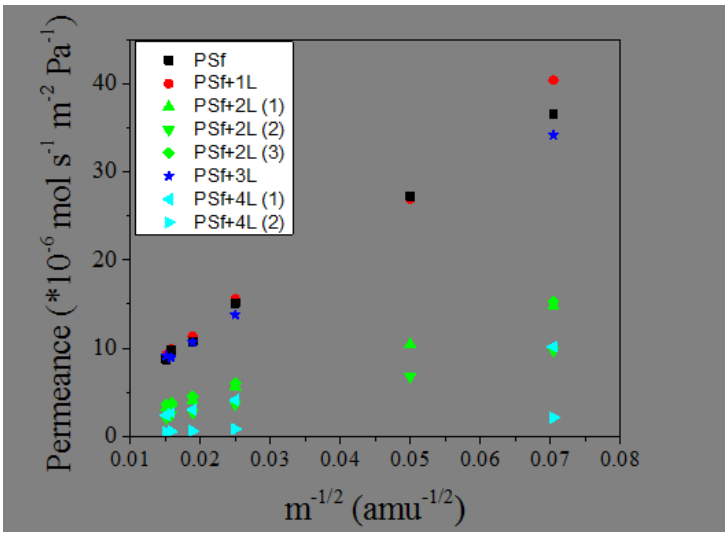

Figure 6-4 Single component transport measurements for the two transfer techniques. (a) and (b) are for the PMMA transfer technique and (c) is the results for the press transfer technique.

the polymer carrier transfer process. Again we have significant scatter in the results. Possible origins of this scatter are the heat and pressure treatment collapsing the pores in the PSf support and/or variations in the quality of the CVD graphene films.

A number of challenges have been encountered with the creating large scale gas separation membranes with graphene. Among the challenges are creating large scale membranes from CVD graphene that are impermeable barriers. This could be due to voids in the graphene films or small voids being created in the membranes during the transfer process. These voids could not be detected using optical microscopy. O'Hem *et al.* showed that CVD graphene films can have intrinsic defects on the order of 1-15 nm which would be detrimental to graphene being an impermeable barrier or using graphene as a gas separation membrane [177]. We also had challenges with both transfer techniques due to variations in the processing which could be contributing to the changes in transport.

6.5. Conclusions

In this chapter we explored the first steps to fabricating large scale CVD grown graphene membranes for gas separations. The first step was to fabricate impermeable barriers. We introduced two techniques to make large scale graphene films and measured the transport properties across films created by these methods. Although we did not create perfectly impermeable barriers we showed that as the number of graphene layers is increased the barrier properties also increased. More work will need to be done to understand why the graphene films are not acting as complete gas barriers.

7. Conclusions and Suggestions for Future Work

7.1. Summary

This thesis examined the mechanics and adhesion as well as explored gas separations with thinnest possible material, graphene. Chapters 1-3 included an overview of the basic concepts relevant to the experimental results presented in Chapters 4-6. Chapter 1 began with discussing mechanical properties of materials and the fundamentals of gas separation membranes. Chapter 2 provided an introduction to carbon allotropes and graphene and an introduction to using graphene as a gas separation membrane. Chapter 3 started with a review of adhesion and then introduced methods for measuring adhesion and in membranes. Chapter 3 also included the fundamental mechanics, both static and dynamic, of circular membranes.

The experimental section started in Chapter 4. Here a pressurized blister test was used to measure both the in-plane mechanical properties and adhesion energy of monolayer and few layer graphene suspended over a circular cavity in silicon dioxide. The adhesion energy between graphene and silicon dioxide was found to be 0.45 ± 0.02 J m^{-2} for monolayer graphene and 0.31 ± 0.03 J m^{-2} for samples containing two to five graphene layers. These values are larger than the adhesion energies measured in typical micromechanical structures and are comparable to solid-liquid adhesion energies. We attribute this to the extreme flexibility of graphene, which allows is to conform to the topography of even the smoothest substrates, thus making its interaction with the substrate more liquid like than solid like. In addition we found that the in-plane mechanical properties are consistent with previously reported values.

In Chapter 5 we show that ultraviolet-induced oxidative etching can create pores in micrometer-sized graphene membranes, and the resulting membranes can be used as molecular

sieves. A pressurized blister test, similar to that used for testing the mechanical properties, and mechanical resonance are used to measure the transport of a range of gases (H_2, CO_2, Ar, N_2, CH_4, and SF_6) through the pores. The experimentally measured leak rate, separation factors, and Raman spectrum agree well with models based on effusion through a small number of angstrom-sized pores.

In Chapter 6 we work toward creating large scale gas separation membranes from CVD grown graphene films. CVD graphene films are grown on copper foils and transferred to a polymer support or suspended over openings in copper. Films are measured in a time lag permeation apparatus to get gas permeation and ideal gas separation factors.

7.2. Future Outlook

The field of graphene adhesion is one that is currently blossoming and there is still much to be explored and learned about graphene. There is still a lot to be learned about graphene to substrate, as well as graphene to graphene interactions, from both an experimental and theoretical perspective. The origin of monolayer graphene having a higher adhesion energy still needs to be fully understood. One possible explanation that is currently being explored further is the effect of surface roughness on adhesion of single and few layer graphene. These studies are still in their infancy [157]. Many more aspect of graphene adhesion are still ripe to be explored such as graphene adhering to materials other than silicon oxide[69] and graphene adhesion to biological cells [182]. A better understanding of graphene to graphene and graphene to substrate interactions can be used to make future devices and also improve graphene transfer processes [183].

As can be seen from the conclusion of Chapter 6 there is still a large amount of work to be done before graphene membranes are suitable for industrial scale gas separation applications. A variety of advances need to be made in the large scale manufacturing of graphene membranes including higher quality CVD grown graphene and the transfer of those graphene films to the appropriate supporting material. There are other methods to producing large scale gas separation membranes that remain largely unexplored such as incorporating graphene into a polymer matrix for gas separation application. It could also be that graphene is not the ultimate answer for more gas separation membranes and another 2D material with intrinsic pores suitable for gas separations might prove to be a better solution. Since the discovery of graphene there have been a wealth of other 2D materials proposed and synthesized.

One route might be with two dimensional polymers [184], [185]. The field of 2D polymers is growing quickly. Polymers could be synthesized more quickly and require less energy to manufacture. Where graphene must be synthesized at 1000 ˚C on a metal catalyst 2D polymers can be made in solution at more moderate temperatures and thus be cheaply and easily manufactured on a large scale [186].

In addition, there is much to be learned about the gas transport properties across molecular sized pores. Even if graphene is not the ultimate answer when it comes to gas separation membranes, much can be learned about the transport across these novel pores. Never before has there been a chance to so carefully measure the transport through a few number of pores but it will no doubt lead to a wealth of knowledge in this area and perhaps guide the design of the next generation gas separation membranes.

APPENDIX 1

We use the method of image charges to estimate the influence of trapped charges in the SiO_2 on the adhesion of graphene to the substrate. The adhesion needed to move a density of charges from a distance *d* from the conducting plane out to infinity is given by equation {3-11}. If we assume all the charges are on the surface of the SiO_2 and that the equilibrium spacing between the graphene and SiO_2 is equal to that of the equilibrium spacing of graphite $d = 0.34$ nm. The charge density needed to produce our measured adhesion energy of 0.31 J/m^2 is ~9x10^{17} m^{-2}. The charge density of SiO_2 is reported to be 2.3x10^{15} m^{-2} [187]. Seeing that the reported value of the charge density in SiO_2 is almost three orders of magnitude lower, we can conclude that trapped charges do not have a significant contribution to the adhesion energy value we measure. Other studies have used potassium ions to increase the charge density present in the oxide [188]. The concentration of potassium ions was as high as ~5 x 10^{16} m^2. This upper limit of the extrinsic doping concentration results in a charge density that is one order of magnitude less than that needed to have adhesion energies on the order of what we measured. These results show that the effect of charge impurities in the SiO_2 below the graphene will not significantly influence our measure of adhesion energy.

APPENDIX 2

As can be seen from equation {6-1} in order to calculate the permeability of a given membrane the volume, V, of the downstream side of the measurement apparatus must be known. In order to find the volume of the downstream side, we first put an impermeable metal foil in the place of the membrane to seal the two volumes. Next both sides are pumped down to vacuum and then the upstream side is filled to given pressure, P_1. Next, the "large" upstream volume (this will be referred to as V_L) is open to the "small" downstream volume (V_S) and the added volume will cause the pressure to drop to P_2. Since there are two unknowns we will next need to insert solid object of known volume and repeat the process. For the objects of known volume we use 1 inch stainless steel ball bearing of volume V_{bb}. Measurements were done with 0 to 35 ball bearings. To find the two volumes a linear fit of the data was taken and the relationship between P_1, P_2, and the number of ball bearings, N_{bb} is derived from the ideal gas law (equation {5-1}) assuming isothermal expansion between the two volumes to find the unknown volumes. The equation to find V_L and V_S given by

$$\frac{1}{P_1/P_2 - 1} = -N_{bb}\frac{V_{bb}}{V_s} + \frac{V_S}{V_L} \qquad \{A2\text{-}1\}$$

Now since we know V_{bb}, we can find V_S and V_L from the slope and intercept of the linear fit to the data in Figure A2-1d. From the linear fit we find that the slope is 1.069 and the y-intercept is 94.27. Now knowing V_{bb} = 2.145cm^3 we calculate V_S and V_L to be 2.007 cm^3 and 189.2 cm^3 respectively. Now that the downstream volume is well known, accurate measurements of the flux

across the membrane can be found from the measurement of *dp/dt* taken from the downstream pressure sensor.

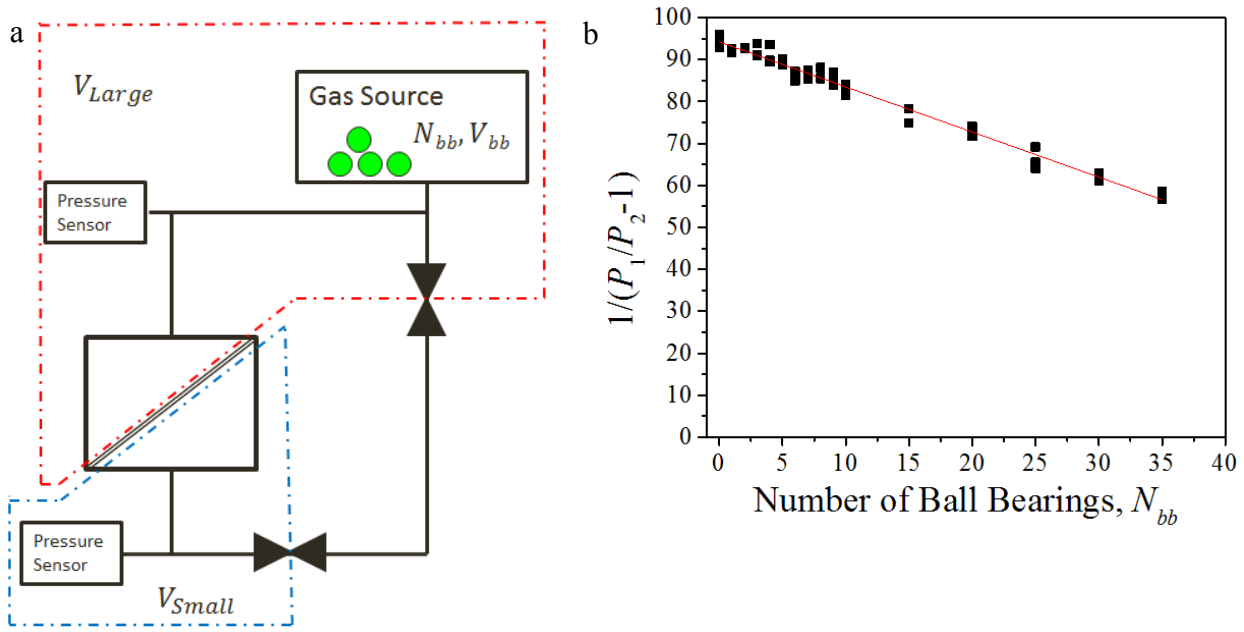

Figure A2-1 (a) Schematic of method for volume calibration. The green circles represent the ball bearings of a known volume V_{bb} that are used to find the large and small volumes. (b) Graph of number of ball bearing, N_{bb}, vs $1/(P_1/P_2\text{-}1)$. A linear fit of the data, red line is used to find the volumes.

REFERENCES

[1] A. K. Geim and K. S. Novoselov, “The rise of graphene.,” *Nature Materials*, vol. 6, no. 3, pp. 183–91, Mar. 2007.

[2] I. W. Frank, D. M. Tanenbaum, a. M. van der Zande, and P. L. McEuen, “Mechanical properties of suspended graphene sheets,” *Journal of Vacuum Science & Technology B*, vol. 25, no. 6, pp. 2558–2561, 2007.

[3] Q. Zhou and A. Zettl, “Electrostatic Graphene Loudspeaker,” *arXiv.org*, vol. 1303.2391, p. 15, Mar. 2013.

[4] D. Wei, Y. Liu, H. Zhang, L. Huang, B. Wu, J. Chen, and G. Yu, “Scalable synthesis of few-layer graphene ribbons with controlled morphologies by a template method and their applications in nanoelectromechanical switches.,” *Journal of the American Chemical Society*, vol. 131, no. 31, pp. 11147–54, Aug. 2009.

[5] P. Blake, P. D. Brimicombe, R. R. Nair, T. J. Booth, D. Jiang, F. Schedin, L. A. Ponomarenko, S. V Morozov, H. F. Gleeson, E. W. Hill, A. K. Geim, and K. S. Novoselov, “Graphene-Based Liquid Crystal Device,” *Nano Letters*, vol. 8, no. 6, pp. 1704–1708, Jun. 2008.

[6] K. S. K. S. Kim, Y. Zhao, H. Jang, S. Y. Lee, J. M. Kim, J.-H. Ahn, P. Kim, J.-Y. Choi, B. H. Hong, and et al. Kuen Soo Kim, “Large-scale pattern growth of graphene films for stretchable transparent electrodes.,” *Nature*, vol. 457, no. 7230, pp. 706–10, Feb. 2009.

[7] C. A. Klein and G. F. Cardinale, “Young’s modulus and Poisson's ratio of CVD diamond,” *Diamond and Related Materials*, vol. 2, no. 5–7, pp. 918–923, Apr. 1993.

[8] P. C. Chou and N. J. Pagano, *Elasticity: Tensor, Dyadic, and Engineering Approaches*, Dover edit. Mineola, NY: Dover, 1992.

[9] D.-B. Zhang, E. Akatyeva, and T. Dumitrică, “Bending Ultrathin Graphene at the Margins of Continuum Mechanics,” *Physical Review Letters*, vol. 106, no. 25, p. 255503, Jun. 2011.

[10] Q. Lu, M. Arroyo, and R. Huang, “Elastic bending modulus of monolayer graphene,” *Journal of Physics D: Applied Physics*, vol. 42, no. 10, p. 102002, May 2009.

[11] S. T. Thornton and J. B. Marion, *Classical Dynamics of Particles and Systems*, Fifth. Belmont, CA: Brooks/Cole, 2004.

[12] P. Pandey and R. S. Chauhan, “Membranes for gas separation,” *Progress in Polymer Science*, vol. 26, no. 6, pp. 853–893, Aug. 2001.

[13] P. Bernardo, E. Drioli, and G. Golemme, “Membrane Gas Separation: A Review/State of the Art,” *Industrial & Engineering Chemistry Research*, vol. 48, no. 10, pp. 4638–4663, May 2009.

[14] R. Mahajan and W. J. Koros, “Mixed matrix membrane materials with glassy polymers. Part 1,” *Polymer Engineering & Science*, vol. 42, no. 7, pp. 1432–1441, Jul. 2002.

[15] E. A. Jackson, *Equilibrium Statistical Mechanics*. Englewood Cliffs, NJ: Presntice-Hall, 1968, pp. 126–130.

[16] C. Kittel, *Elementary Statisitcal Physics*, Dover Edit. Mineola, NY: Dover, 1986.

[17] D. Jiang, V. R. Cooper, and S. Dai, "Porous graphene as the ultimate membrane for gas separation.," *Nano letters*, vol. 9, no. 12, pp. 4019–24, Dec. 2009.

[18] R. J. R. Uhlhorn, M. H. B. J. Huis In't Veld, K. Keizer, and A. J. Burggraaf, "High permselectivities of microporous silica-modifiedγ-alumina membranes," *Journal of Materials Science Letters*, vol. 8, no. 10, pp. 1135–1138, Oct. 1989.

[19] J. G. Wijmans and R. W. Baker, "The solution-diffusion model: a review," *Journal of Membrane Science*, vol. 107, no. 1–2, pp. 1–21, Nov. 1995.

[20] K. S. Novoselov, A. K. Geim, S. V Morozov, D. Jiang, Y. Zhang, S. V Dubonos, I. V Grigorieva, and A. A. Firsov, "Electric field effect in atomically thin carbon films," *Science*, vol. 306, no. 5696, pp. 666–669, 2004.

[21] H. Du, J. Li, J. Zhang, G. Su, X. Li, and Y. Zhao, "Separation of Hydrogen and Nitrogen Gases with Porous Graphene Membrane," *The Journal of Physical Chemistry C*, vol. 115, no. 47, pp. 23261–23266, Dec. 2011.

[22] J. Schrier, "Helium Separation Using Porous Graphene Membranes," *The Journal of Physical Chemistry Letters*, vol. 1, no. 15, pp. 2284–2287, Aug. 2010.

[23] Y. Li, Z. Zhou, P. Shen, and Z. Chen, "Two-dimensional polyphenylene: experimentally available porous graphene as a hydrogen purification membrane.," *Chemical Communications*, vol. 46, no. 21, pp. 3672–4, Jun. 2010.

[24] K. Sint, B. Wang, and P. Král, "Selective ion passage through functionalized graphene nanopores.," *Journal of the American Chemical Society*, vol. 130, no. 49, pp. 16448–9, Dec. 2008.

[25] M. E. Suk and N. R. Aluru, "Water Transport through Ultrathin Graphene," *The Journal of Physical Chemistry Letters*, vol. 1, no. 10, pp. 1590–1594, May 2010.

[26] F. Diederich and Y. Rubin, "Synthetic Approaches toward Molecular and Polymeric Carbon Allotropes," *Angewandte Chemie International Edition in English*, vol. 31, no. 9, pp. 1101–1123, Sep. 1992.

[27] A. K. Geim and P. Kim, "Carbon wonderland," *Scientific American*, vol. 298, no. 4, pp. 90–97, 2008.

[28] F. Bonaccorso, Z. Sun, T. Hasan, and A. C. Ferrari, "Graphene photonics and optoelectronics," *Nature Photonics*, vol. 4, no. 9, pp. 611–622, Aug. 2010.

[29] C. Lee, X. Wei, J. W. Kysar, and J. Hone, "Measurement of the Elastic Properties and Intrinsic Strength of Monolayer Graphene," *Science*, vol. 321, no. 5887, pp. 385–388, Jul. 2008.

[30] Y. Huang, J. Wu, and K. C. Hwang, "Thickness of graphene and single-wall carbon nanotubes," *Physical Review B (Condensed Matter and Materials Physics)*, vol. 74, no. 24, pp. 245413–245419, 2006.

[31] L. Tapasztó, T. Dumitrică, S. J. Kim, P. Nemes-Incze, C. Hwang, and L. P. Biró, "Breakdown of continuum mechanics for nanometre-wavelength rippling of graphene," *Nature Physics*, vol. 8, no. 10, pp. 739–742, Aug. 2012.

[32] C. Wang, K. Mylvaganam, and L. Zhang, "Wrinkling of monolayer graphene: A study by molecular dynamics and continuum plate theory," *Physical Review B*, vol. 80, no. 15, p. 155445, Oct. 2009.

[33] Y. Wei, B. Wang, J. Wu, R. Yang, and M. L. Dunn, "Bending rigidity and Gaussian bending stiffness of single-layered graphene.," *Nano Letters*, vol. 13, no. 1, pp. 26–30, Jan. 2013.

[34] W. Bao, F. Miao, Z. Chen, H. Zhang, W. Jang, C. Dames, and C. N. Lau, "Controlled ripple texturing of suspended graphene and ultrathin graphite membranes.," *Nature Nanotechnology*, vol. 4, no. 9, pp. 562–6, Sep. 2009.

[35] M. Poot and H. S. J. van der Zant, "Nanomechanical properties of few-layer graphene membranes," *Applied Physics Letters*, vol. 92, no. 6, p. 063111, Feb. 2008.

[36] N. Lindahl, D. Midtvedt, J. Svensson, O. A. Nerushev, N. Lindvall, A. Isacsson, and E. E. B. Campbell, "Determination of the bending rigidity of graphene via electrostatic actuation of buckled membranes.," *Nano Letters*, vol. 12, no. 7, pp. 3526–31, Jul. 2012.

[37] K. S. Novoselov, D. Jiang, F. Schedin, T. J. Booth, V. V Khotkevich, S. V Morozov, and a K. Geim, "Two-dimensional atomic crystals.," *Proceedings of the National Academy of Sciences of the United States of America*, vol. 102, no. 30, pp. 10451–3, Jul. 2005.

[38] R. Van Noorden, "Production: Beyond sticky tape.," *Nature*, vol. 483, no. 7389, pp. S32–3, Mar. 2012.

[39] S. Bae, H. Kim, Y. Lee, X. Xu, J.-S. Park, Y. Zheng, J. Balakrishnan, T. Lei, H. Ri Kim, Y. Il Song, Y.-J. Kim, K. S. Kim, B. Özyilmaz, J.-H. Ahn, B. H. Hong, and S. Iijima, "Roll-to-roll production of 30-inch graphene films for transparent electrodes," *Nature Nanotechnology*, vol. 5, no. 8, pp. 574–578, Jun. 2010.

[40] A. Reina, X. T. Jia, J. Ho, D. Nezich, H. B. Son, V. Bulovic, M. S. Dresselhaus, and J. Kong, "Large Area, Few-Layer Graphene Films on Arbitrary Substrates by Chemical Vapor Deposition," *Nano Letters*, vol. 9, no. 1, pp. 30–35, 2009.

[41] X. S. Li, W. W. Cai, J. H. An, S. Kim, J. Nah, D. X. Yang, R. Piner, A. Velamakanni, I. Jung, E. Tutuc, S. K. Banerjee, L. Colombo, R. S. Ruoff, and R. S. Rouff, "Large-Area Synthesis of High-Quality and Uniform Graphene Films on Copper Foils," *Science (New York, N.Y.)*, vol. 324, no. 5932, pp. 1312–4, Jun. 2009.

[42] J. W. Suk, A. Kitt, C. W. Magnuson, Y. Hao, S. Ahmed, J. An, A. K. Swan, B. B. Goldberg, and R. S. Ruoff, "Transfer of CVD-grown monolayer graphene onto arbitrary substrates.," *ACS Nano*, vol. 5, no. 9, pp. 6916–24, Sep. 2011.

[43] X. Li, Y. Zhu, W. Cai, M. Borysiak, B. Han, D. Chen, R. D. Piner, L. Colombo, and R. S. Ruoff, "Transfer of large-area graphene films for high-performance transparent conductive electrodes.," *Nano Letters*, vol. 9, no. 12, pp. 4359–63, Dec. 2009.

[44] W. Regan, N. Alem, B. Alemán, B. Geng, C. Girit, L. Maserati, F. Wang, M. Crommie, and A. Zettl, "A direct transfer of layer-area graphene," *Applied Physics Letters*, vol. 96, no. 11, p. 113102, 2010.

[45] A. Reina, H. B. Son, L. Y. Jiao, B. Fan, M. S. Dresselhaus, Z. F. Liu, and J. Kong, "Transferring and Identification of Single- and Few-Layer Graphene on Arbitrary Substrates," *Journal of Physical Chemistry C*, vol. 112, no. 46, pp. 17741–17744, 2008.

[46] Y. K. Koh, M.-H. Bae, D. G. Cahill, and E. Pop, "Reliably counting atomic planes of few-layer graphene (n > 4).," *ACS Nano*, vol. 5, no. 1, pp. 269–74, Jan. 2011.

[47] A. C. Ferrari, J. C. Meyer, V. Scardaci, C. Casiraghi, M. Lazzeri, F. Mauri, S. Piscanec, D. Jiang, K. S. Novoselov, S. Roth, and A. K. Geim, "Raman spectrum of graphene and graphene layers.," *Physical Review Letters*, vol. 97, no. 18, p. 187401, 2006.

[48] L. G. Cançado, A. Jorio, E. H. M. Ferreira, F. Stavale, C. A. Achete, R. B. Capaz, M. V. O. Moutinho, A. Lombardo, T. S. Kulmala, and A. C. Ferrari, "Quantifying defects in graphene via Raman spectroscopy at different excitation energies.," *Nano Letters*, vol. 11, no. 8, pp. 3190–6, Aug. 2011.

[49] C. Metzger, S. Rémi, M. Liu, S. V Kusminskiy, A. H. Castro Neto, A. K. Swan, and B. B. Goldberg, "Biaxial strain in graphene adhered to shallow depressions.," *Nano Letters*, vol. 10, no. 1, pp. 6–10, Jan. 2010.

[50] T. M. G. Mohiuddin, a. Lombardo, R. R. Nair, a. Bonetti, G. Savini, R. Jalil, N. Bonini, D. M. Basko, C. Galiotis, N. Marzari, K. S. Novoselov, a. K. Geim, a. C. Ferrari, and N, "Uniaxial strain in graphene by Raman spectroscopy: G peak splitting, Grüneisen parameters, and sample orientation," *Physical Review B*, vol. 79, no. 20, pp. 1–8, May 2009.

[51] A. A. Balandin, S. Ghosh, W. Bao, I. Calizo, D. Teweldebrhan, F. Miao, and C. N. Lau, "Superior thermal conductivity of single-layer graphene.," *Nano Letters*, vol. 8, no. 3, pp. 902–7, Mar. 2008.

[52] A. C. Ferrari, "Raman spectroscopy of graphene and graphite: Disorder, electron-phonon coupling, doping and nonadiabatic effects," *Solid State Communications*, vol. 143, no. 1–2, pp. 47–57, Jul. 2007.

[53] A. C. Ferrari and D. M. Basko, "Raman spectroscopy as a versatile tool for studying the properties of graphene," *Nature Nanotechnology*, vol. 8, no. 4, pp. 235–246, Apr. 2013.

[54] C. V. Raman and K. S. Krishnan, "A New Type of Secondary Radiation," *Nature*, vol. 121, no. 3048, pp. 501–502, Mar. 1928.

[55] "Raman spectroscopy in carbons: from nanotubes to diamond," *Philosophical Transactions of the Royal Society of London Series a-Mathematical Physical and Engineering Sciences*, vol. 262, no. Theme Issue, pp. 2267–2565, 2004.

[56] J. S. Bunch, S. S. Verbridge, J. S. Alden, A. M. van Der Zande, J. M. Parpia, H. G. Craighead, P. L. McEuen, and A. M. Van Der Zande, "Impermeable atomic membranes from graphene sheets.," *Nano Letters*, vol. 8, no. 8, pp. 2458–62, Aug. 2008.

[57] O. Leenaerts, B. Partoens, and F. M. Peeters, "Graphene: A perfect nanoballoon," *Applied Physics Letters*, vol. 93, no. 19, p. 193107, Nov. 2008.

[58] S. Blankenburg, M. Bieri, R. Fasel, K. Müllen, C. a Pignedoli, and D. Passerone, "Porous graphene as an atmospheric nanofilter.," *Small*, vol. 6, no. 20, pp. 2266–71, Oct. 2010.

[59] J. Schrier and J. McClain, "Thermally-driven isotope separation across nanoporous graphene," *Chemical Physics Letters*, vol. 521, pp. 118–124, Jan. 2012.

[60] A. W. Hauser and P. Schwerdtfeger, "Nanoporous Graphene Membranes for Efficient 3 He/ 4 He Separation," *The Journal of Physical Chemistry Letters*, vol. 3, no. 2, pp. 209–213, Jan. 2012.

[61] M. Hankel, Y. Jiao, A. Du, S. K. Gray, and S. C. Smith, "Asymmetrically Decorated, Doped Porous Graphene As an Effective Membrane for Hydrogen Isotope Separation," *The Journal of Physical Chemistry C*, vol. 116, no. 11, pp. 6672–6676, Mar. 2012.

[62] A. W. Hauser, J. Schrier, and P. Schwerdtfeger, “Helium Tunneling through Nitrogen-Functionalized Graphene Pores: Pressure- and Temperature-Driven Approaches to Isotope Separation,” *The Journal of Physical Chemistry C*, vol. 116, no. 19, pp. 10819–10827, May 2012.

[63] J. Israelachvilli, *Intermolecular and Surface Forces*. Academic Press, 2011.

[64] P. Blake, E. W. Hill, A. H. Castro Neto, K. S. Novoselov, D. Jiang, R. Yang, T. J. Booth, and A. K. Geim, “Making graphene visible,” *Applied Physics Letters*, vol. 91, no. 6, p. 063124, 2007.

[65] C. Casiraghi, A. Hartschuh, E. Lidorikis, H. Qian, H. Harutyunyan, T. Gokus, K. S. Novoselov, and A. C. Ferrari, “Rayleigh imaging of graphene and graphene layers.,” *Nano Letters*, vol. 7, no. 9, pp. 2711–2717, 2007.

[66] L. Girifalco, M. Hodak, and R. Lee, “Carbon nanotubes, buckyballs, ropes, and a universal graphitic potential,” *Physical Review B*, vol. 62, no. 19, pp. 13104–13110, Nov. 2000.

[67] S. Scharfenberg, D. Z. Rocklin, C. Chialvo, R. L. Weaver, P. M. Goldbart, and N. Mason, “Probing the mechanical properties of graphene using a corrugated elastic substrate,” *Applied Physics Letters*, vol. 98, no. 9, p. 091908, Jun. 2011.

[68] Z. Zong, C.-L. Chen, M. R. Dokmeci, and K. Wan, “Direct measurement of graphene adhesion on silicon surface by intercalation of nanoparticles,” *Journal of Applied Physics*, vol. 107, no. 2, p. 026104, 2010.

[69] T. Yoon, W. C. Shin, T. Y. Kim, J. H. Mun, T.-S. Kim, and B. J. Cho, “Direct measurement of adhesion energy of monolayer graphene as-grown on copper and its application to renewable transfer process.,” *Nano Letters*, vol. 12, no. 3, pp. 1448–52, Mar. 2012.

[70] S. Scharfenberg, N. Mansukhani, C. Chialvo, R. L. Weaver, and N. Mason, “Observation of a snap-through instability in graphene,” *Applied Physics Letters*, vol. 100, no. 2, p. 021910, 2012.

[71] Hertz, *Miscellaneous papers*. London: Macmillan, 1896, p. 146.

[72] R. S. Bradley, “The cohesive force between solid surfaces and the surface energy of solids,” *Philosophical Magazine*, vol. 13, no. 86, p. 853, 1932.

[73] H. C. Hamaker, “The London—van der Waals attraction between spherical particles,” *Physica*, vol. 4, no. 10, pp. 1058–1072, Oct. 1937.

[74] K. L. Johnson, K. Kendall, and A. D. Roberts, “Surface Energy and the Contact of Elastic Solids,” *Proceedings of the Royal Society A: Mathematical, Physical and Engineering Sciences*, vol. 324, no. 1558, pp. 301–313, Sep. 1971.

[75] B. . Derjaguin, V. . Muller, and Y. . Toporov, “Effect of contact deformations on the adhesion of particles,” *Journal of Colloid and Interface Science*, vol. 53, no. 2, pp. 314–326, Nov. 1975.

[76] D. Tabor, “Surface forces and surface interactions,” *Journal of Colloid and Interface Science*, vol. 58, no. 1, pp. 2–13, Jan. 1977.

[77] V. Muller, “On the influence of molecular forces on the deformation of an elastic sphere and its sticking to a rigid plane,” *Journal of Colloid and Interface Science*, vol. 77, no. 1, pp. 91–101, Sep. 1980.

[78] F. London, “The general theory of molecular forces,” *Transactions of the Faraday Society*, vol. 33, p. 8b, 1937.

[79] J. N. Israelachvili and D. Tabor, “The Measurement of Van Der Waals Dispersion Forces in the Range 1.5 to 130 nm,” *Proceedings of the Royal Society A: Mathematical, Physical and Engineering Sciences*, vol. 331, no. 1584, pp. 19–38, Nov. 1972.

[80] D. Tabor and R. H. S. Winterton, “The Direct Measurement of Normal and Retarded van der Waals Forces,” *Proceedings of the Royal Society A: Mathematical, Physical and Engineering Sciences*, vol. 312, no. 1511, pp. 435–450, Sep. 1969.

[81] D. J. Griffiths, *Introduction to Electrodynamics*, 3rd ed. Upper Saddle River, NJ: Prentice-Hall, 1999.

[82] E. Buks and M. Roukes, “Stiction, adhesion energy, and the Casimir effect in micromechanical systems,” *Physical Review B*, vol. 63, no. 3, Jan. 2001.

[83] R. Maboudian and R. T. Howe, “Critical Review: Adhesion in surface micromechanical structures,” *Journal of Vacuum Science & Technology B: Microelectronics and Nanometer Structures*, vol. 15, no. 1, pp. 1–20, Jan. 1997.

[84] S. K. Lamoreaux, “Resource Letter CF-1: Casimir Force,” *American Journal of Physics*, vol. 67, no. 10, p. 850, Oct. 1999.

[85] K. L. Mittal, “Adhesion Measurement of Thin Films,” *ElectroComponent Science and Technology*, vol. 3, no. 1, pp. 21–42, 1976.

[86] B. N. Chapman, “Thin-film adhesion,” *Journal of Vacuum Science and Technology*, vol. 11, no. 1, p. 106, Jan. 1974.

[87] J. Valli, “A review of adhesion test methods for thin hard coatings,” *Journal of Vacuum Science & Technology A: Vacuum, Surfaces, and Films*, vol. 4, no. 6, p. 3007, Nov. 1986.

[88] A. Sofla, E. Seker, J. P. Landers, and M. R. Begley, “PDMS-Glass Interface Adhesion Energy Determined Via Comprehensive Solutions for Thin Film Bulge/Blister Tests,” *Journal of Applied Mechanics*, vol. 77, no. 3, pp. 031007–5, May 2010.

[89] J. E. Pawel and C. J. McHargue, “Testing of adhesion of thin films to substrates,” *Journal of Adhesion Science and Technology*, vol. 2, no. 1, pp. 369–383, Jan. 1988.

[90] J. E. E. Baglin, *Fundamentals of Adhesion*. New York: Srpinger, 1991.

[91] J. Williams, “Energy release rates for the peeling of flexible membranes and the analysis of blister tests,” *International Journal of Fracture*, vol. 87, no. 1, pp. 265–288, Oct. 1997.

[92] K.-S. Kim and J. Kim, “Elasto-Plastic Analysis of the Peel Test for Thin Film Adhesion,” *Journal of Engineering Materials and Technology*, vol. 110, no. 3, p. 266, Jul. 1988.

[93] J. Kim, K. S. Kim, and Y. H. Kim, “Mechanical effects in peel adhesion test,” *Journal of Adhesion Science and Technology*, vol. 3, no. 1, pp. 175–187, Jan. 1989.

[94] R. Jacobsson and B. Kruse, “Measurement of adhesion of thin evaporated films on glass substrates by means of the direct pull method,” *Thin Solid Films*, vol. 15, no. 1, pp. 71–77, Jan. 1973.

[95] K. Kendall, “The adhesion and surface energy of elastic solids,” *Journal of Physics D: Applied Physics*, vol. 4, no. 8, pp. 1186–1195, Aug. 1971.

[96] M. T. Laugier, “An energy approach to the adhesion of coatings using the scratch test,” *Thin Solid Films*, vol. 117, no. 4, pp. 243–249, Jul. 1984.

[97] S. J. Bull, “Failure modes in scratch adhesion testing,” *Surface and Coatings Technology*, vol. 50, no. 1, pp. 25–32, Jan. 1991.

[98] M. Laugier, “The development of the scratch test technique for the determination of the adhesion of coatings,” *Thin Solid Films*, vol. 76, no. 3, pp. 289–294, Feb. 1981.

[99] J. Tomastik and R. Ctvrtlik, “Nanoscratch test — A tool for evaluation of cohesive and adhesive properties of thin films and coatings,” *EPJ Web of Conferences*, vol. 48, p. 00027, May 2013.

[100] C. H. Mastrangelo and C. H. Hsu, “A simple experimental technique for the measurement of the work of adhesion of microstructures,” in *Technical Digest IEEE Solid-State Sensor and Actuator Workshop*, pp. 208–212.

[101] J. A. Knapp and M. P. de Boer, “Mechanics of microcantilever beams subject to combined electrostatic and adhesive forces,” *Journal of Microelectromechanical Systems*, vol. 11, no. 6, pp. 754–764, Dec. 2002.

[102] K. Komvopoulos, “Adhesion and friction forces in microelectromechanical systems: mechanisms, measurement, surface modification techniques, and adhesion theory,” *Journal of Adhesion Science and Technology*, vol. 17, no. 4, pp. 477–517, Jan. 2003.

[103] F. W. Delrio, M. P. de Boer, J. a Knapp, E. David Reedy, P. J. Clews, M. L. Dunn, and E. D. Reedy, “The role of van der Waals forces in adhesion of micromachined surfaces.,” *Nature Materials*, vol. 4, no. 8, pp. 629–34, Aug. 2005.

[104] R. Legtenberg, H. A. C. Tilmans, J. Elders, and M. Elwenspoek, “Stiction of surface micromachined structures after rinsing and drying: model and investigation of adhesion mechanisms,” *Sensors and Actuators A: Physical*, vol. 43, no. 1–3, pp. 230–238, May 1994.

[105] N. Tas, T. Sonnenberg, H. Jansen, R. Legtenberg, and M. Elwenspoek, “Stiction in surface micromachining,” *Journal of Micromechanics and Microengineering*, vol. 6, no. 4, pp. 385–397, Dec. 1996.

[106] J. J. Vlassak and W. D. Nix, “A new bulge test technique for the determination of Young’s modulus and Poisson's ratio of thin-films,” *Journal of Materials Research*, vol. 7, no. 12, pp. 3242–3249, 1992.

[107] Y. Xiang, X. Chen, and J. J. Vlassak, “Plane-strain Bulge Test for Thin Films,” *Journal of Materials Research*, vol. 20, no. 09, pp. 2360–2370, Mar. 2011.

[108] M. K. K. Small and W. D. D. Nix, “Analysis of the accuracy of the bulge test in determining the mechanical properties of thin films,” *Journal of Materials Research; (United States)*, vol. 7:6, no. 6, pp. 1553–1563, Jun. 1992.

[109] J. S. Bunch, A. M. van der Zande, S. S. Verbridge, I. W. Frank, D. M. Tanenbaum, J. M. Parpia, H. G. Craighead, and P. L. McEuen, “Electromechanical Resonators from Graphene Sheets,” *Science*, vol. 315, no. 5811, pp. 490–493, 2007.

[110] S. P. Koenig, N. G. Boddeti, M. L. Dunn, and J. S. Bunch, “Ultrastrong adhesion of graphene membranes,” *Nature Nanotechnology*, vol. 6, no. 9, pp. 543–546, Aug. 2011.

[111] L. B. Freund and S. Suresh, *Thin Film Materials: Stress, Defect Formation and Surface Evolution*, First. Cambridge: Cambridge University Press, 2004.

[112] K. Wan, "A theoretical and numerical study of a thin clamped circular film under an external load in the presence of a tensile residual stress," *Thin Solid Films*, vol. 425, no. 1–2, pp. 150–162, Feb. 2003.

[113] S. Timoshenko and S. Woinowsky-Krieger, *Theory of Plates and Shells*, Second. New York: McGraw-Hill Book Company, 1959.

[114] K. M. Liechti and A. Shirani, "Large scale yielding in blister specimens," *International Journal of Fracture*, vol. 67, no. 1, pp. 21–36, May 1994.

[115] K. Yue, W. Gao, R. Huang, and K. M. Liechti, "Analytical methods for the mechanics of graphene bubbles," *Journal of Applied Physics*, vol. 112, no. 8, p. 083512, Oct. 2012.

[116] P. Wang, W. Gao, Z. Cao, K. M. Liechti, and R. Huang, "Numerical Analysis of Circular Graphene Bubbles," *Journal of Applied Mechanics*, vol. 80, no. 4, p. 040905, 2013.

[117] H. Hencky, "Uber den spannungzustand in kreisrunden platten mit verschwindender biegungssteiflgeit," *Z. fur Mathematik und Physik*, vol. 63, pp. 311–317, 1915.

[118] K.-T. Wan and Y.-W. Mai, "Fracture mechanics of a new blister test with stable crack growth," *Acta Metallurgica et Materialia*, vol. 43, no. 11, pp. 4109–4115, Nov. 1995.

[119] N. G. Boddeti, "Mechanics of Adhered, Pressurized Graphene Blisters," *Journal of Applied Mechanics*, vol. 80, no. 4, p. 041044, May 2013.

[120] W. B. Fichter, "Some Solutions for the Large Deflections of Uniformly Loaded Circular Membranes," *NASA Technical Paper*, vol. 3658, 1997.

[121] J. D. Campbell, "On the theory of initially tensioned circular membranes subjected to uniform pressure," *The Quarterly Journal of Mechanics and Applied Mathematics*, vol. 9, no. 1, pp. 84–93, Jan. 1956.

[122] R. A. Barton, B. Ilic, A. M. van der Zande, W. S. Whitney, P. L. McEuen, J. M. Parpia, and H. G. Craighead, "High, size-dependent quality factor in an array of graphene mechanical resonators.," *Nano Letters*, vol. 11, no. 3, pp. 1232–6, Mar. 2011.

[123] L. Wang, J. J. Travis, A. S. Cavanagh, X. Liu, S. P. Koenig, P. Y. Huang, S. M. George, and J. S. Bunch, "Ultrathin oxide films by atomic layer deposition on graphene.," *Nano Letters*, vol. 12, no. 7, pp. 3706–10, Jul. 2012.

[124] S. Levy, "Large deflection theory for rectangular plates," *Proceedings of symposia in applied mathematics*, vol. 1, 1949.

[125] K.-T. Wan and Y.-W. Mai, "Modified blister test for evaluation of thin flexible membrane adhesion on rigid substrate," *Journal of the Society of Materials Science, Japan*, vol. 44, no. 501Appendix, pp. 78–81, 1995.

[126] C. Wang, "Measurements of interfacial strength from the blister test," *Journal of Applied Polymer Science*, vol. 73, no. 10, pp. 1899–1912, Sep. 1999.

[127] H. Dannenberg, "Measurement of adhesion by a blister method," *Journal of Applied Polymer Science*, vol. 5, no. 14, pp. 125–134, Mar. 1961.

[128] K.-T. Wan, R. G. Horn, S. Courmont, and B. R. Lawn, “Pressurized internal lenticular cracks at healed mica interfaces,” *Journal of Materials Research*, vol. 8, no. 5, pp. 1128–1136, Jan. 2011.

[129] M. L. Williams, “The continuum interpretation for fracture and adhesion,” *Journal of Applied Polymer Science*, vol. 13, no. 1, pp. 29–40, Jan. 1969.

[130] S. J. Bennett, K. L. Devries, and M. L. Williams, “Adhesive fracture mechanics,” *International Journal of Fracture*, vol. 10, no. 1, pp. 33–43, Mar. 1974.

[131] J. A. Hinkley, “A Blister Test for Adhesion of Polymer Films to SiO 2,” *The Journal of Adhesion*, vol. 16, no. 2, pp. 115–125, Nov. 1983.

[132] A. N. Gent and L. H. Lewandowski, “Blow-off pressures for adhering layers,” *Journal of Applied Polymer Science*, vol. 33, no. 5, pp. 1567–1577, Apr. 1987.

[133] H.-S. Jeong, R. C. White, Y. Z. Chu, and C. J. During, “Adhesion study of polyimide to SI surfaces,” *Surface and Interface Analysis*, vol. 18, no. 4, pp. 289–292, Apr. 1992.

[134] Y. Z. Chu and C. J. Durning, “Application of the blister test to the study of polymer–polymer adhesion,” *Journal of Applied Polymer Science*, vol. 45, no. 7, pp. 1151–1164, Jul. 1992.

[135] H. S. Jeong, Y. Z. Chu, M. B. Freiler, C. Durning, and R. C. White, “Thin Film Adhesion Study in Microelectronic Packaging,” *MRS Proceedings*, vol. 239, p. 547, Feb. 2011.

[136] K. Wan, “A novel blister test to investigate thin film delamination at elevated temperature,” *International Journal of Adhesion and Adhesives*, vol. 20, no. 2, pp. 141–143, Apr. 2000.

[137] Y.-S. Chang, Y.-H. Lai, and D. Dillard, “The Constrained Blister - A Nearly Constant Strain Energy Release Rate Test for Adhesives,” *The Journal of Adhesion*, vol. 27, no. 4, pp. 197–211, 1989.

[138] M. J. Napolitano, A. Chudnovsky, and A. Moet, “The constrained blister test for the energy of interfacial adhesion,” *Journal of Adhesion Science and Technology*, vol. 2, no. 1, pp. 311–323, Jan. 1988.

[139] M. G. Allen and S. D. Senturia, “Application of the Island Blister Test for Thin Film Adhesion Measurement,” *The Journal of Adhesion*, vol. 29, no. 1–4, pp. 219–231, Oct. 1989.

[140] M. G. Allen and S. D. Senturia, “Analysis of Critical Debonding Pressures of Stressed Thin Films in the Blister Test,” *The Journal of Adhesion*, vol. 25, no. 4, pp. 303–315, Jun. 1988.

[141] D. A. Dillard and Y. Bao, “The Peninsula Blister Test: A High and Constant Strain Energy Release Rate Fracture Specimen for Adhesives,” *The Journal of Adhesion*, vol. 33, no. 4, pp. 253–271, Feb. 1991.

[142] D. Xu, K. M. Liechti, and T. H. de Lumley-Woodyear, “Closed Form Nonlinear Analysis of the Peninsula Blister Test,” *The Journal of Adhesion*, vol. 82, no. 8, pp. 831–866, Aug. 2006.

[143] K.-T. Wan and C. D. Breach, “Thermodynamics of a Stable Blister Delamination at Elevated Temperature,” *The Journal of Adhesion*, vol. 66, no. 1–4, pp. 183–202, Mar. 1998.

[144] S. Timoshenko, D. H. Young, and W. Weaver, *Vibration Problems in Engineering*, 4th ed. New York: John Wiley and Sons, Inc., 1974, pp. 481–484.

[145] J. C. Meyer, A. K. Geim, M. I. Katsnelson, K. S. Novoselov, T. J. Booth, and S. Roth, "The structure of suspended graphene sheets," *Nature*, vol. 446, no. 7131, pp. 60–63, 2007.

[146] R. R. Nair, P. Blake, a N. Grigorenko, K. S. Novoselov, T. J. Booth, T. Stauber, N. M. R. Peres, and a K. Geim, "Fine structure constant defines visual transparency of graphene.," *Science*, vol. 320, no. 5881, p. 1308, Jun. 2008.

[147] O. L. Blakslee, D. G. Proctor, E. J. Seldin, G. B. Spence, and T. Weng, "Elastic Constants of Compression-Annealed Pyrolytic Graphite," *Journal of Applied Physics*, vol. 41, no. 8, pp. 3373–3382, 1970.

[148] F. W. DelRio, M. L. Dunn, B. L. Boyce, A. D. Corwin, and M. P. de Boer, "The effect of nanoparticles on rough surface adhesion," *Journal of Applied Physics*, vol. 99, no. 10, p. 104304, 2006.

[149] F. W. DelRio, C. Jaye, D. A. Fischer, and R. F. Cook, "Elastic and adhesive properties of alkanethiol self-assembled monolayers on gold," *Applied Physics Letters*, vol. 94, no. 13, p. 131909, 2009.

[150] M. F. Yu, T. Kowalewski, and R. S. Ruoff, "Structural analysis of collapsed, and twisted and collapsed, multiwalled carbon nanotubes by atomic force microscopy," *Physical Review Letters*, vol. 86, no. 1, pp. 87–90, 2001.

[151] W. Cullen, M. Yamamoto, K. Burson, J. Chen, C. Jang, L. Li, M. Fuhrer, and E. Williams, "High-Fidelity Conformation of Graphene to SiO2 Topographic Features," *Physical Review Letters*, vol. 105, no. 21, Nov. 2010.

[152] A. Rudenko, F. Keil, M. Katsnelson, and A. Lichtenstein, "Interfacial interactions between local defects in amorphous SiO_{2} and supported graphene," *Physical Review B*, vol. 84, no. 8, Aug. 2011.

[153] J. Sabio, C. Seoánez, S. Fratini, F. Guinea, A. Neto, and F. Sols, "Electrostatic interactions between graphene layers and their environment," *Physical Review B*, vol. 77, no. 19, May 2008.

[154] Z. H. Aitken and R. Huang, "Effects of mismatch strain and substrate surface corrugation on morphology of supported monolayer graphene," *Journal of Applied Physics*, vol. 107, no. 12, p. 123531, 2010.

[155] T. Li and Z. Zhang, "Substrate-regulated morphology of graphene," *Journal of Physics D: Applied Physics*, vol. 43, no. 7, p. 075303, Feb. 2010.

[156] S. Viola Kusminskiy, D. Campbell, A. Castro Neto, and F. Guinea, "Pinning of a two-dimensional membrane on top of a patterned substrate: The case of graphene," *Physical Review B*, vol. 83, no. 16, Apr. 2011.

[157] J. S. Bunch and M. L. Dunn, "Adhesion mechanics of graphene membranes," *Solid State Communications*, vol. 152, no. 15, pp. 1359–1364, Aug. 2012.

[158] J. W. Suk, R. D. Piner, J. An, and R. S. Ruoff, "Mechanical properties of monolayer graphene oxide.," *ACS Nano*, vol. 4, no. 11, pp. 6557–64, Nov. 2010.

[159] C. S. Ruiz-Vargas, H. L. Zhuang, P. Y. Huang, A. M. van der Zande, S. Garg, P. L. McEuen, D. A. Muller, R. G. Hennig, and J. Park, "Softened elastic response and unzipping in chemical vapor deposition graphene membranes.," *Nano Letters*, vol. 11, no. 6, pp. 2259–63, Jun. 2011.

[160] C. Lee, Q. Li, W. Kalb, X.-Z. Liu, H. Berger, R. W. Carpick, and J. Hone, "Frictional characteristics of atomically thin sheets.," *Science*, vol. 328, no. 5974, pp. 76–80, Apr. 2010.

[161] C. H. Lui, L. Liu, K. F. Mak, G. W. Flynn, and T. F. Heinz, "Ultraflat graphene.," *Nature*, vol. 462, no. 7271, pp. 339–41, Nov. 2009.

[162] F. Capasso, J. N. Munday, D. Iannuzzi, and H. B. Chan, "Casimir Forces and Quantum Electrodynamical Torques: Physics and Nanomechanics," *IEEE Journal of Selected Topics in Quantum Electronics*, vol. 13, no. 2, pp. 400–414, 2007.

[163] Z. Lu and M. L. Dunn, "van der Waals adhesion of graphene membranes," *Journal of Applied Physics*, vol. 107, no. 4, p. 044301, 2010.

[164] R. R. Nair, H. A. Wu, P. N. Jayaram, I. V. Grigorieva, and A. K. Geim, "Unimpeded Permeation of Water Through Helium-Leak-Tight Graphene-Based Membranes," *Science*, vol. 335, no. 6067, pp. 442–444, Jan. 2012.

[165] S. Chen, L. Brown, M. Levendorf, W. Cai, S.-Y. Ju, J. Edgeworth, X. Li, C. W. Magnuson, A. Velamakanni, R. D. Piner, J. Kang, J. Park, and R. S. Ruoff, "Oxidation Resistance of Graphene-Coated Cu and Cu/Ni Alloy," *ACS Nano*, vol. 5, no. 2, pp. 1321–1327, Jan. 2011.

[166] S. Ozeki, T. Ito, K. Uozumi, and I. Nishio, "Scanning Tunneling Microscopy of UV-Induced Gasification Reaction on Highly Oriented Pyrolytic Graphite," *Japanese Journal of Applied Physics*, vol. 35, no. Part 1, No. 6B, pp. 3772–3774, Jun. 1996.

[167] S. Huh, J. Park, Y. S. Kim, K. S. Kim, B. H. Hong, and J.-M. Nam, "UV/Ozone-Oxidized Large-Scale Graphene Platform with Large Chemical Enhancement in Surface-Enhanced Raman Scattering.," *ACS Nano*, vol. 5, no. 12, pp. 9799–9806, Nov. 2011.

[168] L. Liu, S. Ryu, M. R. Tomasik, E. Stolyarova, N. Jung, M. S. Hybertsen, M. L. Steigerwald, L. E. Brus, and G. W. Flynn, "Graphene oxidation: thickness-dependent etching and strong chemical doping.," *Nano Letters*, vol. 8, no. 7, pp. 1965–70, Jul. 2008.

[169] H. Chang and A. J. Bard, "Scanning tunneling microscopy studies of carbon-oxygen reactions on highly oriented pyrolytic graphite," *Journal of the American Chemical Society*, vol. 113, no. 15, pp. 5588–5596, Jul. 1991.

[170] M. Bieri, M. Treier, J. Cai, K. Aït-Mansour, P. Ruffieux, O. Gröning, P. Gröning, M. Kastler, R. Rieger, X. Feng, K. Müllen, and R. Fasel, "Porous graphenes: two-dimensional polymer synthesis with atomic precision.," *Chemical Communications*, no. 45, pp. 6919–21, Dec. 2009.

[171] C. O. Girit, J. C. Meyer, R. Erni, M. D. Rossell, C. Kisielowski, L. Yang, C.-H. H. Park, M. F. Crommie, M. L. Cohen, S. G. Louie, and A. Zettl, "Graphene at the Edge: Stability and Dynamics," *Science*, vol. 323, no. 5922, pp. 1705–1708, Mar. 2009.

[172] J. Schrier, "Fluorinated and Nanoporous Graphene Materials As Sorbents for Gas Separations," *ACS Applied Materials & Interfaces*, vol. 3, no. 11, pp. 4451–4458, Nov. 2011.

[173] J. Bai, X. Zhong, S. Jiang, Y. Huang, and X. Duan, "Graphene nanomesh.," *Nature Nanotechnology*, vol. 5, no. 3, pp. 190–4, Mar. 2010.

[174] Z. Fan, Q. Zhao, T. Li, J. Yan, Y. Ren, J. Feng, and T. Wei, "Easy synthesis of porous graphene nanosheets and their use in supercapacitors," *Carbon*, vol. 50, no. 4, pp. 1699–1703, Apr. 2012.

[175] D. Fox, A. O'Neill, D. Zhou, M. Boese, J. N. Coleman, and H. Z. Zhang, "Nitrogen assisted etching of graphene layers in a scanning electron microscope," *Applied Physics Letters*, vol. 98, no. 24, p. 243117, Jun. 2011.

[176] D. W. Breck, *Zeolites Molecular Sieves: Structure, Chemistry, and Use*. New York, NY: Wiley, 1973, pp. 593–724.

[177] S. C. O'Hern, C. A. Stewart, M. S. H. Boutilier, J.-C. Idrobo, S. Bhaviripudi, S. K. Das, J. Kong, T. Laoui, M. Atieh, and R. Karnik, "Selective molecular transport through intrinsic defects in a single layer of CVD graphene.," *ACS Nano*, vol. 6, no. 11, pp. 10130–8, Nov. 2012.

[178] P. Y. Huang, C. S. Ruiz-Vargas, A. M. van der Zande, W. S. Whitney, M. P. Levendorf, J. W. Kevek, S. Garg, J. S. Alden, C. J. Hustedt, Y. Zhu, J. Park, P. L. McEuen, and D. A. Muller, "Grains and grain boundaries in single-layer graphene atomic patchwork quilts.," *Nature*, vol. 469, no. 7330, pp. 389–92, Jan. 2011.

[179] A. W. Tsen, L. Brown, R. W. Havener, and J. Park, "Polycrystallinity and Stacking in CVD Graphene.," *Accounts of chemical research*, Nov. 2012.

[180] S. Lee, K. Lee, C.-H. Liu, and Z. Zhong, "Homogeneous bilayer graphene film based flexible transparent conductor.," *Nanoscale*, vol. 4, no. 2, pp. 639–44, Jan. 2012.

[181] S. W. Rutherford and D. D. Do, "Review of time lag permeation technique as a method for characterisation of porous media and membranes," *Adsorption*, vol. 3, no. 4, pp. 283–312, Dec. 1997.

[182] T. R. Nayak, H. Andersen, V. S. Makam, C. Khaw, S. Bae, X. Xu, P.-L. R. Ee, J.-H. Ahn, B. H. Hong, G. Pastorin, and B. Özyilmaz, "Graphene for controlled and accelerated osteogenic differentiation of human mesenchymal stem cells.," *ACS Nano*, vol. 5, no. 6, pp. 4670–8, Jun. 2011.

[183] S. Pang, J. M. Englert, H. N. Tsao, Y. Hernandez, A. Hirsch, X. Feng, and K. Müllen, "Extrinsic corrugation-assisted mechanical exfoliation of monolayer graphene.," *Advanced Materials*, vol. 22, no. 47, pp. 5374–7, Dec. 2010.

[184] J. Sakamoto, J. van Heijst, O. Lukin, and A. D. Schlüter, "Two-dimensional polymers: just a dream of synthetic chemists?," *Angewandte Chemie (International ed. in English)*, vol. 48, no. 6, pp. 1030–69, Jan. 2009.

[185] J. Schrier, "Carbon Dioxide Separation with a Two-Dimensional Polymer Membrane," *ACS applied materials & interfaces*, vol. 4, no. 7, pp. 3745–3752, Jul. 2012.

[186] K. Baek, G. Yun, Y. Kim, D. Kim, R. Hota, I. Hwang, D. Xu, Y. H. Ko, G. H. Gu, J. H. Suh, C. G. Park, B. J. Sung, and K. Kim, "Free-Standing, Single-Monomer-Thick Two-Dimensional Polymers through Covalent Self-Assembly in Solution.," *Journal of the American Chemical Society*, vol. 135, no. 17, pp. 6523–8, May 2013.

[187] J. Martin, N. Akerman, G. Ulbricht, T. Lohmann, J. H. Smet, K. von Klitzing, and A. Yacoby, "Observation of electron–hole puddles in graphene using a scanning single-electron transistor," *Nature Physics*, vol. 4, no. 2, pp. 144–148, Nov. 2007.

[188] J.-H. Chen, C. Jang, M. Ishigami, S. Xiao, W. G. Cullen, E. D. Williams, and M. S. Fuhrer, "Diffusive charge transport in graphene on SiO2," *Solid State Communications*, vol. 149, no. 27–28, pp. 1080–1086, Jul. 2009.

[189] R. Saito, G. Dresselhaus, and M. S. Dresselhaus, *Physical Properties of Carbon Nanotubes*. London, England: Imperial College Press, 1998, p. 259.

[190] E. D. Minot, “Tuning the band structure of carbon nanotubes,” Cornell, 2004.